Hot-carrier luminescence in graphene

Submitted by Evgeny Alexeev to the University of Exeter as a thesis for the degree of Doctor of Philosophy in Physics

May, 2015

I certify that all material in this thesis which is not my own work has been identified and that no material has previously been submitted and approved for the award of a degree by this or any other University.

Evgeny Alexeev
May, 2015

Abstract

In this thesis, the effect of the sample properties on the characteristics of the hot carrier luminescence in graphene is investigated. The present work focuses on the two main issues described below.

The first issue is the modification effects of near-infrared pulsed laser excitation on graphene. For excitation fluences several orders of magnitude lower than the optical damage threshold, the interaction with ultrafast laser pulses is found to cause a stable change in the properties of graphene. This photomodification also results in a decrease of the hot photoluminescence intensity. The detailed analysis shows that ultrafast photoexcitation leads to an increase in the local level of hole doping, as well as a change in the mechanical strain. The variation of doping and strain are linked with the enhanced adsorption of atmospheric oxygen caused by the distortion of the graphene surface. These findings demonstrate that ultrashort pulsed excitation can be invasive even if a relatively low laser power is used.

Secondly, the variation of the hot photoluminescence intensity with the increasing charge carrier density in graphene is investigated. The electro-optical measurements performed using graphene field-effect transistors show a strong dependence of the photoluminescence intensity on the intrinsic carrier concentration. The emission intensity has a maximum value in undoped graphene and decreases with the increasing doping level. The theoretical calculations performed using a refined two-temperature model suggest that the reduction of the photoluminescence intensity is caused by an increase in the hot carrier relaxation rate. The modification of the carrier relaxation dynamics caused by photoinduced doping is probed directly using the two-pulse correlation measurements.

The discovered sensitivity of the hot photoluminescence to the intrinsic carrier concentration can be utilised for spatially-resolved measurements of the Fermi level position in graphene samples, offering an advantage in resolution and speed.

Acknowledgements

Firstly and most importantly, I would like to thank my supervisors, Euan Hendry and Julian Moger, without whom this thesis would not have been possible. I was very fortunate to have you as my advisors, and the experience and knowledge I have gained while working with you have made me a much better scientist. Gentle, but constant pressure from Euan and help from Julian, both moral and in the lab, allowed me to progress with the research without losing my motivation. The moral support from my mentor Volodymyr Kruglyak is also greatly appreciated.

I am very grateful to Pete Hale for his assistance with device fabrication and ultrafast measurements during the first year of my PhD. I want to thank Sam Hornett for his help in various areas throughout all these years, especially for teaching me how to set up transport measurements.

I want to express my gratitude to the old team of G28 - Alexey Kaverzin, Tim Khodkov, Alexander Markevich, and Freddie Withers - for the wonderful atmosphere of friendship and collaboration. My special thanks to Adam Price and Ivan Khrapach for organising journal clubs, FCCMP seminars and other less official gatherings that are missed so much.

I am very grateful to Saverio Russo, Andrey Shytov, Sharon Strawbridge and other members of the Quantum Systems and Nanomaterials Group for their assistance and helpful discussions. I would like to especially acknowledge Misha Portnoi for his help throughout three and a half year of my PhD and for providing me with his old desk which has been a great support in writing this thesis. My special thanks to David Horsell for helping me out with the atomic force microscopy measurements.

I want to thank David Anderson and Mark Heath for their assistance and for keeping the cleanroom facilities in perfect working order. I am very grateful to Paul Wilkins and the wonderful team of the mechanical workshop for the technical support. My special thanks to John Meakin for bearing with the endless flow of deliveries and saving me a lot of time that I would have otherwise spent collecting them.

I would like to thank my fellow PhD students for sharing their knowledge and experience with me. Tom Bointon, Charles Downing, Chris Downs, Sneha Eashwer-Singhraj, Dave Hudson, Denis Nikiforov, Alex Pearce, and Claire Woollacott, it was a great pleasure working with you and I hope that we will continue to collaborate in future.

I owe my sincere gratitude to Dominique Wehenkel for his extraordinary hospitality and for teaching me how to juggle. Very special thanks to Nicola Townsend, without whom this thesis would have been finished a few months earlier, but, perhaps, would have been a thousand words shorter.

Finally, I would like to express my gratitude to the most important people in my life. I want to thank my brother Arseny for his help and for always being a great inspiration for me and my sister-in-law Julia for making me feel at home so far away from home. I am very grateful to my nephew Daniil for visiting me during the difficult hours of writing the final chapters.

None of this would have happened without help and support of my parents. I want to especially thank my dad Mikhail for sparking my interest in physics and my mom Marina for making me learn English despite my strongest resistance. I owe my deepest gratitude to my grandmother Valentina, without whose incredible optimism and will-power no one of our family would have ever been born.

Introductory notes

Please note that in this thesis, the terms “Fermi level” and “chemical potential” are used as synonyms describing the total electrochemical potential of charge carriers in graphene. The topmost occupied energy level in the ground state of a system is referred to as ”Fermi energy”.

Chapter 4 is based on the paper E. Alexeev, J. Moger and E. Hendry, ”Photo-induced doping and strain in exfoliated graphene”, Applied Physics Letters, 103(15), 151907 [1].

Introduction

Two-dimensional electronic systems have always attracted extensive research interest due to a unique combination of quantum and classical properties that give rise to intriguing physical phenomena. The high mobilities achieved in these systems have led to the discovery of the integer [2] and fractional [3] quantum Hall effects and made them an integral part of the modern semiconductor technology.

Two-dimensional confinement of electrons in conventional systems is usually achieved using metal-oxide-semiconductor (MOS) structures [4], quantum wells [5,6] and superlattices [7]. In these systems, charge carriers are localised in a potential well, making their behaviour essentially two-dimensional. A robust and truly two-dimensional electronic system, however, can be achieved only using an atomically thin material. For a very long time, purely two-dimensional crystals had been believed to be thermodynamically unstable [8]. The experimental discovery of graphene in 2004 [9] has opened a new era in the low-dimensional electronic system research.

Graphene is a single atomic layer of graphite, in which carbon atoms are arranged into a two-dimensional honeycomb lattice. The unique properties of graphene arise from its crystal structure: the strong in-plane σ bonds formed by the intersecting sp^2-hybridised orbitals give graphene its incredible mechanical strength, while the bonding and anti-bonding of the out-of-plane p_z orbitals define its low-energy electronic structure.

The band structure of graphene was first calculated by P. Wallace in 1947 [10] using the tight-binding approximation. Graphene is a zero-band gap semiconductor, with the valence and conduction bands intersecting at the two inequivalent corners of the first Brillouin zone, K and K'. In the vicinity of these points, the electron energy dispersion can be approximated by a linear relation $E = \hbar v_F |K - k|$, where $\hbar$ is Plancks constant, $v_F \sim 10^6$ m/s is the Fermi velocity [11], and k is the wavevector of electron. The linear energy dispersion of electrons results in charge carriers in graphene behaving like mass-less Dirac fermions, described by the relativistic Dirac equation rather than the Schroedinger equation [12].

One of the consequences of this relativistic behaviour is extremely high carrier mobility. The very first graphene samples fabricated using mechanical exfoliation of graphite demonstrated a room-temperature mobility of 10 000 $\mathrm{cm}^2\ V^{-1}s^{-1}$ [9], and graphene devices encapsulated in hexagonal boron-nitride [13] show mobilities approaching the theoretically predicted limit of $2 \cdot 10^5\ \mathrm{cm}^2\ V^{-1}s^{-1}$ [14, 15].

The high carrier mobility makes graphene a very promising material for high-speed electronics; however, the absence of the band gap complicates its applications as a logic component. A variety of methods for opening the band gap have been developed, including confinement of the charge carriers in narrow nanoribbons [16–20], chemical modification [21–26] and inducing interlayer asymmetry in few-layer graphene using an electric field [27–29]. Unfortunately, the majority of these methods results in the opening of the band gap with a width of less than 360 meV [15] and also lead to significant degradation of the carrier mobility [30].

Moreover, many of the superior transport characteristics have been observed only in the samples obtained by mechanical exfoliation. The industrial use of graphene as a supplement or replacement of silicon requires a mass production method capable of producing graphene samples with the highest crystalline quality.

Another intriguing property of graphene is its unique mechanical strength. Graphene has a Young's modulus of 1 TPa and can sustain a strain of more than 20%, making it the strongest material ever tested [31]. Combined with its remarkable electronic properties, this makes it an ideal conductor for flexible electronics. However, the true potential of graphene perhaps lies in optoelectronic applications.

Owing to the symmetric conical band structure, monolayer graphene absorbs 2.3% of incident light [32], and the absorption is frequency-independent in the infrared-to-visible frequency range [32]. Moreover, monolayer and bilayer graphene can be made completely transparent for low-energy light using Pauli blocking [33,34]. The combination of broadband absorption [35], strong optical nonlinearities [36, 37] and remarkable transport properties [11] makes graphene a perfect material for optoelectronic applications.

Graphene has been used as an active element in various photonic and optoelectronic devices, including optical modulators [38–40], ultrafast photodetectors [41–43], saturable absorbers [44, 45], optical frequency converters [36, 46] and transparent conducting films [47–49]. For all these applications, it is vitally important to understand the light-matter interaction and charge carrier relaxation in graphene.

The dynamics of the hot electron relaxation has been studied extensively using a variety of optical spectroscopy techniques, including transient absorption [50–57] and photoemissions [58–61] measurements.

The relaxation of the photoexcited charge carriers in graphene consists of three fundamental steps [50, 62]. Firstly, an initially narrow distribution in energy space created by laser excitation broadens due to the electron-electron scattering. This fast process, which generally conserves energy, leads to the establishment of a Fermi - Dirac distribution within a few femtoseconds after photoexcitation [50,62,63]. The hot carrier distribution then quickly loses its energy through the emission of optical phonons, until after $\sim$ 500 fs the two systems reach thermal equilibrium [52,54,62]. These initial relaxation processes occur at a much higher rate in graphene than in other semiconductor materials due to the linear dispersion relation of electrons [63, 64]. On longer timescales, further energy relaxation occurs due to the anharmonic decay of optical phonons, with both electron and phonon systems returning to initial temperature on a time scale of few picoseconds [52, 54, 57, 62].

The initial nonequilibrium carrier distribution formed by the rapid electron-electron scattering gives rise to a broadband luminescence signal. Due to the absence of a band gap and ultrafast carrier relaxation, graphene does not produce any fluorescence emission under continuous-wave excitation, and conventional photoluminescence has been observed only in a chemically modified [4, 23, 65–67] and highly electrostatically doped graphene [68]. However, upon excitation with ultrashort laser pulses, graphene produces a broad luminescence signal, with emission for energies both higher and lower than the excitation one.

At present, only a few experimental studies of ultrafast photoluminescence (PL) have been carried out. The ultrafast PL spectrum was investigated for various excitation energies and different pulse duration [64, 69, 70]. The temporal dynamics of the emission was investigated using two-pulse correlation measurements [71] and time-resolved luminescence spectroscopy [72]. The up-converted PL was used for high-contrast imaging of graphene on arbitrary substrates [64, 70]. Due to its origin, this unique signal could give a valuable insight into the electron-electron interactions. However, the correlation between the PL characteristics and properties of graphene has not yet been established.

The implementation of graphene as an active element of optical and optoelectronics devices requires the long-term stability of its properties under various operating conditions. Due to its interfacial nature, graphene exhibits very high sensitivity to the atoms and molecules interacting with its surface. This environmental sensitivity has found its application in a wide range of different sensors [73–82], and enabled graphene conductivity to be tuned from insulating to metallic through chemical functionalisation [22, 49, 83–87]. However, it also makes the graphene properties very susceptible to changes through interaction with the environment. For examples,

adsorption of atmospheric oxygen and moisture can lead to significant hole doping of graphene [88–90] and is responsible for hysteresis effects observed in graphene field-effect transistors [91–94].

A very important case of the environmental sensitivity is the modification of graphene properties caused by photoexcitation. Reversible photoinduced doping of graphene has been reported for visible [95–97] and ultraviolet excitation [98, 99]. However, for the near-infrared region, the experimental studies have been so far limited to identifying the optical damage threshold under ultrashort pulsed excitation [100–103].

In this thesis, two main issues are addressed. Firstly, the photomodification of graphene by ultrafast near-infrared excitation is investigated. The interaction with picosecond laser pulses is found to cause a stable change of graphene properties, which reveals itself in the reduction of the PL intensity. Secondly, the relationship between the sample properties and the characteristics of the hot carrier luminescence is studied using a combination of optical and transport measurements.

The thesis has the following structure: in Chapter 1, the theoretical concepts that are essential for understanding the investigated optical phenomena and the operational principles of various measurement techniques are described. The sample fabrication and characterisation methods, including electron beam lithography, Raman spectroscopy, and transport measurements, are presented in Chapter 2.

Chapter 3 focuses on the modification of graphene properties caused by near-infrared picosecond excitation. For the pulse fluences several orders of magnitude lower than the optical damage threshold, the interaction with ultrashort laser pulses was found to result in a stable localised modification of graphene. The photomodification process is investigated for various experimental conditions (e.g. different sample thickness, excitation wavelengths and pulse width) and the changes induced in graphene are monitored using ultrafast PL spectroscopy. The modification effects demonstrate remarkable long-term stability, however, they can be reversed completely through solvent treatment or thermal annealing.

In Chapter 4, the photoinduced changes of graphene properties are investigated using Raman spectroscopy. The variation of the Raman spectra after photomodification indicates a significant increase in the level of hole doping and a change in the sample strain. These effects are explained by enhanced bonding of atmospheric oxygen caused by the distortion of the surface due to slippage and buckling of graphene. The changes of the sample properties are linked with increasing surface roughness through atomic force microscopy measurements.

Chapter 5 investigates the origin of the ultrafast PL sensitivity to the photoin-

duced changes. The dependence of the PL intensity on the carrier concentration in graphene is studied using samples with controllable chemical potential. The luminescence intensity is found to have a maximum value in samples with low intrinsic carrier density and decrease with increasing doping level. A simple two-temperature model based on a set of coupled differential equations provides a very good fit to the observed results.

Finally, Chapter 6 presents preliminary results concerning direct investigation of hot carrier relaxation in graphene through two-pulse correlation measurements. The changes of the shape of the correlation signal suggest an increase in the carrier relaxation rates in the photomodified regions.

Chapter 1

Background theory

1.1 Introduction

In this chapter, essential theoretical concepts utilised in this thesis are discussed. Many of intriguing graphene properties arise from its unique band structure with linear energy dispersion, and valence and conduction overlapping at the Dirac Point. At the beginning of the chapter, the band structure of graphene is calculated within the tight-binding approximation, and the universal optical conductance is derived using time-dependent perturbation theory. Next, basic concepts of Raman spectroscopy and its application for investigating different properties of graphene, such as doping, strain, and sample thickness, are reviewed. Finally, ultrafast photoluminescence, a unique signal arising from recombination of hot charge carrier distribution, is discussed. The two-temperature model that describes the temporal evolution of electron and phonon temperatures following the photoexcitation is presented at the end of the chapter.

1.2 Band structure of graphene

Monolayer graphene is a single layer of sp^2 hybridised carbon atoms arranged in a two-dimensional honeycomb lattice. Being a basic building block for many carbon allotropes, graphene has been a subject of extensive theoretical studies over the last 70 years. However, isolated graphene had been believed to be unstable and considered only as a theoretical concept until it was discovered experimentally by Geim and Novoselov in 2004 [9].

Each of the carbon atoms that form the graphene lattice possess six electrons; two of them belong to the tightly bound $1s$ state and do not take part in the formation of

chemical bonds. Three of the four electrons in the outer shell occupy sp^2 hybridised orbitals formed by superposition of $2s$, $2p_x$ and $2p_y$ orbitals. These orbitals have in-plane orientation with mutual angles of 120° degrees and form strong σ bonds between neighbouring atoms. The remaining fourth electron belongs to the out-of-plane unhybridised $2p_z$ orbital; the overlap between these orbitals defines low-energy electronic structure of graphene.

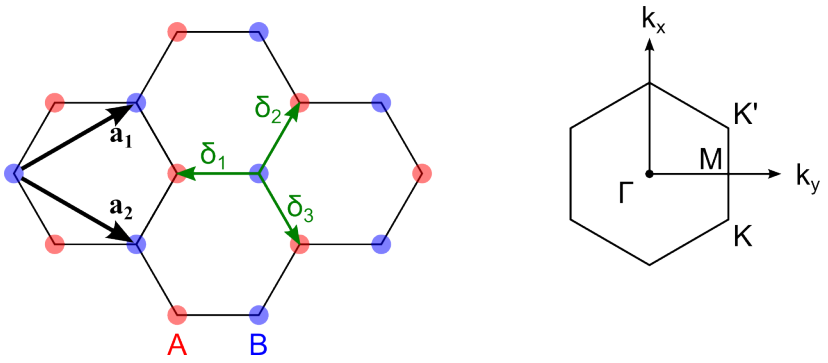

Figure 1.1: **(left)** Crystal lattice of graphene in real space. Honeycomb lattice is a triangular lattice with a basis of two: black arrows show primitive translation vectors and green arrows indicate nearest-neighbor vectors connecting two subblatices with each other. **(right)** First Brillouin zone of graphene with high symmetry points Γ, M, K and K' indicated.

Figure 1.1 **left** shows the crystal structure of graphene. The honeycomb lattice is not a Bravais lattice as its unit cell contains two inequivalent atoms, A and B. It can be seen as two intersecting triangular lattices with primitive vectors defined by

$$\boldsymbol{a}_1 = \frac{a}{2}\left(3, \sqrt{3}\right), \qquad \boldsymbol{a}_2 = \frac{a}{2}\left(3, -\sqrt{3}\right), \tag{1.1}$$

where a = 0.124 nm is the distance between two neighbouring carbon atoms. The nearest-neighbour vectors that connect an atom on the sublattice B with the three nearest atoms that belong to the sublattice A are given by the following expressions:

$$\boldsymbol{\delta}_1 = -a\begin{pmatrix} -1 \\ 0 \end{pmatrix}, \quad \boldsymbol{\delta}_2 = a\begin{pmatrix} \frac{1}{2} \\ \frac{\sqrt{3}}{2} \end{pmatrix}, \quad \boldsymbol{\delta}_3 = a\begin{pmatrix} \frac{1}{2} \\ \frac{-\sqrt{3}}{2} \end{pmatrix}. \tag{1.2}$$

The electronic band structure of graphene can be calculated using the tight binding approximation [10]. Assuming that electrons are strongly bound to their own carbon atoms and can hop only between the nearest neighbours, their wavefunction can be defined as linear combination of the wavefunctions corresponding to the atoms on different sublattices:

$$\Psi = C_A\psi_A + C_B\psi_B. \tag{1.3}$$

The atomic wavefunctions that satisfy the Bloch's theorem are constructed from linear combination of the individual $2p_z$ orbital wavefunctions of carbon atoms $\phi(\mathbf{r})$

$$\psi_j = \frac{1}{\sqrt{N}} \sum_{\boldsymbol{R}_j} e^{i\boldsymbol{k}\boldsymbol{R}_j} \phi(\boldsymbol{r} - \boldsymbol{R}_j),\ j = A, B, \tag{1.4}$$

where $\mathbf{R}_j = n_j\mathbf{a}_1 + m_j\mathbf{a}_2$ is translation vector and summation is taken over N atoms in the corresponding sublattice. Substituting the wavefunction given by Eq. 1.4 into the Schroedinger equation and multiplying it by $\langle\phi_A|$ and $\langle\phi_B|$, we get the following set of linear equations for coefficients C_A and C_B:

$$\begin{aligned} C_A \left\langle \psi_A \middle| \hat{H} \middle| \psi_A \right\rangle + C_B \left\langle \psi_A \middle| \hat{H} \middle| \psi_B \right\rangle &= E(C_A \langle \psi_A \,|\, \psi_A \rangle + C_B \langle \psi_A \,|\, \psi_B \rangle) \\ C_A \left\langle \psi_B \middle| \hat{H} \middle| \psi_A \right\rangle + C_B \left\langle \psi_B \middle| \hat{H} \middle| \psi_B \right\rangle &= E(C_A \langle \psi_B \,|\, \psi_A \rangle + C_B \langle \psi_B \,|\, \psi_B \rangle), \end{aligned} \tag{1.5}$$

If we assume that $2p_z$ wavefunctions centred on different atoms have negligible overlap, i.e. $\langle\phi_A|\phi_B\rangle = 0$, then Eq. 1.6 can be simplified as

$$\begin{aligned} C_A H_{AA} + C_B H_{AB} &= E C_A S \\ C_A H_{BA} + C_B H_{BB} &= E C_B S, \end{aligned} \tag{1.6}$$

where $H_{ij} = \langle\psi_i|\hat{H}|\psi_j\rangle$ and $S = \langle \psi_A \,|\, \psi_A \rangle = \langle \psi_B \,|\, \psi_B \rangle$. The energy spectrum of graphene can be obtained using the secular equation:

$$\begin{vmatrix} H_{AA} - ES & H_{AB} \\ H_{BA} & H_{BB} - ES \end{vmatrix} = 0. \tag{1.7}$$

Carbon atoms that form sublattices A and B are identical, therefore $H_{AA} = H_{BB}$. As individual atomic wavefunctions $\phi(\mathbf{r} - \mathbf{R}_j)$ are normalised, it is easy to show that $S = 1$ and solution of Eq. 1.7 gives

$$E = H_{AA} \pm |H_{AB}|, \tag{1.8}$$

where positive (negative) sign corresponds to the electrons in conduction (valence) bands. We can now calculate the matrix elements H_{AA} and H_{AB} in the nearest-neighbour approximation using the Bloch's functions given above (Eq. 1.4):

$$E = E_0 \pm \gamma \sqrt{1 + 4\cos\frac{\sqrt{3}k_y a}{2} \cos\frac{3k_x a}{2} + 4\cos^2\frac{\sqrt{3}k_y a}{2}}, \tag{1.9}$$

where $E_0 = \langle\phi(\boldsymbol{r} - \boldsymbol{R}_A)|\hat{H}|\phi(\boldsymbol{r} - \boldsymbol{R}_A)\rangle$ and $\gamma = \langle\phi(\boldsymbol{r} - \boldsymbol{R}_A)|\hat{H}|\phi(\boldsymbol{r} - \boldsymbol{R}_B)\rangle$. From

Eq. 1.9 it can be seen that the energy spectrum is symmetric with respect to E_0, which is the Fermi energy of undoped graphene; therefore it is convenient to set its value to zero. The term γ describes hopping between the nearest neighbours and has a value $\gamma \sim 2.8$ eV. A more accurate calculation can be made by taking into account the next-nearest-neighbour interaction, however, it gives small corrections to the result listed above.

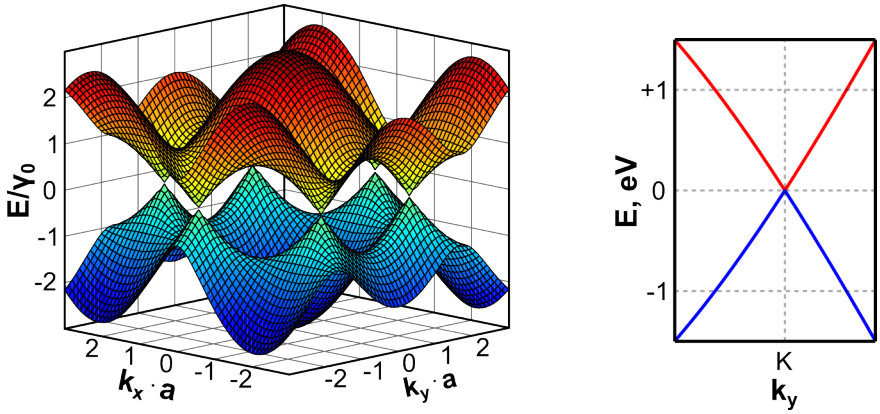

Figure 1.2: **(left)** Band structure of graphene calculated using the tight-binding approximation for nearest-neighbour hopping. **(right)** Cross-section of the band structure in the vicinity of the K point showing linear energy dispersion.

Figure 1.2 plots the energy spectrum of graphene calculated using the tight-binding approximation. Graphene has a symmetric energy dispersion relation for electrons and holes with conduction and valence band touching each other at the K and K' points of the Brillouin zone. These points are non-equivalent due to the presence of two sublattices and therefore correspond to two different valleys.

In the vicinity of the K (K') point the energy dispersion relation can be approximated by linear function

$$E = \sqrt{3}a\gamma|\mathbf{k} - \mathbf{K}|/2 = \hbar v_F|\mathbf{k} - \mathbf{K}|, \tag{1.10}$$

where $v_F = 1 \cdot 10^6$ m/s is the Fermi velocity which in the case of graphene does not depend on the carrier energy. The linear energy spectrum is similar to that of massless Dirac particles, thus K and K' point are called Dirac points.

1.3 Optical properties of graphene

1.3.1 Universal optical conductivity

One of the striking features of the graphene band structure is that it supports direct interband transitions in a very wide range of energies. In this section, we derive the light absorption of graphene within the electric dipole approximation by calculating the optical transitions rate for the electrons excited from the valence to the conduction band.

The Hamiltonian describing massless particles in the presence of an electromagnetic field has the following form [11, 12]:

$$H = v_F \boldsymbol{\sigma} \cdot (\mathbf{p} + \mathbf{eA}), \tag{1.11}$$

where $\mathbf{p}$ is the momentum operator, $\mathbf{A}$ is the vector potential and $\boldsymbol{\sigma} = (\sigma_x, \sigma_y)$ are the Pauli spin matrices that represent pseudospin. The latter describes the sublattice degree of freedom and acts analogously to the real spin of massless particles [12]. The term $v_F \boldsymbol{\sigma} e\mathbf{A}$ in the Eq. 1.11 describes interband transitions of charge carriers induced by absorptions of photons and can be considered as a perturbation. The optical transition rate in the electric dipole approximation can be calculated using Fermi's golden rule

$$W_{i\to f} = \frac{2\pi}{\hbar} \left| \left\langle f \left| \, v_F \boldsymbol{\sigma} \cdot \frac{e}{c} \mathbf{A} \, \right| i \right\rangle \right|^2 \nu(E_f)\, \delta(E_f - E_i - \hbar\omega). \tag{1.12}$$

Here, $\nu(E_f)$ is the density of final states, E_i (E_f) is the energy of the initial (final) states and $\hbar\omega$ is the energy of the absorbed photon. The wavefunction of the two-dimensional (2D) Dirac fermions in graphene is given by

$$|\psi_\pm\rangle = \frac{1}{\sqrt{2}} \begin{pmatrix} e^{-i\theta(\mathbf{k})/2} \\ \pm e^{i\theta(\mathbf{k})/2} \end{pmatrix} e^{i\mathbf{k}\cdot\mathbf{r}}, \tag{1.13}$$

where $\theta(\mathbf{k}) = \arctan(k_y/k_x)$ and negative (positive) sign corresponds to the carriers in the valence (conduction) band [12]. If we choose the electromagnetic wave to be polarised along the x axis

$$\mathbf{A} = \hat{\mathbf{x}}\, A_0 \left(e^{i\omega t} + e^{-i\omega t}\right)/2, \tag{1.14}$$

then optical transitions are controlled by the σ_x matrix. The light absorption cannot induce direct transitions within one band, therefore the only non-vanishing matrix

element is given by

$$\langle \psi_- \,|\, \sigma_x \,|\, \psi_+ \rangle = -(i/2) v_F e A_0 \sin\theta(\mathbf{k}). \tag{1.15}$$

Substituting the matrix element given by Eq. 1.15 into Eq. 1.12 and taking into account the density of states in graphene $\nu(E) = 2|E|/\pi\hbar^2 v_F^2$ we obtain the following expression for the optical transition rate in the electric dipole approximation

$$W_{-\to+}(\mathbf{k}) = \frac{e^2 A_0^2 \omega}{2\hbar^2} \sin^2\theta(\mathbf{k})\, \delta(2E - \hbar\omega). \tag{1.16}$$

Note that the delta function ensures that only charge carriers with the energy equal to the half of the photon energy can be excited to the conduction band.

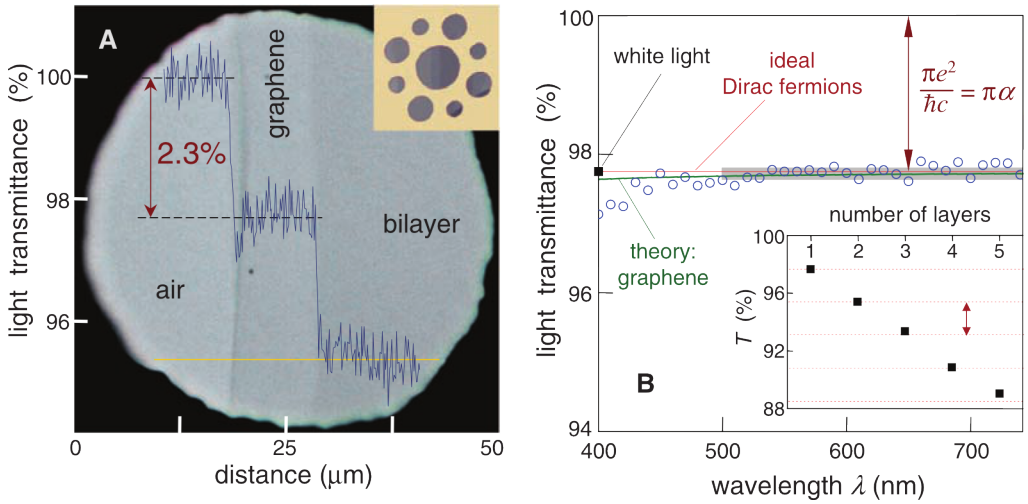

Figure 1.3: **(left)** Optical micrograph of graphene sample suspended over a 50 μm aperture.**(right)** Transmittance spectrum of monolayer graphene showing frequency-independent absorption in the near-IR to UV range. Inset plots transmittance as a function of sample thickness. Images adapted from Ref. [32].

The total transition rate per unit area can be calculated by integrating Eq. 1.16 over the momentum space and multiplying the result by 4 to account for spin and valley degeneracy

$$R = e^2 A_0^2\, \omega / 8\hbar^2. \tag{1.17}$$

Comparing the amount of light absorbed by a unit area of graphene $W_a = R \cdot \hbar\omega$ with energy flux of incoming light $W_i = c\epsilon_0 A_0^2 \omega^2/2$ we obtain the following expression for the percentage of transmitted light:

$$T = 1 - W_a/W_i = 1 - \pi\alpha \approx 0.977. \tag{1.18}$$

where $\alpha = e^2/4\pi\epsilon_0\hbar c$ is the fine structure constant. Two striking features of graphene can be seen from these calculations. Firstly, it absorbs 2.3% of incoming light despite being atomically thin. Secondly, within the linear dispersion range the absorption coefficient is independent of the excitation wavelength. Experimental measurements on suspended graphene (Fig. 1.3) show very good agreement with theoretical predictions. Graphene absorption increases linearly with the increasing number of layers for flakes up to 9 layers thick [104].

1.3.2 Raman spectrum of graphene

1.3.2.1 General introduction

Raman spectroscopy is a spectroscopic technique that utilises inelastic light scattering to probe low-frequency modes of a system. In a simplified way, the difference between elastic and Raman scattering can be described as follows: when a sample is irradiated by the excitation light, electrons are excited to the state with energy $E_g + \hbar\omega$, where E_g is the energy of the ground state and $\hbar\omega$ is the energy of the incoming photons. Since this excited state isn't stable, electrons relax to the initial state through the emission of a photon. In the majority of cases, the energy of the emitted photons will exactly match the energy of the excitation light, which corresponds to elastic or Raleigh scattering.

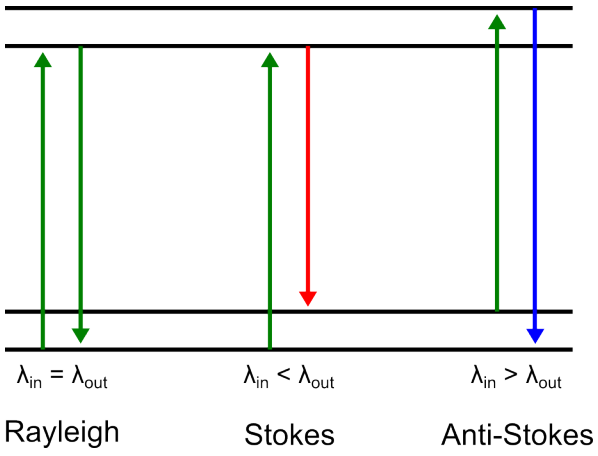

Figure 1.4: Diagram of energy levels involved in elastic and Raman scattering.

Raman scattering has a much lower probability and occurs when electrons lose some of their energy through an interaction process before returning to the ground state and the frequency of the emitted photons is therefore down-shifted. In rare cases, an incoming photon can find the system in an excited low-energy state; hence

when electron returns to the ground state it generates a photon with energy higher than that of the excitation photon.

Resonant Raman scattering takes place when the excited or intermediate state corresponds to the real energy state of the system and leads to a great improvement of the Raman signal intensity. By measuring changes in the frequency of the excitation light, vibrational, rotational and other low-frequency modes of the system can be investigated. To maximise spectral resolution, a narrow-line monochromatic light source, such as continuous wave laser, is used. Elastically scattered light will dominate sample response and must be blocked using a notch filter; down-converted (Stokes) and up-converted (anti-Stokes) components are registered with a spectrometer.

The frequency of Raman components is measured with respect to the frequency of excitation light and is expressed in the units of inverse centimetres (wavenumbers):

$$\Delta\omega = \left(\frac{1}{\lambda_{\text{in}}} - \frac{1}{\lambda_{\text{out}}}\right).$$

1.3.2.2 Raman spectrum of graphene

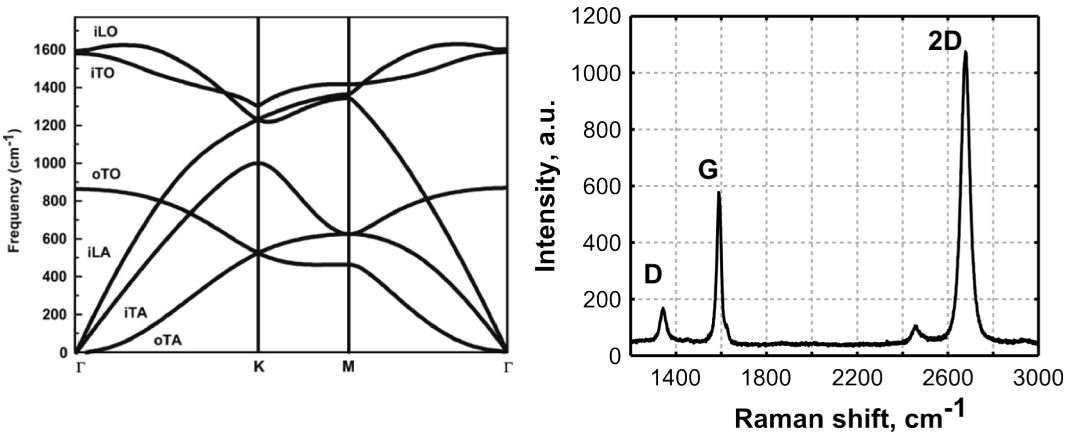

Figure 1.5: **(left)** Phonon dispersion of graphene showing three acoustic and three optical branches. Image adapted from Ref. [105] **(right)** Typical Raman spectrum of monolayer graphene showing all major peaks including defect-activated D peak at 1350 cm^{-1}.

Due to its unique band structure, which supports direct electron transitions for photon energies in the near-infrared-to-ultraviolet spectral range, even monolayer graphene produces a strong Raman signal. Raman spectroscopy can provide useful information about the state of an electron system since, for visible excitation, real electronic states serve as an intermediate state for scattering processes [106].

The Raman signal of graphene originates from electron energy loss through interaction with optical phonons. The unit cell of graphene has two inequivalent atoms, hence there are three acoustic and three optical branches in phonon dispersion relations (see Fig. 1.5 **(left)**). For one acoustic and one optical band, displacements of atoms are perpendicular to the surface of graphene (out-of-plane modes). The other four modes correspond to in-plane vibrations and are classified as longitudinal or transverse depending on direction of vibrations with respect to the A-B site direction. Only in-plane longitudinal (iLO) and transverse (iTO) optical modes are Raman-active [105].

Figure 1.5 **(right)** shows a typical Raman spectrum of monolayer graphene. The two most intense features of the spectrum are the G and 2D peaks, which lie around 1580 and 2700 cm^{-1} respectively for visible excitation. In the presence of disorder (e.g. defects, grain boundaries or at the edge of the sample) the defect-activated D peak appears at 1350 cm^{-1}.

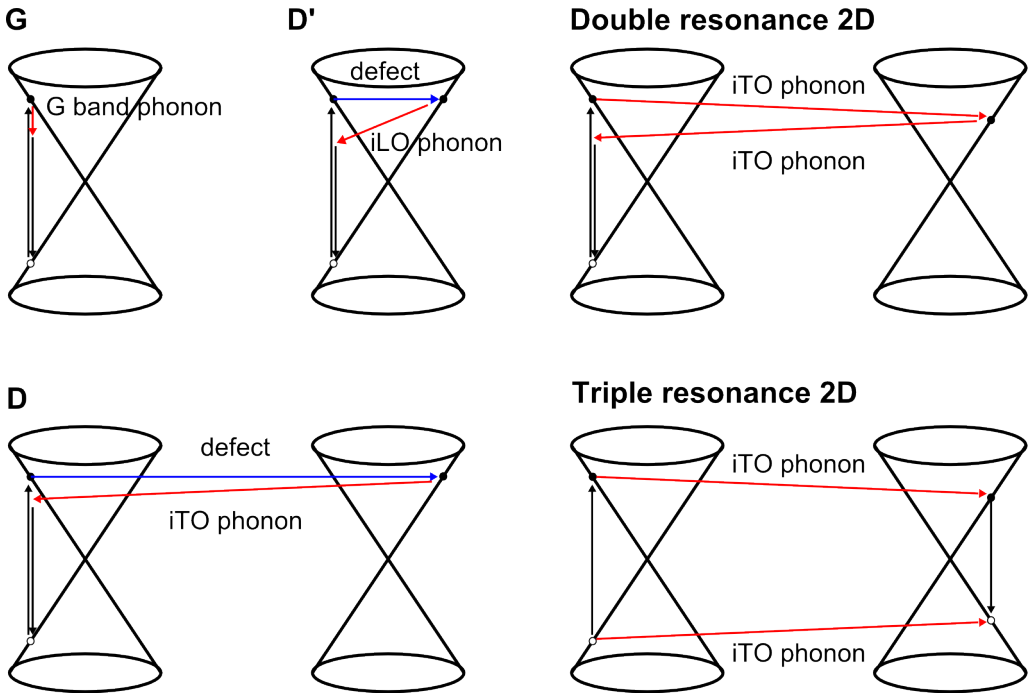

Figure 1.6: Diagram illustrating Raman scattering processes in single layer graphene. Red arrows correspond to phonon scattering and blue arrows indicate defect scattering.

Raman scattering processes associated with these peaks are illustrated in Figure 1.6. The G band originates from the first order Raman scattering process involving the double degenerate in-plane (iTO and iLO) phonon mode at the centre of the Brillouin zone. The 2D peak arises from the second-order scattering process

involving two iTO phonons near the K point. The D (D') corresponds to the second-order scattering process involving one iTO (iLO) phonon and impurity scattering and therefore is forbidden in ideal graphene.

Since both the D and 2D bands originate from double resonance Raman process, their frequencies increase linearly with increasing excitation energy with $\partial\omega_D/\partial E_{ex} = 50\text{cm}^{-1}$ for the D peak and $\partial\omega_{2D}/\partial E_{ex} = 100\,\text{cm}^{-1}$ for the 2D peak [105, 107].

1.3.2.3 Sample thickness and quality determination

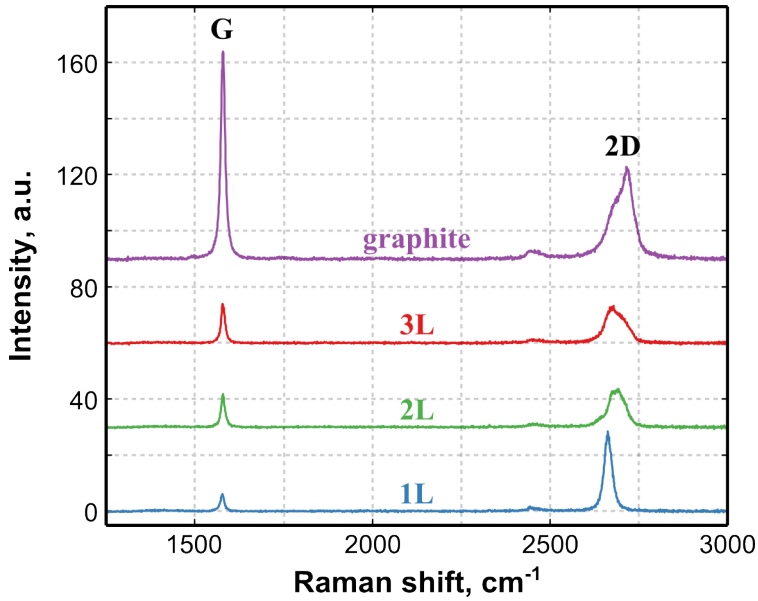

Figure 1.7: Raman spectra of monolayer **(blue)**, bilayer **(green)**, trilayer **(red)** graphene and bulk graphite **(purple)**. Baselines of spectra are shifted for clarity.

Raman spectroscopy is commonly used to determine thickness of graphene samples. Figure 1.7 compares the Raman spectra of mono-, bi- and trilayer graphene with spectrum of bulk graphite where the baselines of the spectra have been shifted for clarity. The most significant change in the Raman spectrum occurs when moving from single to bilayer graphene. The Raman spectrum of monolayer graphene **(blue)** shows sharp 2D peak with a symmetric shape and FWHM $\sim$ 25-30 cm^{-1} that can be fitted with single Lorentzian; the intensity of the 2D peak is normally 3-4 times higher than that of the G peak. The 2D peak in bilayer graphene **(green)** is much broader (FWHM $\sim 50\,\text{cm}^{-1}$) and requires four Lorentzians to reproduce its shape. The 2D and G peaks have approximately same intensity.

The difference in the 2D peak shape arises from the difference in the band structure: due to interaction between two layers, bilayer graphene has a parabolic electron

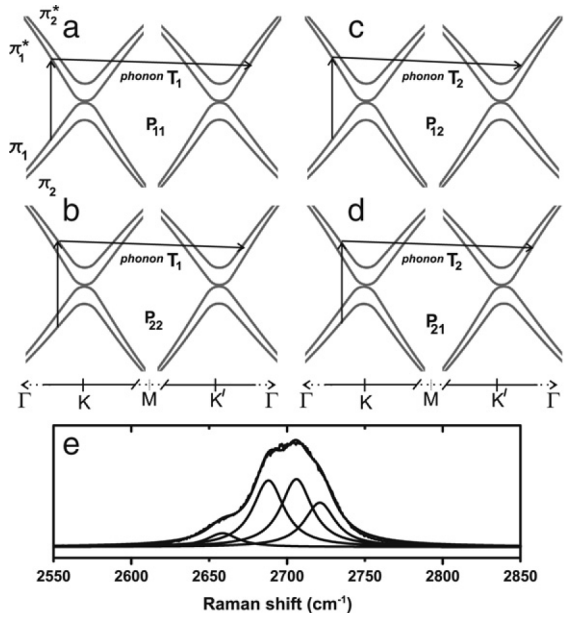

Figure 1.8: Raman scattering processes that give rise to the 2D band in bilayer graphene. Image adapted from Ref. [105].

dispersion relation with two conduction and two valence bands. As a result, there are four Raman scattering processes with different probabilities that lead to formation of the 2D peak (Fig. 1.8); the difference in the phonon energies associated with these processes comes from phonon energy dispersion.

The shape and width of the 2D peak can provide information about stacking order and relative orientation in few layer samples and is widely used to identify single and bilayer samples. However, it does not allow unambiguous thickness determination for thicker samples. For $N_{\text{layers}} > 5$ shape of the 2D peak becomes almost indistinguishable from that of bulk graphite [108].

Number of layers in sample up to 10 layers thick can be estimated from the intensity of the G peak. The G peak originates from the stretching of the sp^2 bonds between carbon atoms and is present in many carbon materials. Its intensity is proportional to the number of sp^2 bonds in the excited area and grows linearly with increasing number of graphene layers. For samples on silicon substrate, the G peak intensity is usually normalised to the intensity of silicon peak at 520 cm^{-1} to avoid variations in the signal intensity due to fluctuation of the excitation power.

The D peak at 1350 cm^{-1} is normally absent in samples produced by mechanical exfoliation as it requires a defect for its activation. However, spectra of CVD-grown samples usually contain it due to presence of grain boundaries. B. Kraus et al. [109] have studied the evolution of Raman spectra during laser-induced disassembling of single-crystal graphene into a network of interconnected nanocrystallites. As

the number of defect increases the Raman spectrum evolves as follows: the D' peak appears at $\sim$ 1620 cm^{-1}, the intensity ratio I_D/I_G increases and all peaks are broadened. At the end of this stage, broadening of the G and D' peaks causes them to merge into one broad feature around 1600 cm^{-1}.

Since the D peak is produced only in a small ($\sim$ 3 - 4 nm) region around defects, intensity ratio of the G and D peaks can be effectively used to estimate density of defects in the sample [109, 110]. Note that with further increase of disorder, as nanocrystallite graphene is transformed into low sp^3 amorphous carbon, the I_D/I_G ratio decreases towards zero. However, this stage is easily distinguishable by the absence of well-defined second-order peaks [110].

1.3.2.4 Effects of doping and strain on Raman spectrum

Due to its intrinsic sensitivity to phonon frequencies, Raman spectroscopy has become a popular method of measuring strain in crystalline and semi-crystalline materials. The change of interatomic distances caused by applied strain leads to the shift of the phonon frequencies, with tensile (compressive) strain generally giving softening (hardening) of phonon modes [108]. Since the 2D and G peaks in graphene originate from scattering on optical phonons, their position down-shifts with decreasing phonon frequency. The 2D peak experiences larger shift with applied strain because it originated from the second-order process that involves two phonons.

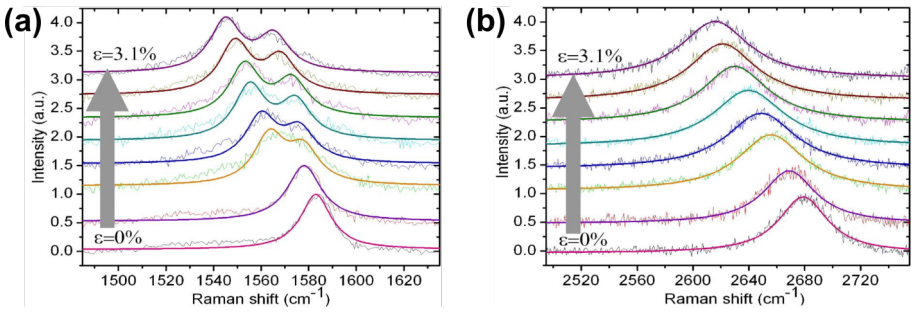

Figure 1.9: The evolution of the Raman G **(a)** and 2D **(b)** bands under increasing uniaxial strain. The splitting of the G peak is caused by the symmetry breaking between two sublattices, while the broadening of the 2D results from the strain-induced modification of the band structure. Images adapted from Ref. [111].

Uniaxial strain applied to graphene lowers the symmetry of the crystal lattice, causing both the G and 2D peaks to split into two components. Figure 1.9 plots the evolution of the Raman G and 2D peaks under increasing uniaxial strain. The G peak originates from a conventional first order Raman scattering process involving the doubly-degenerate zone-centre phonon mode. Since uniaxial strain breaks the

symmetry between the two sublattices, it resolves the phonon degeneracy at the Γ point [111, 112]. This causes the G peak to split into two components, one parallel and one perpendicular to the direction of strain, named G^+ and G^-. These components have different polarisation, allowing the sample orientation with respect to the strain direction to be determined using polarised Raman measurements [111].

The 2D peak, however, arises from the second-order, two-phonon Raman process, and the effects of the uniaxial strain on the 2D peak are more complex. The changes of the 2D peak shape and frequency under the applied strain are caused by both changes in phonon frequencies as well as changes in the band structure, i.e. deformation and displacement of the Dirac cones [111, 113]. The two distinct components of the 2D peak, $2D^+$ and $2D^-$, can be clearly resolved only when a significant amount of strain is applied along a high-symmetry direction [114].

As biaxial strain preserves the lattice symmetry, it does not cause any splitting of the Raman peaks [115–117].

Different types of strain can be distinguished by considering the relative rate of the peak position change as $\Delta\omega_{2D}/\Delta\omega_G$ depends on the type and direction of strain. For the zigzag (arm-chair) oriented uniaxial strain, $\Delta\omega^+_{2D}/\Delta\omega^+_G = 2.00(3.00)$ and $\Delta\omega^-_{2D}/\Delta\omega^-_G = 2.05(1.89)$ [112, 113, 118]. When the level of uniaxial strain is not high enough to resolve the two peak components, $\Delta\omega_{2D}/\Delta\omega_G$ can be approximated as 2.02 and 2.44 for strain along the zigzag and armchair direction respectively [90]. Biaxial strain leads to a larger $\Delta\omega_{2D}/\Delta\omega_G$ ratio with experimentally measured values ranging from 2.45 to 2.8 [115–117].

The position of the Fermi level in graphene plays an important role in many physical processes, such as light absorption, charge carrier transport and relaxation etc. The most accurate way of identifying it is through transport measurements, e.g. Shubnikov-de Haas oscillations, quantum Hall effect or $R(V_g)$ measurements. However, it requires electric contact to be created with graphene and might not be suitable for all types of samples.

The Fermi level position can be estimated from the Raman spectrum with a high degree of accuracy as many parameters of graphene Raman spectrum have a strong dependence on the carrier concentration (see Fig. 1.10). The G peak frequency increases and FWHM(G) decreases with increasing Fermi level shift of any sign. The intensity ratio of the 2D and G peaks I_{2D}/I_G has maximum value in pristine graphene and decrease with increasing doping.

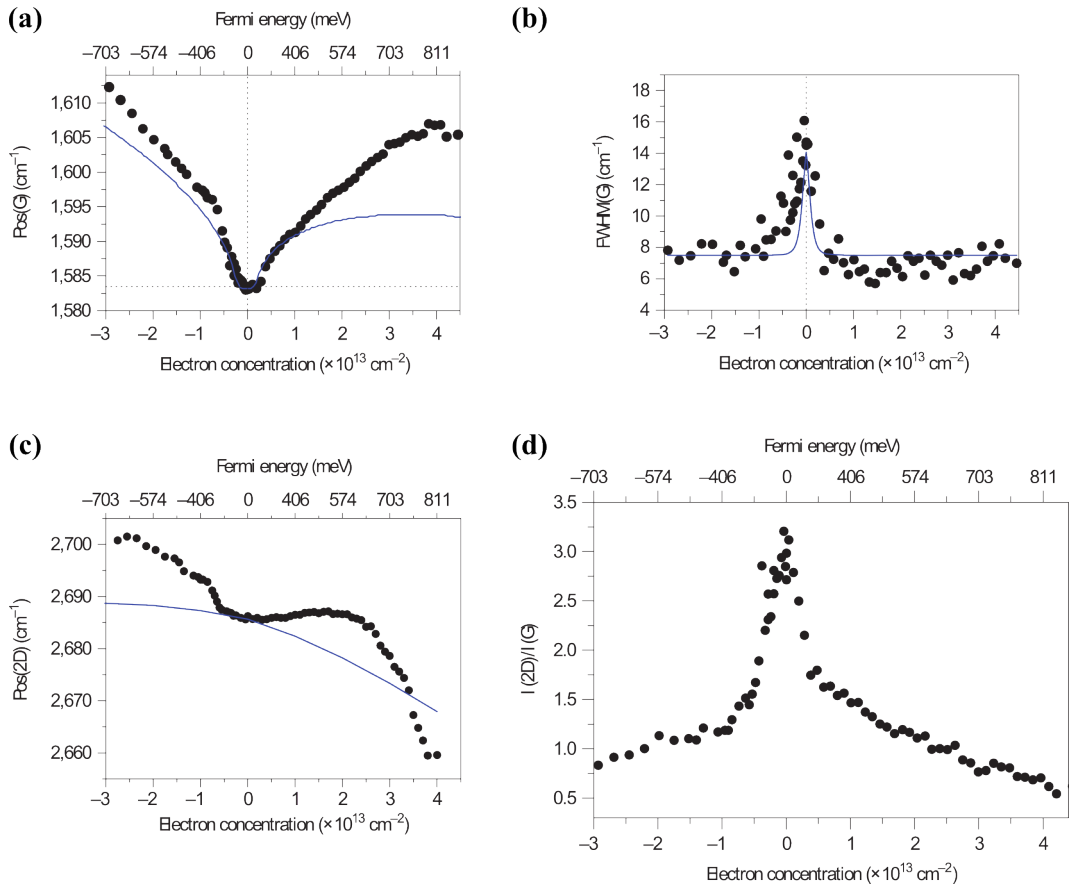

Figure 1.10: **(a)** Position and **(b)** FWHM of the Raman G band as a function of carrier concentration. **(c)** Position of the 2D peak for as a function of doping. **(d)** Intensity ratio of the 2D and G peak as a function of the Fermi level position. Images adapted from Ref. [119].

These three parameters show dependence only on the absolute value of the Fermi level shift and therefore do not allow different types of doping to be distinguished. Fortunately, the 2D peak shows different response to n- and p-doping as its frequency decreases (increases) with increasing electron (hole) doping (Fig. 1.10 b).

Up-shift of the G peak position is caused by the presence of Kohn anomalies in graphene [120]: strong electron-phonon coupling leads to softening of the phonon modes with wavevector $q \sim 2k_F$ where k_F is the Fermi-surface wavevector. When the Fermi level moves away from the Dirac point, the Kohn anomaly in graphene at the Γ point is removed causing stiffening of the E_{2G} phonon mode. The main contribution to homogeneous broadening of the G peak comes from the phonon decay into electron-hole pairs [120]. With increasing carrier concentration the electron-hole gap becomes larger than the phonon energy blocking the decay channels. This leads to sharpening of the G peak that saturates when the Fermi level shift is equal to

half of the phonon energy.

The total area under Raman peaks represents the probability of the corresponding scattering process [106]. The G peak arises from the single phonon scattering process whose probability is not affected by doping for $|\epsilon_F| < \hbar\omega_L/2$, where $\hbar\omega_L$ is the excitation energy. The 2D peak, however, originates from the second-order scattering process in which real electronic states serve as intermediate states. Therefore the area of the 2D peak is sensitive to the inelastic scattering rate of electrons that includes both e-ph and e-e scattering [108]. The latter increases with increasing carrier concentration, causing a decrease of A(2D) with increasing doping (Fig. 1.10).

1.4 Ultrafast photoluminescence

Ultrafast photoluminescence of graphene is a rather unexpected property for a zero-bandgap material. Due to the absence of a bandgap and ultrafast relaxation of photoexcited carrier no luminescence signal was expected from graphene. Indeed, for continuous wave excitation photoluminescence was observed only in chemically modified [121] or highly electrostatically doped graphene [68]. However, upon photoexcitation with ultrashort laser pulses, graphene produces a strong broadband luminescence signal with emission for energies both lower and higher than the excitation energy. The photoluminescence (PL) signal is unpolarised and angularly broad, and its intensity shows strong dependence on the excitation power [64, 70, 71].

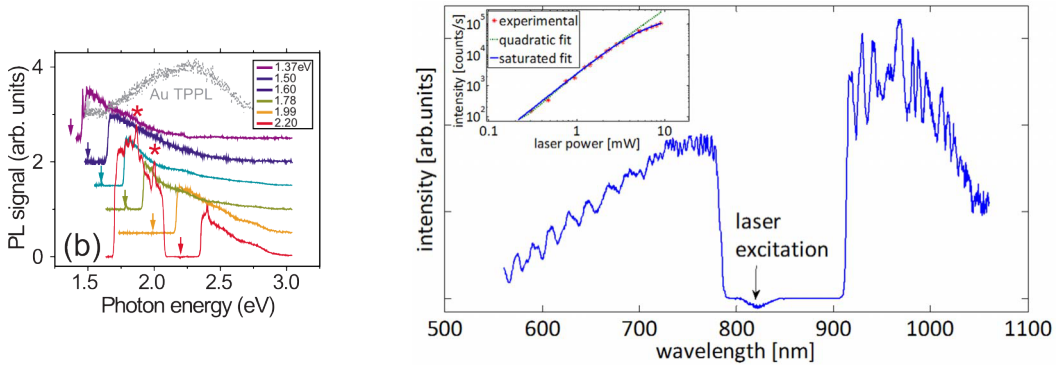

Figure 1.11: Spectrum of PL induced by excitation with 150 fs **(a)** and 7 ps **(b)** laser pulses. Images adapted from Refs. [64, 122].

Different PL spectra have been reported for various excitation pulse lengths. Figure 1.11 compares spectra of PL induced by 150 fs **(a)** and 7 ps **(b)** laser pulses. The PL produced upon femtosecond excitation show monotonous increase of intensity towards the lower energy end of the spectrum. The shape of femtosecond PL

spectrum does not show a strong dependence on the excitation energy, however, it varies strongly with increasing pump fluence [71]. For picosecond excitation, PL spectrum has approximately symmetric shape centred at the excitation wavelength that does not change with increasing pulse fluence [64].

Origin of this difference lies in the relative pulse duration compared to characteristic carrier relaxation times in graphene. Relaxation of photoexcited charge carriers consist of three main steps: first, within $\sim$ 10 fs after photoexcitation rapid e-e scattering leads to formation of hot Fermi-Dirac distribution [50, 63, 123]. This process is very efficient in graphene due to the linear energy dispersion that allows both energy and momentum conservation laws to be satisfied. This distribution then loses its energy due to scattering on optical phonons until after $\sim$ 500 fs equilibrium between two systems is achieved [57]. The final step of the relaxation process consists of an anharmonic decay of hot optical phonons into acoustic modes and happens on a $\sim$ 5 ps timescale [54].

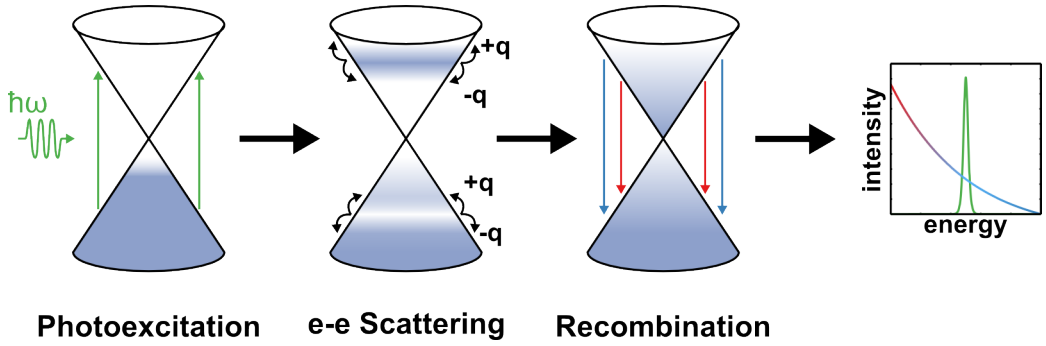

Figure 1.12: Origin of ultrafast PL. Spectrum of PL is defined by ultrafast scattering of photoexcited charge carriers.

PL signal originates from the recombination of hot electron distribution created by photoexcitation (Fig. 1.12). For femtosecond excitation, high instantaneous density of the photoexcited charge carriers leads to formation of a hot Fermi-Dirac distribution on a $\sim$ 10 fs timescale through rapid e-e scattering. The temperature of this distribution shows a strong dependence on the excitation pulse fluence, but it is to a large extent independent of the excitation energy. The PL spectrum corresponds to the spectrum of thermal emission and can extend well above the excitation energy.

In the case of picosecond excitation,the Fermi-Dirac distribution cannot be established as new charge carriers are created in the conduction and valence band at the rate comparable to the characteristic e-ph relaxation times. E-e scattering leads to almost instantaneous broadening of the laser-induced distribution, however, the

energy exchange between electrons is less efficient due to much lower carrier concentration.

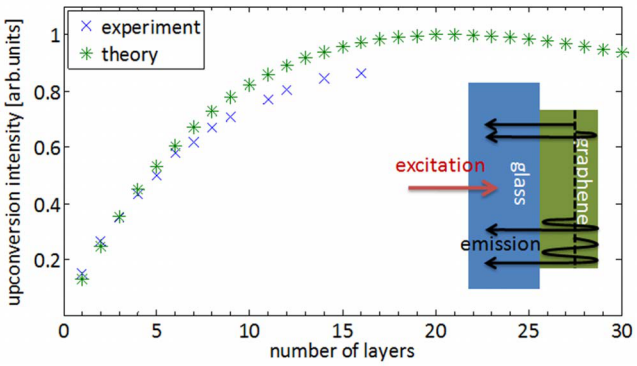

Figure 1.13: Intensity of ultrafast PL as a function of sample thickness. Image adapted from Ref. [64]

The ultrafast PL is not limited to single layer graphene samples. Figure 1.13 plots changes of PL intensity with varying sample thickness. For few layer graphene, PL intensity shows an approximately linear increase with increasing number of layers. However, after $N_{\text{layers}} \sim 10$ the increase rate slows down, with the PL intensity reaching a maximum value at $N_{\text{layers}} = 15 - 20$ and decreasing for thicker flakes; bulk graphite does not produce a detectable up-converted signal.

1.4.1 Two-temperature model

The temporal evolution of the hot electron distribution that gives rise to the ultrafast PL can be modelled using a set of coupled rate equations [54, 57, 71, 72]. This two-temperatures model is a slightly modified version of the model developed by Wang *et al.* [57] and Hale *et al.* [54] and is limited to the case of undoped graphene.

Due to ultrafast e-e scattering we can assume that at any given moment charge carriers are fully thermalised with each other and form a hot Fermi-Dirac distribution. Changes in the temperature of this distribution caused by the interaction with optical phonons can be described by the following differential equation:

$$\frac{dT_e}{dt} = \frac{I(t) - 2 \cdot \Gamma_{\text{ph}} \hbar\omega_{\text{ph}}}{C_e}, \tag{1.19}$$

where $I(t)$ is the absorbed laser irradiance, Γ_{ph} is the optical phonon generation rate, $\hbar\omega_{ph}$ is the optical phonon energy and C_e is the electronic heat capacity. The factor of 2 in Eq. 1.19 arises from the presence of both Γ and K point phonons. Since they have similar frequencies, we can simplify the calculation by treating them as

a single mode with energy $\hbar\omega_{ph} = 0.18$ eV. The phonon generation rate Γ_{ph} can be calculated using the following relation [54]:

$$\Gamma_{ph} = \alpha \int_{-\infty}^{+\infty} dE\, \nu(E)\nu(E - \hbar\omega_{ph}) \cdot [\rho_e - \rho_a]. \tag{1.20}$$

Here, $\nu(E)$ is the density of electronic states, ρ_e and ρ_e are the phonon emission and absorption probabilities, and α is electron-phonon coupling strength given by

$$\alpha = \frac{9}{4}\frac{\pi\beta^2}{\rho_0\omega_{ph}}, \tag{1.21}$$

where $\beta = 45$ eV/nm is the deformation potential, $\rho_0 = 7.6 \cdot 10^{-7}$ kg/m^2 is the density of graphene, and $v_F = 1 \cdot 10^6$ m/s is the Fermi velocity. The probability of emitting and absorbing a phonon for a given energy of electron ρ_e and ρ_a are given by

$$\begin{aligned} \rho_e &= f(E, T_e)\ (1 - f(E - \hbar\omega_{ph}, T_e))\ (n_{ph} + 1) \\ \rho_a &= f(E - \hbar\omega_{ph}, T_e)\ (1 - f(E, T_e))\ n_{ph}, \end{aligned} \tag{1.22}$$

where $f(E, T_e)$ is the Fermi-Dirac distribution and n_{ph} is the phonon occupation number.

The second differential equation that describes changes in the phonon occupation numbers has the following form

$$\frac{dn_{\mathrm{ph}}}{dt} = \frac{\Gamma_{\mathrm{ph}}}{M_{\mathrm{ph}}} - \frac{n_{\mathrm{ph}} - n^0_{\mathrm{ph}}}{\tau_{\mathrm{ph}}}. \tag{1.23}$$

The first term describes phonon generation by e-ph scattering and the second term corresponds to the anharmonic decay of optical phonons into acoustic modes. M_{ph} is the number of phonon modes per unit area that participate in e-ph scattering; it can be estimated by calculating the minimum and maximum momenta of phonons that can be generated by a hot electron:

$$M_{ph} = \frac{2}{4\pi}\left[\left(\frac{E_{\max}}{\hbar v_F}\right)^2 - \left(\frac{\omega_{ph}}{v_F}\right)^2\right], \tag{1.24}$$

where $E_{\max}$ is the maximum energy of hot electrons that can generate phonons. The factor of 2 arises from valley or phonon mode degeneracy for Γ and K phonon modes respectively. The temporal dynamics of electron and phonon temperatures following the photoexcitation can be calculated by numerically solving the pair of

coupled rate equations 1.19 and 1.23.

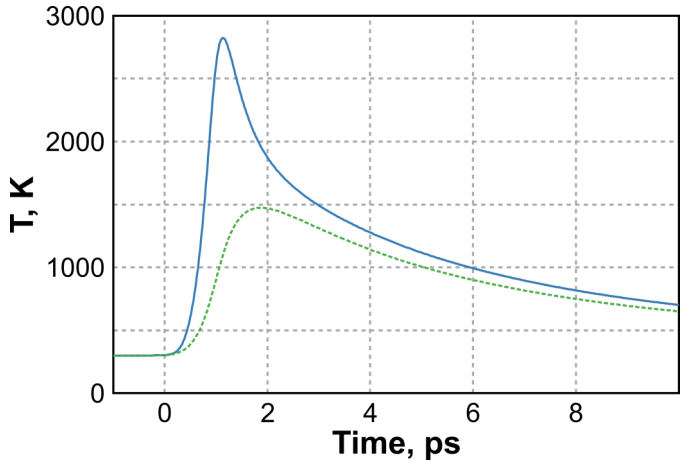

Figure 1.14: Temporal evolution of electron **(solid blue)** and phonon **(dashed green)** temperatures following the photoexcitation by a 180 fs laser with the fluence of 0.1 mJ/cm^2 calculated using the two-temperature model.

Figure 1.14 shows an example of electron and phonon temperature dynamics calculated using this model. Here the absorbed irradiance was defined as

$$I(t) = \frac{F_{ex}}{2\tau_{ex}\cosh(\frac{t(I)}{\tau_{ex}})}, \tag{1.25}$$

where $F_{ex} = 2.3$ μJ/cm^2 is the absorbed laser fluence and $\tau_{ex} = 180$ fs is the excitation pulse duration. The electronic heat capacity was calculated analytically in the high temperature limit [71]

$$c_e(T_e) = \frac{18\zeta(3)}{\pi(\hbar v_F)^2} k_B^3 T_e^2, \tag{1.26}$$

where $\zeta(3) = 1.202$ is the zeta function and k_B is the Boltzmann constant. Note that this model is not applicable for the case of picosecond excitation as the energy exchange between carriers is less efficient due to much lower instantaneous photoexcited carrier density [63, 123].

Chapter 2

Experimental techniques

2.1 Introduction

In this chapter, sample fabrication and characterisation techniques utilised in this thesis are described. Graphene samples were obtained by micromechanical cleavage of graphite and CVD growth on copper substrates. The number of layers in exfoliated samples was defined from optical contrast measurements. Using Raman spectroscopy, different sample characteristics, such as crystal quality, position of the Fermi level and the mechanical strain level were investigated and number of layers was confirmed. Contacted samples on Si/SiO_2 substrates for electro-optical measurements were fabricated using electron beam lithography.

At the end of the chapter, basics of ultrafast PL imaging and spectroscopy are described.

2.2 Sample fabrication and characterisation

Since the first experimental discovery of graphene in 2004 [9], a range of different graphene fabrication techniques have been developed, including chemical and shear exfoliation [124–126], epitaxial growth on silicon carbide [127–129] etc. Graphene samples produced by these methods vary in size, thickness and crystalline quality, therefore appropriate fabrication techniques must be used for a specific application. For research applications, the two most commonly used fabrication methods are mechanical exfoliation [9, 130, 131] and chemical vapour deposition on metallic foils [132–134].

2.2.1 Mechanical exfoliation

Majority of graphene samples presented in this thesis were obtained by mechanical exfoliation of natural graphite, the technique that was originally developed by Geim and Novoselov in 2004 [9]. Despite being unusable for industrial use due to small size and low outcome of monolayer flakes, this process allows producing single crystal samples of highest quality that are ideal for research and prototyping applications. In order to the increase size of fabricated graphene flakes, high quality natural graphite crystals with large size single crystal domains were used (Fig. 2.1 (a)).

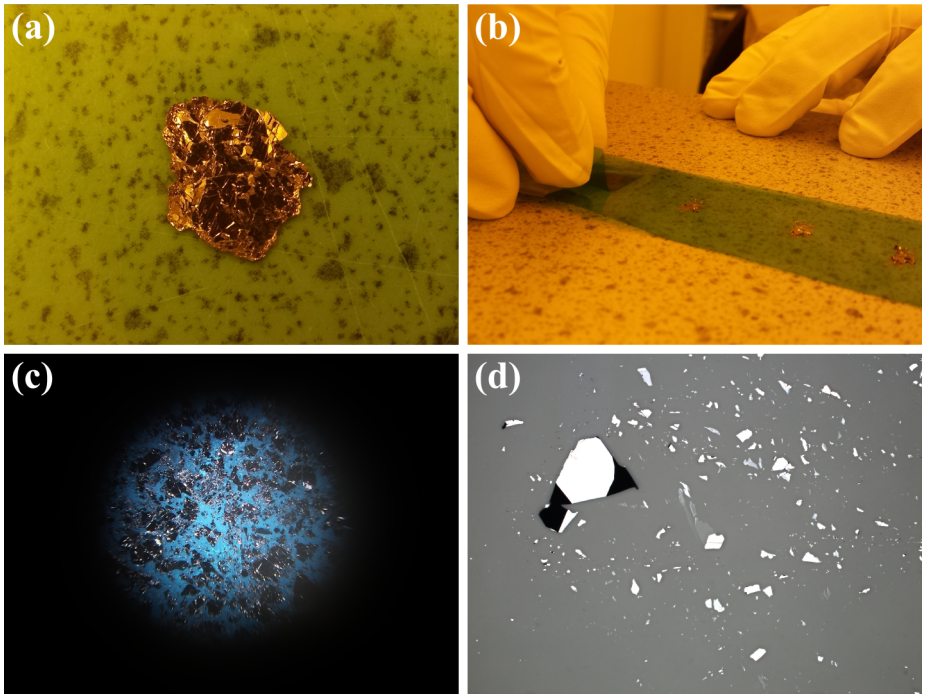

Figure 2.1: Basic steps of mechanical exfoliation process. **(a)** Top layers of graphite crystal are transferred onto a pre-cut piece of adhesive tape. **(b)** Graphite is repeatedly pealed using another peace of tape until desired thickness is achieved. **(c)** Photograph of graphite crystals after pealing is completed. **(d)** Optical micrograph of thin graphite crystals transferred onto a glass substrate showing large a few-layer graphene flake in the middle.

At the beginning of the fabrication process, surface layers of graphite, which might have been contaminated during transport and storage, are removed with adhesive tape. Regular office tape can be employed, however, the use of less adhesive tape (Nitto SWT 10+) allows glue residues on substrate and graphene flakes to be minimised. Clean underlying layers are then transferred to a small piece of pre-cut adhesive tape and pealed repeatedly until they look thin and translucent under a microscope (Fig. 2.1 (b-c)).

Substrate preparation is a crucial step of the fabrication process, since contamination of the substrate surface can result in a very low density of transferred flakes. Prior to the application of the tape, substrates are cleaned by immersion into boiling acetone for 30 minutes and consequent sonication in fresh acetone and isopropyl alcohol (IPA) for another 60 minutes. Finally, the substrates are treated with oxygen plasma to remove any remaining contaminants. Graphene flakes are transferred onto the cleaned substrate by pressing adhesive tape against it and then carefully pealing it off. It has been noticed that heating the substrate up before flake deposition leads to higher deposition density; however, it can also increase sample contamination due to tape residues.

2.2.2 CVD growth on copper substrate

Commercial applications of graphene require a fabrication method capable of producing large area samples at low cost. One of the most commonly used techniques is CVD growth of graphene on copper substrates. Chemical vapour deposition (CVD) is widely used in the semiconductor industry for thin film fabrication. In the typical CVD process, precursor gases at ambient temperature are fed into a reaction chamber containing a hot substrate. A chemical reaction occurring near or at the surface leads to deposition of a thin film on the substrate. By-products of the reaction and unreacted precursors are removed from the chamber by gas flow.

CVD growth of graphene on Cu substrate was first reported in 2009 by Li et al. [132] In this process, a graphene film is formed by thermochemical decomposition of hydrocarbons at the surface of hot metal which also acts as catalyst significantly lowering the energy barrier of pyrolysis. As copper has a very low carbon solubility, the majority of carbon involved in formation of graphene comes from hydrocarbon precursors. The first continuous layer of graphene formed on the copper substrate acts as a barrier separating the precursors from the catalyst. Therefore, CVD growth of graphene on Cu substrates is a self-limiting process resulting in the majority of graphene being only one layer thick.

Graphene samples were grown in a cold wall furnace at 1000° C using mixture of hydrogen and methane and transferred onto glass or silicon substrate using the wet transfer method. First, copper foil with graphene film was covered by thin layer of polymethyl methacrylate (PMMA) and put into a desiccator to remove any remaining solvent. After the metal film was etched using ammonium persulfate solution, the graphene/PMMA stack was rinsed in de-ionised water and transferred onto the target substrate. In the final step, the polymer layer was removed by

immersion into hot acetone, the substrate was then washed in IPA and dried nitrogen flow to remove any remaining solvents.

2.2.3 Graphene visibility and thickness identification

Micromechanical cleavage of graphite crystals results in the distribution of flakes with different thickness, with monolayer and few-layer graphene being a great minority among much thicker flakes. Search and identification of such samples is a crucial part of the fabrication process. Fortunately, graphene shows an exceptionally high absorbance of $\pi\alpha = 2.293\%$ per one atomic layer which is independent of wavelength for excitation in the near-infrared to ultraviolet range [32]. It means that even monolayer graphene flakes are visible under wide-field microscope on most substrates. Figure 2.2 **(a)** shows an example of a graphene sample with several areas of different thickness deposited onto on $180\,\mu m$ thick glass substrate. The contrast of the digital image has been artificially increased to make the monolayer part clearly visible.

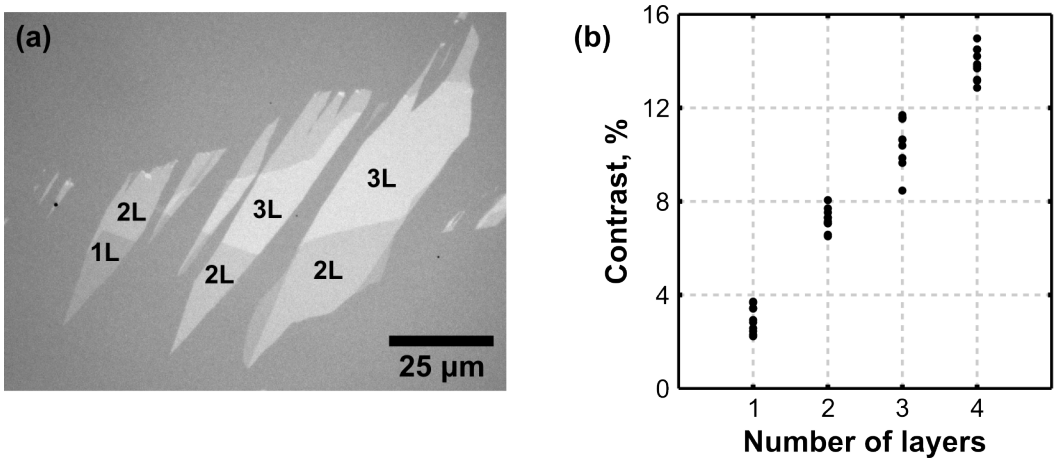

Figure 2.2: **(a)** Optical micrograph of a few-layer graphene sample on a glass substrate. Contrast of the image was digitally increased to make monolayer part visible. **(b)** Statistics of optical contrast measurements for 40 different samples showing a step-like change in the optical contrast of graphene with increasing number of layers.

Optical contrast measurement is a well-established method for identifying the number of layers in graphene samples [104]. The optical contrast of graphene flakes can be defined as

$$C = (I_{gr} - I_s)/I_s \cdot 100\%,$$

where I_{gr} is the reflection intensity of the graphene flake and I_s is the intensity of the substrate. Figure 2.2 **(b)** shows optical contrast measurements for 40 graphene sam-

ples of different thickness. Even though non-uniform illumination and interaction with substrate creates variation of contrast for the flakes with the same thickness, a step-like change with increasing number of layers is clearly visible and allows an accurate determination of number of layers for samples up to 9 layers thick [104].

Monolayer samples on transparent substrates provide only 3% of contrast making them hardly visible and extremely difficult to find. The visibility of graphene flakes can be increased by using n-doped silicon substrate covered with a thin layer of thermally-grown SiO_2. In this case, highly doped Si, dioxide layer and graphene create a Fabry-Perot structure, and the contrast provided by graphene flakes can be maximised by choosing an appropriate combination of oxide layer thickness and illumination light wavelength. For the commonly used 285 nm thick SiO_2, the maximum contrast is achieved using green light (550 nm).

2.2.4 Raman spectroscopy

After the fabrication process was completed and appropriate samples were identified with an optical microscope, various sample properties, such as number of layers, Fermi level position and defect density, were investigated using Raman spectroscopy.

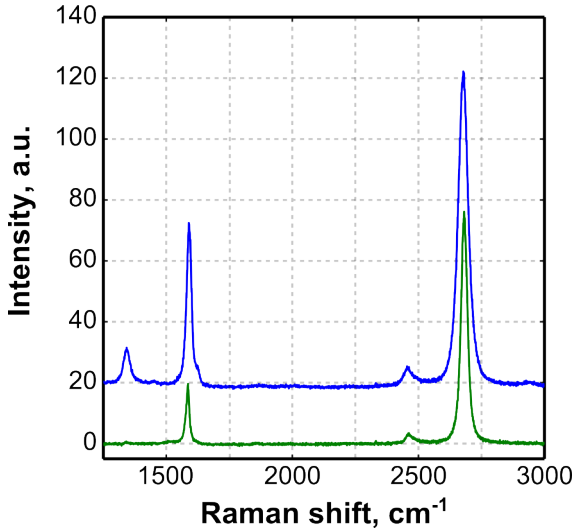

Figure 2.3: Example of Raman spectra for exfoliated **(green)** and CVD-grown **(blue)** graphene samples showing all major peaks. The baseline of the spectra have been shifted for clarity.

Raman spectra were collected using a Renishaw RM1000 Raman microscope: a 532 nm excitation beam with power of 60 mW was focused onto the sample using a 50x lens, resulting in excitation spot with diameter $d < 1.5\,\mu m$. In order to avoid optically damaging the graphene, a 1 OD neutral density filter was used to reduce

the laser intensity. The excitation wavelength was blocked by high extinction low-pass filters and the Raman signal was detected using thermoelectrically cooled CCD detector. High spectral resolution of $< 1\text{cm}^{-1}$ allows the accurate determination of the peak positions that can be used to estimate doping and strain levels in the sample. To ensure that measured Raman shifts are consistent, the system was calibrated prior to measurements using the high intensity Si peak at 520 cm^{-1}. All measurements were performed at room temperature and in ambient conditions.

Figure 2.3 shows the Raman spectra of monolayer graphene samples produced by mechanical exfoliation **(green)** and CVD growth **(blue)**; the baselines of spectra have been shifted for clarity. The 2D peak at 2680 cm^{-1} has a symmetric shape and FWHM of less than 50 cm^{-1} confirming that both samples are only one layer thick. The defect-induced D peak at 1350 cm^{-1} in the CVD sample indicates presence of structural defects while reduced intensity ratio of the 2D and G peak suggest a higher level of doping, most likely due to charged impurities introduced during the fabrication process.

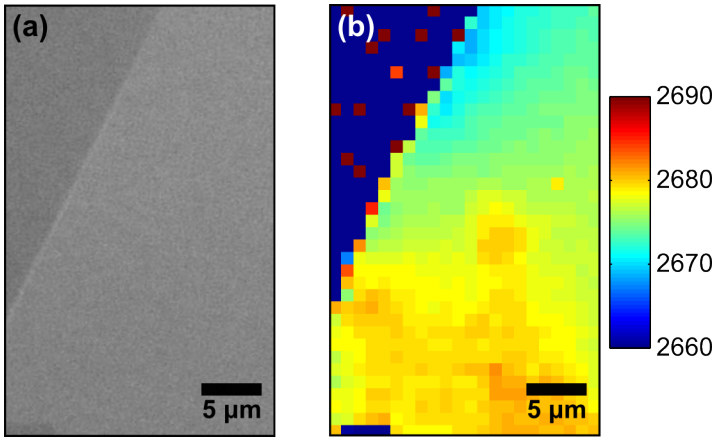

Figure 2.4: **(a)** Optical micrograph of a monolayer graphene sample on a glass substrate. **(b)** Raman map of the corresponding area plotting the position of the Raman 2D peak.

Maps plotting various parameters of the Raman spectrum can be constructed by recording Raman spectra for different positions of excitation spot on the sample. Figure 2.4 **(b)** shows the strain-induced variation of the 2D peak position in exfoliated monolayer sample on glass substrate.

2.2.5 Electron beam lithography

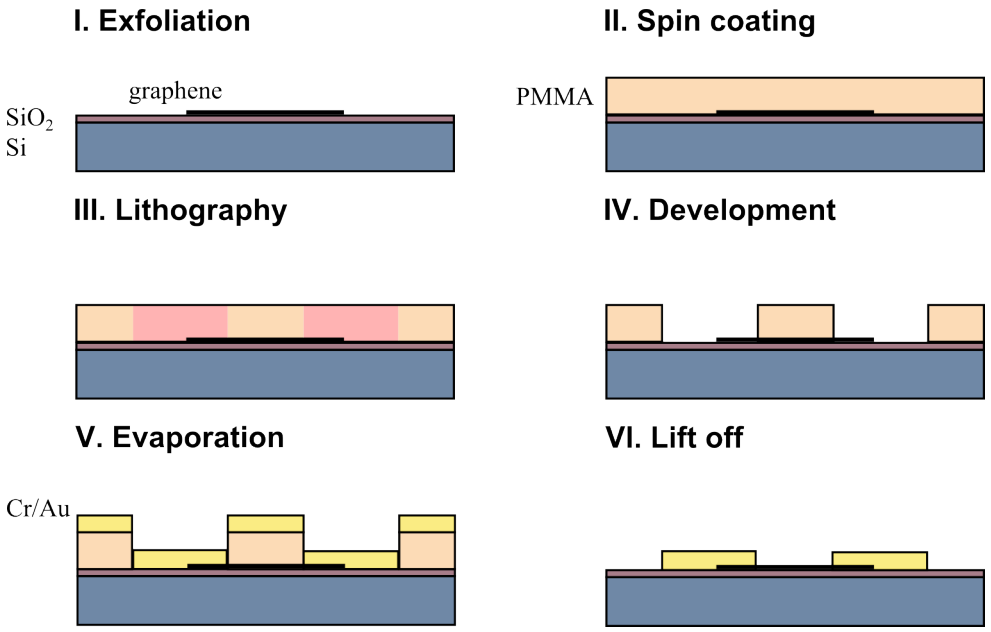

Figure 2.5: Basic steps of contacted sample fabrication. **(I)** Graphene flake is exfoliated onto silicon substrate. **(II)** Thin layer of PMMA is spun onto the substrate. **(III)** Contacts pattern is exposed in the the PMMA layer. **(IV)** Exposed areas of the PMMA are removed during development. **(V)** Sample is coated with thermally evaporated metal film. **(VI)** Unexposed PMMA is dissolved in hot acetone, leaving only the metal film deposited directly onto the substrate.

Contacted graphene devices on Si/SiO_2 substrates used for electro-optical measurements were created using electron beam lithography. The main steps of the fabrication process are illustrated in Figure 2.5. Firstly, a substrate with deposited graphene flakes is covered with 400 nm thick layer of positive electron beam resist (PMMA) using spin coating technique. After the location of a suitable graphene flake has been identified using wide-field microscope, the pattern defining the contacts is exposed in the PMMA layer. Exposure to electron beam causes the breaking of polymer chains allowing exposed areas to be selectively removed. The trenches revealed after photoresist development are filled with thermally evaporated chromium and gold (5 nm and 60 nm respective layer thickness). Unexposed areas of PMMA are removed by immersing the substrate into hot acetone. Finally, the sample is washed in IPA and blow dried with N_2 to remove any remaining residues.

2.2.6 R(V_g) measurements

A field-effect transistor structure created by graphene, oxide layer and silicon can be used to both measure and control the Fermi level position in graphene. By applying a voltage between the highly-doped silicon layer and one of the gold contacts, electrons can be injected or depleted from the graphene.

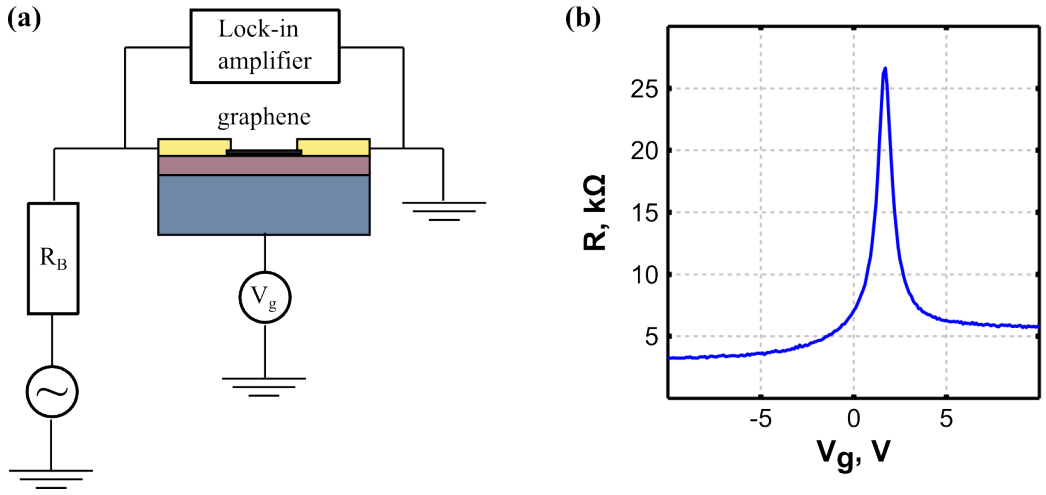

Figure 2.6: **(a)** Schematic of the experimental set-up for R(V_g) measurements. **(b)** Typical R(V_g) dependence of monolayer graphene sample. Resistance peak at 1.7 V occurs when the Fermi level crosses the Dirac point.

The number of injected charge carriers can be calculated using the plane plate capacitor equation:

$$n = \frac{\epsilon\epsilon_0 V_g}{de} = 2.16 \times 10^{11} \times V_g \ [\mathrm{cm}^{-2}], \tag{2.1}$$

where $\epsilon = 3.9$ is the permittivity of SiO_2, ϵ_0 is the permittivity of free space, V_g is applied gate voltage, d is the thickness of dioxide layer, and e is the charge of electron. Taking into account the density of states in graphene [12]

$$\nu(E) = dN/dE = 2|E|/\pi\hbar^2 v_F^2, \tag{2.2}$$

the Fermi level shift induced by electrostatic gating can be calculated as

$$\epsilon_F = 59.6\sqrt{V_G} \ [\mathrm{meV}]. \tag{2.3}$$

The position of the Fermi level can be identified by recording sample resistance as a function of the applied gate voltage: when the Fermi level is positioned exactly at the Dirac point, resistance of graphene reaches a maximum value due to the van-

ishing density of states. In pristine graphene, this occurs when no voltage is applied to the gate electrode; however, charged impurities created during the fabrication process, as well as interaction with the underlying substrate, can lead to non-zero chemical doping.

Figure 2.6 **(a)** a shows schematic of the experimental set-up for $R(V_g)$ measurements. The ballast resistor R_B has resistance of $10M\Omega$, which is much higher than the expected resistance of graphene sample (typical $R < 20\,k\Omega$). Changes of the overall circuit resistance due to the variation of graphene resistance are less than 1%. Therefore, current can be assumed to be constant and sample resistance can be calculated from the voltage drop across the sample. Figure 2.6 (b) shows an example of the $R(V_g)$ dependence of monolayer graphene sample. The resistance peak is located at 1.7 V indicating that the Fermi level in the sample is shifted down from Dirac point by 77 meV.

2.2.7 Atomic force microscopy

Atomic force microscopy (AFM) is a high-resolution microscopy technique that is widely used to image the surface topography of a sample. The capacity to investigate both conductive and insulating samples in a wide range of experimental conditions, including measurement in air and under liquid, has made AFM the most commonly used type of scanning probe microscopy techniques [135].

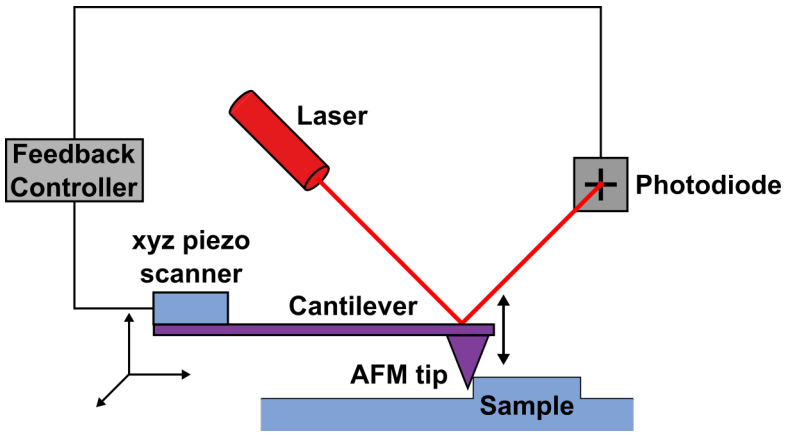

Figure 2.7: Schematic diagram of atomic force microscope.

The basic operating principle of AFM is illustrated in Figure 2.7. A sharp tip mounted at the end of a flexible cantilever beam is brought into contact with a sample, and the surface topography is investigated by measuring the change in the force between the cantilever tip and the sample. The bending of the cantilever caused by the repulsive or attractive force experienced by the AFM tip is recorded using

the laser light reflected from the surface of the cantilever. The feedback controller is used to adjust the vertical distance between the tip and the sample surface. The position of the cantilever is controlled using a 3-axis piezoelectric scanner, and the image is created by raster-scanning the probe across the surface of the sample.

The two most commonly used AFM imaging modes are contact (static) and tapping modes. In constant mode, the signal from the four-segment photodetector registering the deflection of the cantilever is used to keep the tip-to-surface distance constant. In tapping mode, the cantilever is excited into oscillation near its resonant frequency using a piezoelectric driver. The interaction with the substrate leads to damping of the oscillation, and the feedback loop is used adjust the probe vertical position in order to keep the oscillation amplitude constant.

Alongside with investigating surface topography, the tapping mode allows different sample properties, such as adhesion and viscoelastic properties, to be investigated by recording the difference in phase between the driving signal and cantilever oscillations.

The lateral resolution of the AFM is limited by the size of the tip, while the vertical resolution is defined by the sensitivity of the piezoelectric material and can be as high a fraction of an angstrom. The AFM tips are usually made out of silicon or silicon nitride using MEMS technology and have an end radius of 15-40 nm.

2.3 Ultrafast optical measurements

Ultrafast spectroscopy utilises short pulse excitation to probe transient processes in a system. Pioneering work in this field was done in 1949 by G. Porter et. al. [136], who studied free radicals involved in the photochemical decomposition of carbon disulphide using 4 ms light pulses generated by photography flashes. For the development of flash photolysis technique, Ronald Norrish and George Porter were awarded the Nobel Prize in Chemistry in 1967.

Great improvement in temporal resolution was achieved in the mid-1960s with invention of mode-locked ruby [137] and Nd:glass [138] lasers. Pulses with picosecond duration allowed much faster processes, such as electron transfer reactions, energy redistribution in molecules and relaxation in semiconductors, to be studied [139]. Measurement in the femtosecond time domain became available in 1980s after the invention of the colliding-pulse mode-locked dye laser [140]. Currently the shortest available isolated laser pulse has duration of 67 attoseconds and is generated using the double optical gating technique [141].

Besides providing high temporal resolution, pulsed excitation allows very high peak powers to be achieved. This property makes it extremely useful for studying nonlinear phenomena that have a strong dependence on incident power. Some of these effects cannot be observed in the steady-state excitation regime as CW power required to achieve a detectable signal would be much higher that the optical damage threshold.

2.3.1 Laser systems

PL imaging and photomodification were performed using a picosecond optical parametrical oscillator (Levante IR ps, APE). Optical parametrical oscillator (OPOs) are used to convert high energy incoming "pump" photon into two lower energy photons with their frequencies linked by the condition:

$$\omega_{\text{signal}} + \omega_{\text{idler}} = \omega_{\text{pump}}. \tag{2.4}$$

The higher and the lower frequency outputs of OPO are historically called signal and idler respectively. The frequency of both outputs can be tuned simultaneously by changing the nonlinear crystal temperature and phase-matching conditions.

The Levante OPO is pumped by a frequency-doubled output of a neodymium-doped yttrium orthovanadate (ND:YVO4) seed laser; using 532 nm pump photon, the wavelength of the OPO outputs can be tuned continuously in the 690 - 990 nm range for the signal and in the 1150 - 2300 nm range for the idler. Laser pulses are generated with a 76 MHz repetition rate and have duration of 6 ps. The fundamental mode of the seed laser centred at 1064 nm is also available and was used in some measurements.

Higher temporal resolution required for correlation measurements was achieved using a Ti:sapphire mode-locked laser (Mira 900D, Coherent Inc). Basic operational principles of Ti:sapphire mode-locked laser can be described as follows: a continuous wave pump laser induces fluorescence in a sapphire crystal doped with titanium ions, with emission ranging from 650 to 1100 nm. Continuous wave lasing starts in the laser cavity with many modes competing for amplification. If the individual phase of these modes is not fixed and can change randomly over time, interference between different modes will cause beating effects, i.e. random fluctuation of laser intensity. However, if the phase of each mode is locked and they oscillate in phase, constructive interference will lead to the formation of short, intense pulses of light. The repetition rate of these pulses is defined by the time it takes for light to make one round-trip in the cavity.

The phase-locking in the Mira 900D laser is achieved using the Kerr-lens mode-locking method. When high-intensity light travels through the Ti:sapphire crystal interaction with the electric field of the light causes changes in its refractive index. As the beam has a non-uniform power density distribution, the maximum change occurs in the centre of the beam, and the crystal acts as a lens narrowing diameter of the beam. By using an aperture with a diameter smaller than the cross-section of the CW beam, low-intensity light can be attenuated and high-intensity partially phase-locked pulses can be amplified, driving the mode-locking process.

The Mira 900D is pumped by a 532 nm (Verdi V10,Coherent) solid state laser and produces 180 fs pulses at a 76 MHz repetition rate. The wavelength of these pulses can be tuned in the 660 - 990 nm range, with the maximum laser intensity achieved around 800 nm.

2.3.2 Ultrafast photoluminescence imaging and spectroscopy

Ultrafast PL imaging and spectroscopy were performed using adapted inverted confocal microscope (IX71, Olympus). Near-infrared excitation beam with a wavelength in the 775 - 1064 nm range was carefully aligned into the microscope through a confocal scan unit (Fluoview 300, Olympus). To achieve the smallest possible size of the excitation spot, the diameter of the laser beam was enlarged by the set of beam expanders ensuring that the back aperture of the microscope lens was filled completely.

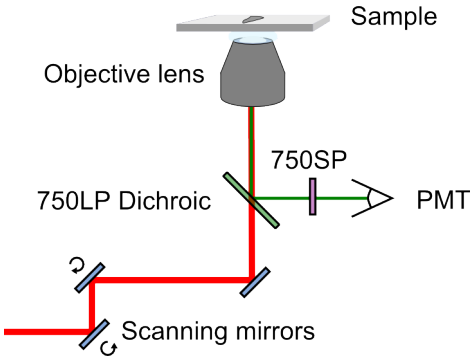

Figure 2.8: Internal alignment of the confocal microscope used for PL imaging. Excitation spot is scanned across the sample by the set of oscillating mirrors. Intensity of the PL signal, isolated with the edge-pass filters, is recorded by the photomultiplier tube.

The laser beam was focused onto the sample using either an Olympus UPLSAPO 20X lens or Olympus UPLSAPO 60XW water immersion lens. The signal generated in graphene was collected in the backwards direction and detected by the photomul-

tiplier tube (R3896, Hamamatsu) for integrated intensity measurements or by the spectrometer with cooled CCD detector (Shamrock SR-303i, Andor Technology) for spectroscopic studies.

PL images were constructed by raster-scanning the laser spot across the sample using oscillating mirrors and recording the intensity of up-converted PL as a function of position on the sample. The PL generation process has a relatively low efficiency (QE $\sim 10^{-9}$), therefore a set of appropriate high extinction edge pass filters must be used. Up-converted PL signal was isolated using 750 nm long-pass (LP) dichroic mirror followed by a set of two 750 nm short-pass (SP) filters (see Fig. 2.8).

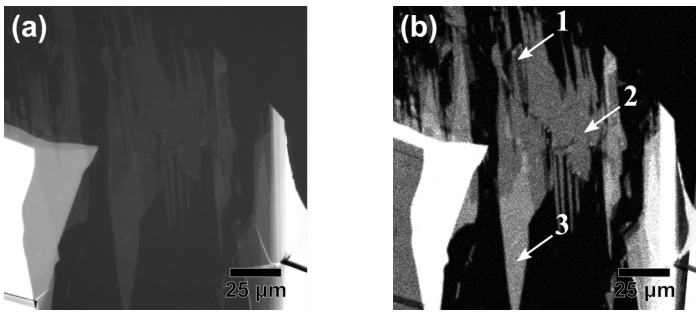

Figure 2.9: **(a)** Optical microscope image of a few layer graphene sample on a glass substrate. **(b)** Up-converted PL image of the same sample; numbers indicate thickness of the corresponding area.

Figure 2.9 compares images of a graphene sample on a glass substrate created using wide-field optical microscopy **(a)** and up-converted PL imaging **(b)**. The PL image has a much higher contrast, making monolayer and bilayer areas of the sample clearly visible. Areas of bulk graphite appear dark in the PL image due to non-monotonous dependence of the PL intensity on sample thickness. The intensity of the PL increases with increasing number of layers for thin samples, reaching maximum at ∼15-20 layers and decreasing for thicker flakes.

PL imaging becomes particularly useful when visibility of graphene is obscured by sample contamination, e.g. PMMA residues from the wet transfer process. Figure 2.10 shows examples of optical and PL images of a CVD-grown graphene sample. Contrast of the optical micrograph is too low to resolve any details or distinguish between graphene and PMMA residues.

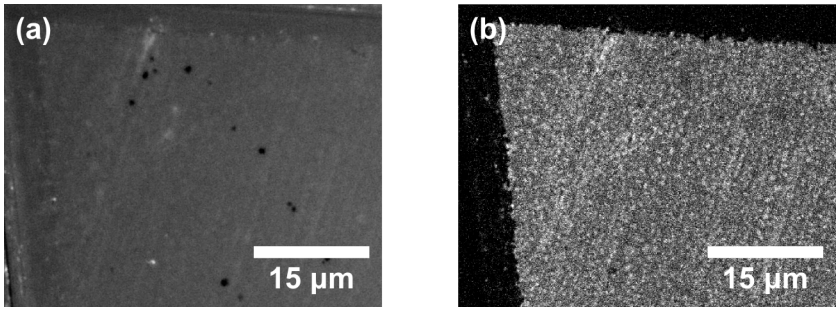

Figure 2.10: Wide-field microscopy **(a)** and up-converted PL **(b)** images of a CVD-grown graphene sample transferred onto a glass substrate.

In the PL image only graphene is visible as up-converted signal produced by residues is weak compared to graphene signal. Bright spots in the PL images correspond to patches of bilayer graphene created during the growth process.

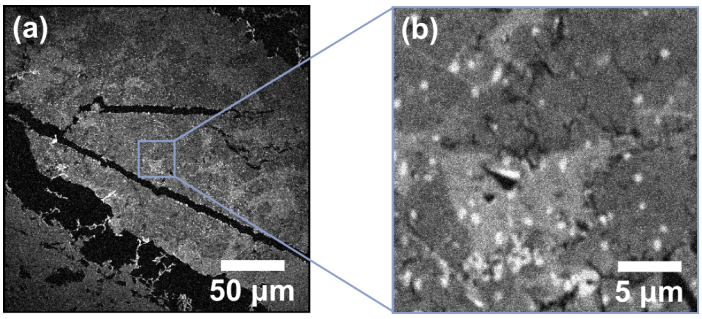

Figure 2.11: PL image of a CVD-grown graphene on a glass substrate showing the full field of view accessible with the 60x lens **(a)** and magnified image of the central region **(b).**

The confocal microscope system is controlled by the Fluoview software, which allows a range of different measurements to be performed. The size and position of the raster-scanned region can be chosen arbitrarily, allowing only a small portion of the sample to be investigated. Figure 2.11 shows PL images of a CVD sample constructed by raster-scanning the full field of view (235 μm $\times$ 235 μm for 60x lens) **(a)** and only the 23 μm $\times$ 23 μm central area **(b)**. Besides in-plane imaging, a depth scan of the sample can be taken by varying the focal plane position using the

motorised microscope stage. Different scan parameters, such as raster scan speed and number or repetition, can be controlled.

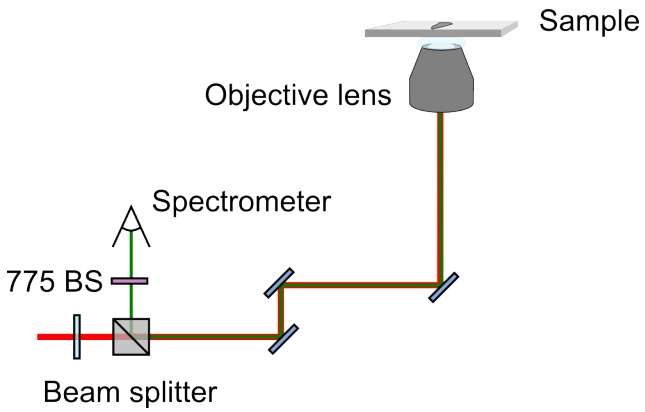

Figure 2.12: Schematics of the experimental set up for ultrafast PL spectroscopy. The PL signal collected in the backwards direction is isolated using a polarising beam splitter; the backscattered excitation light is blocked by a band-stop filter.

Frequency resolved information about PL was obtained using the Hamrock SR-303i spectrometer with Andor iDUS thermoelectrically cooled CCD detector. As the PL signal does not show a polarisation dependence, it can be effectively isolated using a polarising beam splitter (Fig. 2.12). The remaining excitation beam was blocked by a pair of 775 nm high-extinction band-stop filters (NF785-33, Thorlabs), allowing both up-converted and down-converted PL signal to be registered at the same time. During the measurements CCD detector was cooled down to $-55°$ C to reduce the thermal noise level.

Chapter 3

Photomodification of graphene with near-infrared laser pulses

3.1 Introduction

In this chapter, the modification of graphene samples caused by interaction with near-infrared picosecond laser pulses is investigated using ultrafast photoluminescence measurements. In recent years much research has been focused on the ultrafast optical properties of graphene: the nonlinear optical response of graphene has been studied using frequency mixing technique [36], transient absorption and photoemissions measurements have provided vital information about hot carrier lifetimes and relaxation mechanisms [54, 57, 59, 60, 142]. With extremely high instantaneous temperatures reached with pulsed laser excitation, it is of great importance to ensure that samples are not modified in any way during the measurements. Several experimental and theoretical studies have defined the optical damage threshold of graphene to be of the order of 100 mJ/cm^2, though laser-induced defects in CVD-grown graphene have been reported for pulse fluences as low as 14 mJ/cm^2 [101].

Near-infrared excitation pulses were focused onto the samples and modification of graphene was investigated by monitoring changes in the up-converted PL signal. It was found that even for pulse fluences orders of magnitude lower than the damage threshold the interaction with short intense pulses leads to a stable, localised decrease of PL intensity. The changes induced in graphene show remarkable long-term stability, however, they can be reversed completely through solvent treatment or thermal annealing. Samples with different number of layers show very similar temporal dynamic of photomodification that is only weakly dependent on the excitation wavelength. Strong environmental sensitivity of the photomodification process sug-

gests that it is mediated by adsorption of atmospheric gas molecules onto the surface of graphene.

3.2 Photoinduced reduction of photoluminescence intensity

To investigate the effects of near-infrared pulsed laser excitation on graphene, the picosecond excitation light generated by the Levante OPO was focused onto graphene samples using a 60x water immersion lens and changes of the sample properties were monitored using ultrafast PL imaging. Single and few-layer graphene samples were fabricated by mechanical exfoliation and deposited onto $180 - \mu m$-thick glass substrates. The number of layers in individual samples was estimated by optical contrast measurements [104] and confirmed using Raman spectroscopy [143].

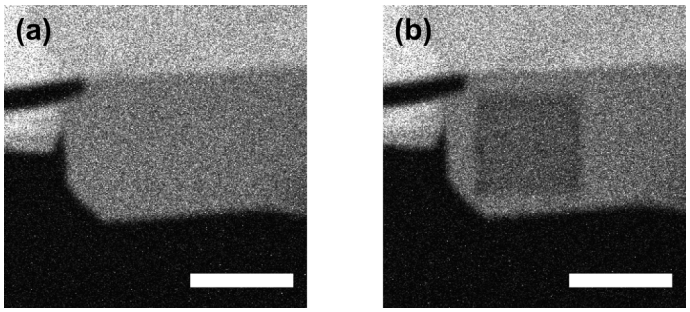

Figure 3.1: **(a)** PL images of a pristine monolayer sample on a glass substrate **(b)** PL image of the sample after photoexcitation with 3 mJ/cm^2 laser light centred at 815 nm for duration of 8 minutes. The dark square corresponds to the photoexcited region. All scale bars, $5\mu m$.

Prior to photoexcitation, an image of the sample was created using the up-converted PL signal, and the position and size of the area to be photoexcited were defined using Fluoview software. In order to minimise changes induced in the sample during PL imaging, laser fluence was kept below 0.2 mJ/cm^2. For the photomodification, the laser beam with fluence in the range of 1-3 mJ/cm^2 was raster-scanned over the designated area. The total time of the sample excitation was controlled by varying the number of raster-scans.

Figure 3.1 shows the PL image of a graphene flake before **(a)** and after **(b)** excitation with 3 mJ/cm^2 pulses for duration of 8 minutes. The photoexcited region can be clearly seen in Fig. 3.1 **(b)** as interaction with the laser light has led to stable and highly localised reduction of PL intensity.

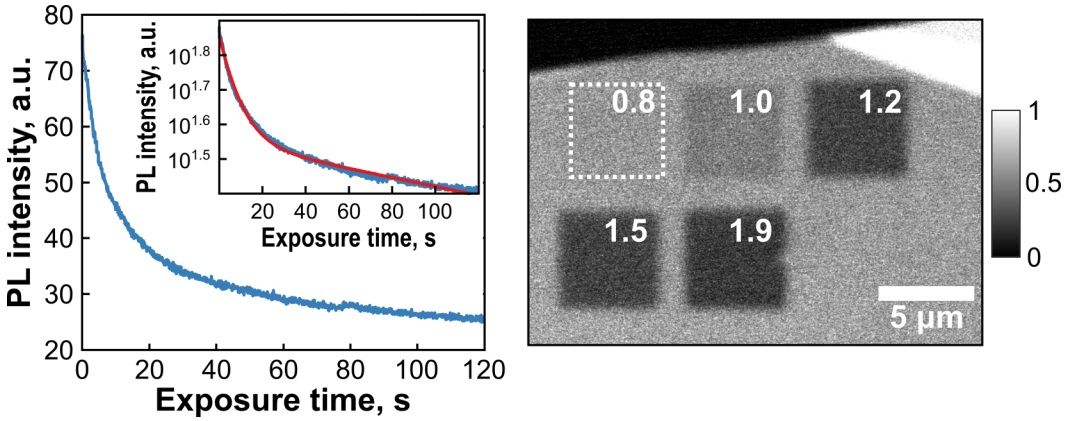

Figure 3.2: **(left)** Dependence of the PL intensity on the total exposure time for excitation with 3 mJ/cm^2 pulses for a duration of 2 minutes. **(Inset)** A logarithmic plot of the PL intensity decrease. The red line corresponds to a bi-exponential fit of the data. **(right)** A PL image of a monolayer sample showing several square regions exposed to various fluences of 879 nm radiation for one minute. Numbers indicate excitation fluence in mJ/cm^2 that was used to modify selected region.

The decrease of the PL intensity (I(PL)) with increasing exposure time shows approximately bi-exponential behaviour: a fast initial drop is followed by a slow decline that saturates at ∼20-30% of original value. Figure 3.2 **(left)** plots the I(PL) dependence on the total exposure time for excitation with 3 mJ/cm^2 pulses. The inset of Figure 3.2 **(left)** shows the semi-logarithmic plot of the PL intensity decrease; the red line represents a bi-exponential fit of the data.

The reduction of the PL intensity becomes faster with increasing excitation power. Right side of Figure 3.2 shows the PL image of a monolayer flake with several square regions exposed to different fluences of 879 nm radiation for duration of 1 minute; the numbers in the image indicate the pulse fluence in mJ/cm^2 that was used to modify the corresoponding area. The regions modified with higher pulse fluence show a stronger decrease of the PL intensity until the onset of saturation.

The total excitation time required to achieve a certain degree of reduction in the PL intensity scales linearly with the size of the raster-scanned area. This indicates that the PL intensity decrease depends only on the total exposure of each individual region suggesting that photomodification is an accumulated effect of interaction with individual pulses and not a result of steady-state heating.

The photoinduced reduction of the PL intensity is not limited to mechanically exfoliated flakes, and CVD-grown graphene samples show identical behaviour upon ultrashort pulse excitation. Figure 3.3 **(a)** shows the PL image of a sample obtained byCVD growth on copper substrate and transferred onto a 180-μm-thick glass cover slip. Majority of the sample consists of monolayer graphene, with small patches of bilayer that appear as bright spots in the PL image.

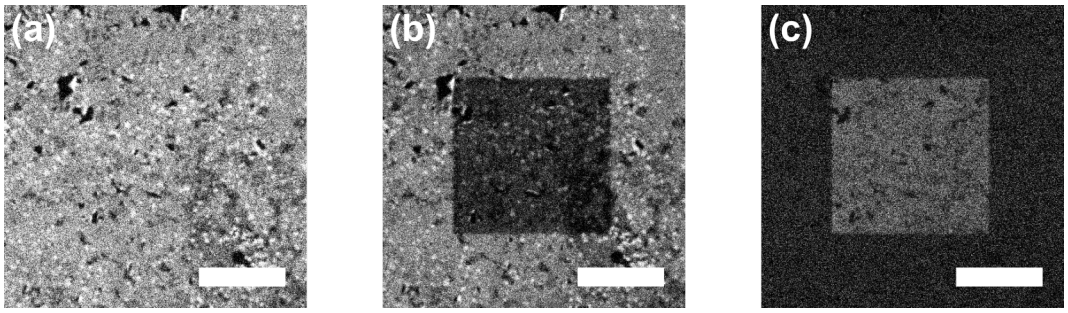

Figure 3.3: **(a)** PL image of a CVD-grown graphene sample transferred onto a glass substrate. **(b)** PL image of the sample after photoexcitation with 0.8 mJ/cm^2 laser light centred at 775 nm for duration of 16 minutes. The dark square in the middle corresponds to the photoexcited region. **(c)** Difference between images (a) and (b). All scale bars, 20 μm.

Ultrafast photoexcitation leads to a stable localised reduction of the PL intensity. Figure 3.3 **(b)** shows the PL image of the sample after 16 minute exposure to 0.8 mJ/cm^2 laser pulses centred at 775 nm. To minimise fluctuations of the excitation power due to accidental defocusing of the set up, lower numerical aperture 20x air lens was used. The long exposure time was required due to the larger size of the photoexcited region.

As it can be seen from Figure 3.3 **(b)**, the decrease of the PL intensity occurs in both monolayer and bilayer regions of the sample. Figure 3.3 **(c)** is constructed by plotting difference between Figures 3.3 **(a)** and **(b)**: pristine areas appear black as their intensity has not changes. In the modified area, regions with different thicknesses can no longer be distinguished from each other, indicating that the intensity of the PL intensity produced by monolayer and bilayer areas has reduced by exactly the same values.

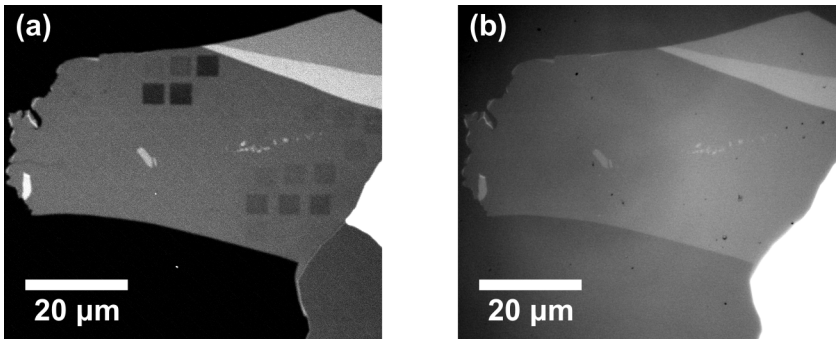

Figure 3.4: **(a)** PL image of a graphene sample on a glass substrate after photomodification showing the decrease of up-converted PL intensity in modified regions. **(b)** Optical micrograph of the same flake after photomodification.

A similar effect could be caused by the optical damaging of graphene. However, optical micrographs of samples after photoexcitation do not show any signs of the photoinduced changes. Figure 3.4 compares PL and optical microscope images of a monolayer graphene flake after photomodification. Even though the contrast of the optical image has been digitally increased, the photomodified regions are indistinguishable from pristine graphene.

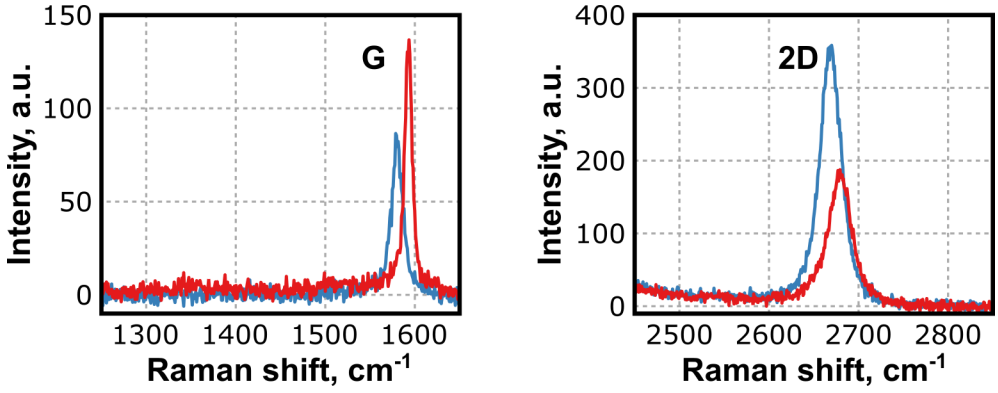

Figure 3.5: Raman spectra of a monolayer graphene sample before **(blue)** and after **(red)** excitation with 3 mJ/cm^2 laser pulses centred at 815 nm for 1 minute.

Furthermore, the Raman spectra collected in the modified regions do not contain the defect-activated D peak. Figure 3.5 shows an example of Raman spectrum before and after photoexcitation: even though the positions and intensities of both G and 2D peaks have changed, the absence of the D peak at 1350 cm^{-1} indicates that no structural defects have been created in graphene [110].

The photoexcited areas are indistinguishable from pristine graphene in optical microscope images and do not contain structural defect. However, they produce significantly different PL signal, indicating that interaction with near-infrared (near-

IR) picosecond laser pulses has led to modification of graphene.

It is worth mentioning that PL imaging can also cause photomodification. Therefore, low pulse fluences and short exposure times must be used to ensure that no unintentional modification of samples occurs.

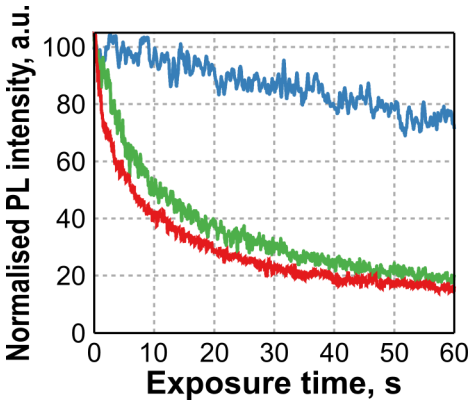

Figure 3.6: Decrease of the normalised PL intensity upon photoexcitation with 0.3 mJ/cm^2 **(blue)**, 0.7 mJ/cm^2 **(green)** and 1.2 mJ/cm^2 **(red)** pulses with the wavelength of 1064 nm.

Figure 3.6 shows the dependence of the PL intensity on the total exposure time for a graphene sample modified with a 1064 nm laser excitation with various pulse fluences. The PL intensity was normalised to the value recorded in pristine sample to make difference between excitation regimes more visible. As it can be seen, the interaction with 0.7 mJ/cm^2 **(green)** and 1.2 mJ/cm^2 **(red)** pulses has led to a significant decrease of the PL intensity. However, the reduction of the PL intensity for 0.3 mJ/cm^2 **(blue)** excitation is much smaller and is caused not by photomodification, but by defocusing of the system during the measurement; the PL image of the sample taken after the measurement does not show any sign of PL intensity reduction in the photoexcited region.

To prevent unintentional photomodification during PL imaging, pulse fluence was kept below 0.3 mJ/cm^2. At the end of each experiment, the PL intensity of non-modified regions was compared to the value recorded in the pristine sample to ensure that no accidental photomodification has occurred.

3.3 Photoluminescence intensity decrease for samples with different thicknesses

In order to investigate modification effects of pulsed laser excitation on samples with different number of layers, few layer graphene samples were fabricated by mechanical exfoliation. To minimise the influence of sample-to-sample variation of graphene properties, flakes containing areas with different thicknesses were used. After a suitable flake had been identified using an optical microscope and its PL image had been created, areas with different number of layers were modified using 814 nm light with pulse fluence of 1 mJ/cm^2. Figure 3.7 compares temporal photomodification dynamics (TPD) for sample thickness up to four layers.

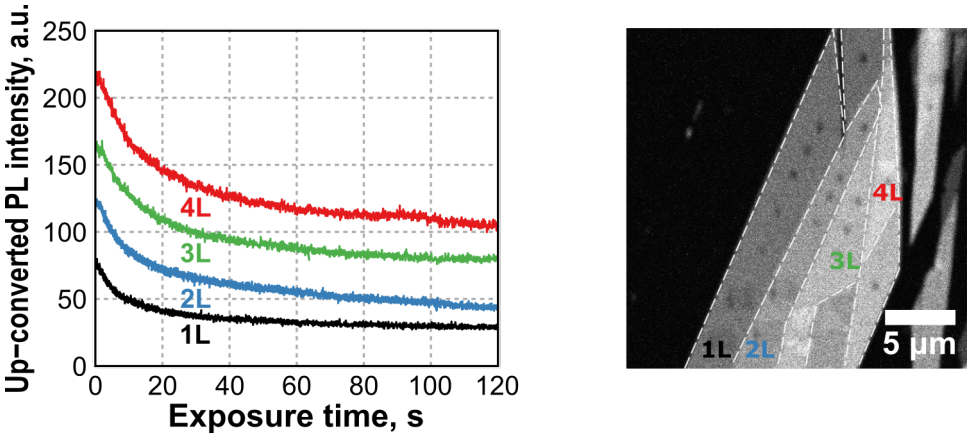

Figure 3.7: **(left)** The decrease of the PL intensity for photomodification with 1 mJ/cm^2 laser light centred at 814 nm for sample thicknesses up to four layers. **(right)** PL image of the sample after photomodification. The numbers in the image indicate the thickness of the corresponding region.

As for few-layer samples PL intensity increases with increasing number of layers, the thicker areas show a higher pristine value of the PL intensity - see Section 1.4 for the details. Upon photoexcitation, all four areas demonstrate identical behaviour: initial rapid drop of the I(PL) is followed by slower decline. Though the shape of the TPD curves is very similar, the total change and rate of the PL intensity reduction is different in different regions. The variation might be caused by changes of experimental conditions (e.g. fluctuation of the laser power or defocusing) or sample inhomogeneity. These effects can be minimised by modifying several areas at the same time and averaging the signal over the region with the same thickness.

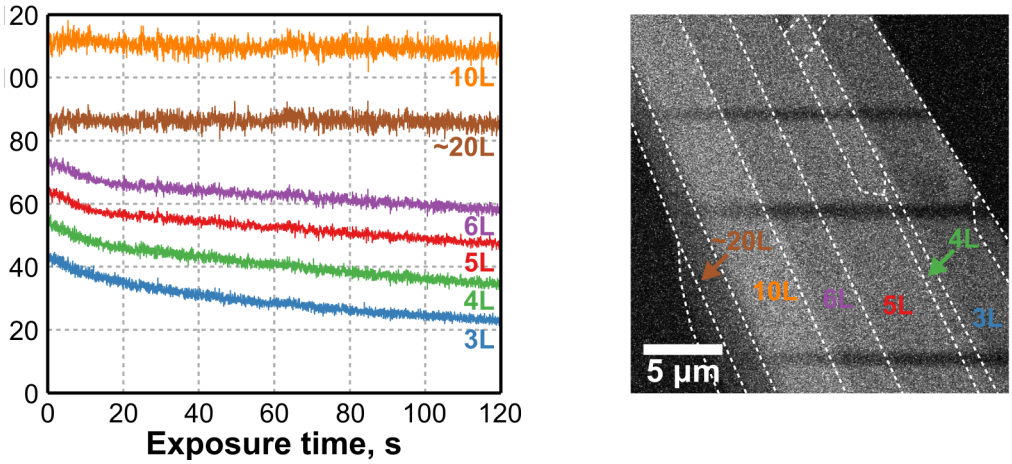

Figure 3.8: **(left)** Temporal photomodification dynamics in areas of a graphene sample with different thicknesses. **(right)** PL image of a few-layer graphene flake after photomodification with 813 nm excitation with the pulse fluence of 3 mJ/cm^2. The numbers in the image indicate the thickness of the corresponding region. The thicker areas appear darker due to non-monotonous dependence of the PL intensity on sample thickness.

Figure 3.8 plots the TPD curves obtained by exposing a straight line across the areas with different thicknesses. The regions up to 6 layers thick demonstrate a virtually identical response to the photoexcitation, with thicker samples showing a slightly slower I(PL) decrease rate. The areas with number of layers $N > 10$, however, show completely different behaviour: the PL signal produced by thick areas remains constant with increasing exposure time.

Very similar rate of the PL intensity decrease in samples with different thicknesses suggests that the process affecting PL intensity occurs primarily at the surface of graphene. Due to its intrinsically high surface-to-volume ratio, graphene exhibits strong environmental sensitivity, and molecules physisorbed onto graphene can significantly alter its electrical and optical properties [142, 144]. In ambient conditions, graphene samples can experience significant p-doping due to interaction with oxygen and moisture in air [88, 144]. Reversible photoinduced doping has been reported previously for visible [95] and ultraviolet [98] excitation and was attributed to the laser heating of graphene and the release of adsorbate groups respectively. However, the linear dependence of the total exposure time required to achieve a certain degree of I(PL) decrease on the size of the photoexcited region and much lower energy of near-IR phonons suggest that photomodification process has different origin.

The absence of I(PL) decrease in thicker samples may be caused by the significant decrease of the surface-to-volume ratio. The thickness-dependent doping caused by physisorption of oxygen onto the basal plane of graphene has been demonstrated before: though single and bilayer samples showed reversible hole doping in the oxygen atmosphere, no change was observed in thicker samples [94]. However, more detailed studies of thickness dependence of the modification process are required to draw any conclusions.

3.4 Photomodification with difference wavelengths

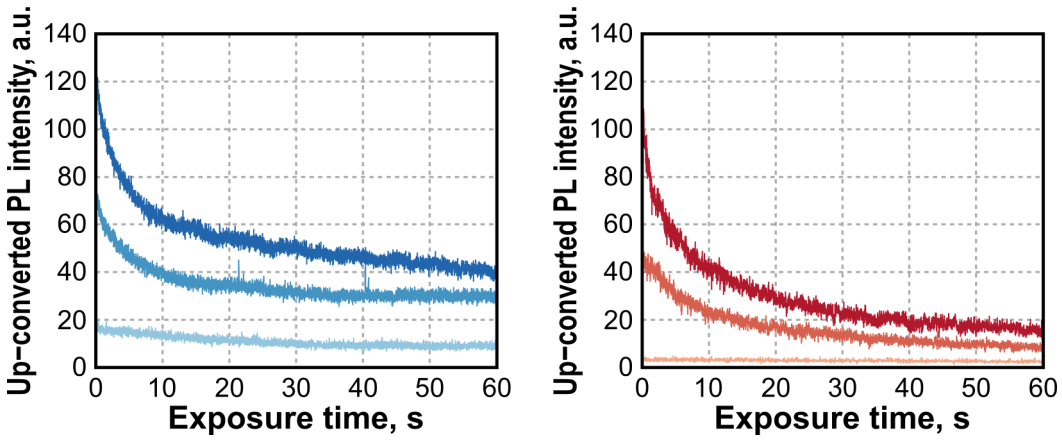

Figure 3.9: **(left)** TPD curves for modification with 775 nm laser pulses with 0.4 (bottom) , 1.1 (middle) and 1.7 (top) mJ/cm^2 pulse fluence. **(right)** TPD curves for modification with 1064 nm excitation with 0.3 (bottom), 0.7 (middle) and 1.2 (top) mJ/cm^2 pulse fluence.

Figure 3.9 shows TPD curves for modification with 775 nm **(left)** and 1064 nm **(right)** pulses recorded using a similar set of excitation powers. Lower PL intensity in the latter case is caused by two reasons. Firstly, for the same excitation power, the absorbed fluence for 1064 nm excitation is lower due to a larger excitation spot size. Secondly, different portions of the up-converted PL spectrum were detected for two excitation frequencies. The spectrum of PL produced with picosecond excitation has a symmetric shape centered at the excitation wavelength [64]. Since a 750 nm short-pass filter was used to isolate the up-converted signal in both experiments, for 1064 nm excitation, a much smaller part of the PL spectrum was detected by PMT[1].

[1]Hamamatsu R3896. Spectral response range:185 to 900 nm

The difference in the PL intensity becomes smaller with increasing excitation power as the higher energy end of the PL spectrum shows a stronger power dependence [71].

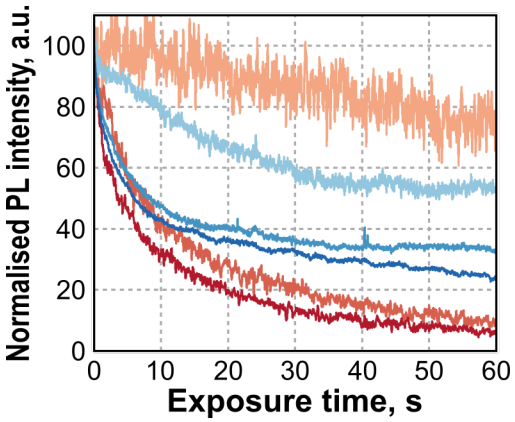

Figure 3.10: Normalised PL intensity decrease for 775 nm **(blue)** and 1064 nm **(red)** excitation with different pulse fluences.

To compare TPD curves for different excitation frequencies and powers, Figure 3.10 plots the PL intensity normalised to its pristine value. For both wavelengths, photoexcitation leads to the modification of graphene with I(PL) decrease curves having very similar shapes. However, for 1064 nm excitation the intensity decrease occurs at a slower rate and saturates at a much lower level.

The absence of a strong dependence on the excitation wavelength suggests that photomodification is not mediated by the absorption of individual photons, but is a consequence of very high electron phonon temperatures achieved with ultrafast pulsed excitation. Different saturation levels for 775 nm and 1064 nm excitations indicate that the higher-energy part of the up-converted PL spectrum is more affected by photomodification. This can be evidence of changes in the relaxation times of hot charge carriers as higher energy electrons would be more affected by it due to a larger phase space available for scattering.

For both excitation frequencies, the TPD curves obtained with higher excitation powers have virtually identical shapes despite almost a factor of two difference in the absorbed laser fluence. This suggests that there is a process that limits the maximum rate of the PL intensity decrease.

3.5 Effects of photomodification on photoluminescence spectrum

The signal registered with the PMT represents the integrated intensity of the up-converted PL. To obtain frequency-resolved information about the effects of the photomodification, the changes of PL spectrum were investigated using the Hamrock SR-303i spectrometer - see Section 2.3.2 for details. Figure 3.11 compares the PL spectra of a monolayer graphene sample before **(blue)** and after **(orange)** the photomodification. The gap in the middle corresponds to the optical filters blocking the excitation light represented by the red spike at 785 nm.

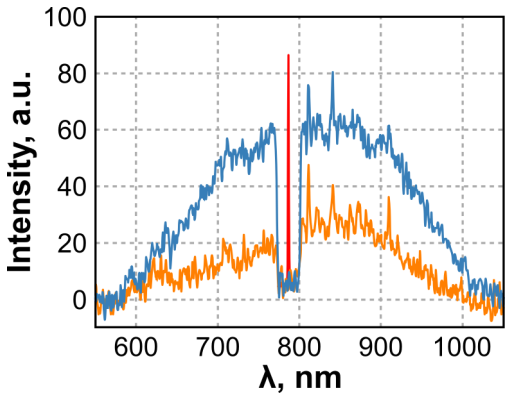

Figure 3.11: The PL spectrum produced by a monolayer graphene sample under excitation with 6 ps laser pulses before **(blue)** and after **(orange)** the photomodification. The gap in the middle of the spectra corresponds to the bandstop filters used to block the 785 nm excitation that is marked by the red line.

The PL signal produced under picosecond excitation peaks at the wavelength of excitation, with up-converted and down-converted parts having a comparable strength. The photomodification affects not only the integrated intensity of PL, but also the emission spectrum. After modification, the intensity of both parts of the PL is decreased; however, the up-converted part of the PL is affected more than down-converted part.

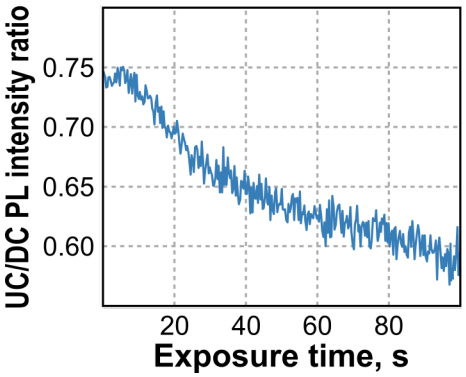

Figure 3.12: The changes of the integrated intensity ratio of the up-converted and down-converted PL under photoexcitation.

The ratio of the integrated intensity of the up-converted and down-converted PL shows a steady decrease with increasing exposure time (Fig. 3.12). This modification-induced asymmetry of the PL spectrum indicates an increase in the energy loss rate of the hot carriers. As the density of electronic states of graphene increases linearly with increasing charge carrier energy, higher energy electrons would be more affected by it, due to a larger phase space available for scattering.

3.6 Effects of pulse duration

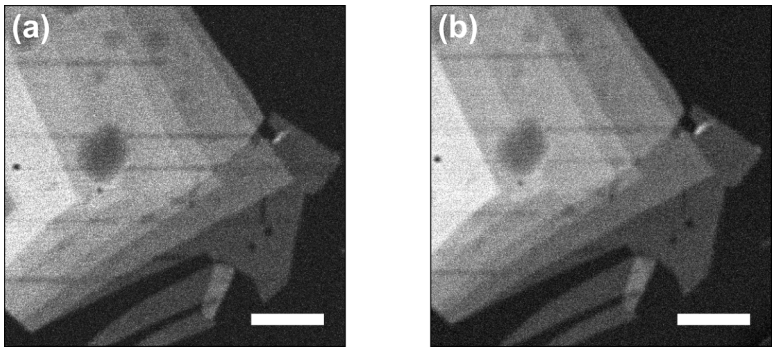

Figure 3.13: **(a)** PL image of a few-layer graphene sample after photomodification created using 6 ps excitation with the wavelength of 775 nm. **(b)** PL of the sample created using 180 fs excitation centred at 765 nm. In both cases, the excitation pulses had the fluence of 0.17 mJ/cm^2. All scale bars, 5 μm.

To investigate the effects of the temporal pulse width on the photomodification process, PL imaging and photomodification were performed using 180 fs laser pulses generated by the Mira 900D laser.

The shape of the PL spectrum changes significantly with excitation pulse width[2], and the variation of the PL spectrum reflects the alteration of the nonequilibrium charge carrier distribution. While for picosecond excitation the carrier distribution created by photoexcitation is significantly broadened by e-e scattering, a much higher instantaneous carrier density achieved with femtosecond excitation results in the electrons being fully thermalised with each other, forming a hot Fermi-Dirac distribution.

The use of excitation pulses with different temporal widths, however, results in virtually identical PL images. Figure 3.13 compares the PL images of a few-layer graphene sample created using excitation pulses with the 6 picosecond **(a)** and 180 femtosecond **(b)** duration.

Though the up-converted PL signal produced with femtosecond excitation had a higher intensity, the brightness of the PL image was adjusted digitally to make the two images more comparable. Various regions modified using picosecond pulses are clearly visible in both images and have a very similar contrast, indicating that photomodification has a similar effect on the intensity of both femtosecond and picosecond PL. The prolonged exposure of the sample to femtosecond radiation also leads to a stable reduction of the PL intensity. However, unlike the photomodification with picosecond pulses, it is caused by optical damage induced in the sample.

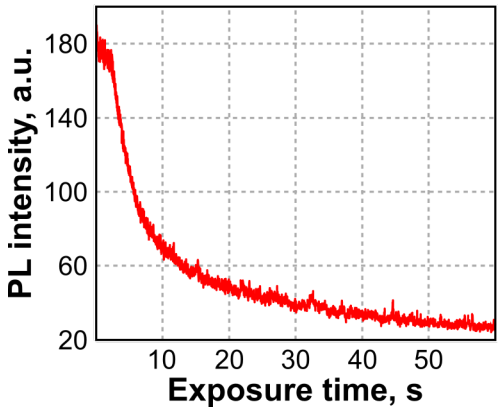

Figure 3.14: The temporal dependence of the PL intensity for photoexcitation with 180 fs pulses centred at 813 nm with the fluence of 1 mJ/cm^2.

The difference between optical damaging and photomodification can be immediately seen in the shape of the PL intensity decrease with increasing exposure time (Fig. 3.14). For femtosecond excitation, the PL intensity shows a slow initial decline followed by a rapid drop. The intensity reduction rate decreases with increasing ex-

[2]See Section 1.4 for details.

posure time, however, it never reaches zero, and the PL intensity continues to decline until the sample produces no detectable signal.

Though the initial slow decrease may result from a process similar to the picosecond photomodification, the dramatic change of the slope indicates the onset of the optical damage. As soon as initial defects, i.e. dislocations or missing atoms, are created, the structural integrity of graphene becomes compromised, making it more susceptible to laser-induced damage [145]. The defects also significantly lower the heat conductivity of graphene, allowing for more efficient localised laser heating [146–148]. These effects lead to an avalanche increase in the rate of creation of new defects, resulting in a rapid drop of the PL intensity. The decrease of PL continues until graphene is transformed into amorphous carbon or oxidised completely.

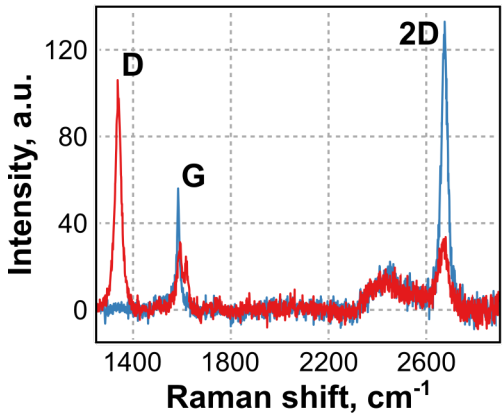

Figure 3.15: Raman spectra of a monolayer graphene sample before **(blue)** and after **(red)** 2 minutes excitation with 180 fs pulses with 1 mJ/cm^2 fluence centred at 813 nm.

Figure 3.15 compares the Raman spectra collected before **(blue)** and after **(red)** the two minute exposure to 1 mJ/cm^2 femtosecond laser pulses. The considerable intensity decrease and broadening of the 2D peak, as well as high intensity ratio of the D and G peaks in the Raman spectrum after the excitation, indicates significant photoinduced damage [109].

The difference between the two excitation regimes lies in the relative pulse duration compared to characteristic relaxation time scales in graphene. The duration of the femtosecond pulse is shorter than the characteristic electron-phonon thermalisation time [50, 62, 63], leading to a significant increase in the electron temperature after the excitation. On the other hand, the temporal width of the picosecond pulses is comparable with the lattice cooling time [52, 54, 62]. Though the maximum phonon temperatures achieved with picosecond excitation are significantly lower, the graphene lattice remains at an elevated temperature for a longer time.

The photoexcitation with the femtosecond pulses on some occasions has led to a PL intensity reduction very similar to the one observed for picosecond photomodification. However, the femtosecond photomodification was found to be sample-specific and very difficult to control. The majority of the samples demonstrated an increasing D peak intensity in the Raman spectrum recorded after femtosecond excitation.

3.7 Environmental dependence of photomodification

To investigate environmental sensitivity of the photomodification process, the ambient atmosphere was replaced with high-purity argon gas using a specially designed sample holder - see Fig. 3.16 for the schematics. Prior to modification in the argon atmosphere, a reference data set was created by exposing several areas of a four layer graphene flake to 813 nm laser light with 1 mJ/cm^2 fluence in ambient conditions. The sample chamber was then flushed with fresh argon for a duration of 10 minutes and photomodification was performed on pristine areas of the same flake using identical excitation conditions.

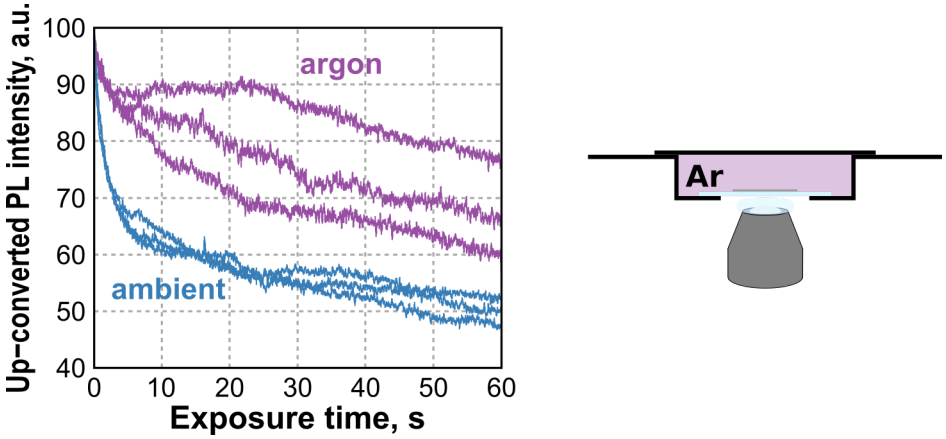

Figure 3.16: **(left)** TPD for modification in ambient **(blue)** and argon **(magenta)** atmospheres. **(right)** Schematics of the sample holder used to study environmental sensitivity of photomodification.

Figure 3.16 plots the decrease of PL intensity recorded during modification in ambient **(blue)** and argon **(magenta)** atmospheres. The pristine value of PL intensity is identical in both cases, however, the inert atmosphere has significantly lowered the rate of the I(PL) decrease. The observed environmental sensitivity suggests that photomodification is mediated by adsorption of atmospheric gas molecules to the surface of graphene.

Though the inert atmosphere has significantly lowered the rate of I(PL) decrease, it has not prevented photomodification completely. This may indicate that the molecular or atomic species that take part in the modification process were already present at the surface of graphene. However, significant variations in the shape of the TPD curves for modification in the argon atmosphere suggest the leakage of atmospheric gases into the sample chamber as a more probable explanation. A more detailed study is required to identify the roles of different gases in the photomodification process, including the modification in controlled gas environments and under high vacuum. However, these measurements require the use of a vacuum chamber which could not be implemented in the current experimental set-up.

3.8 Stability of photomodification effects

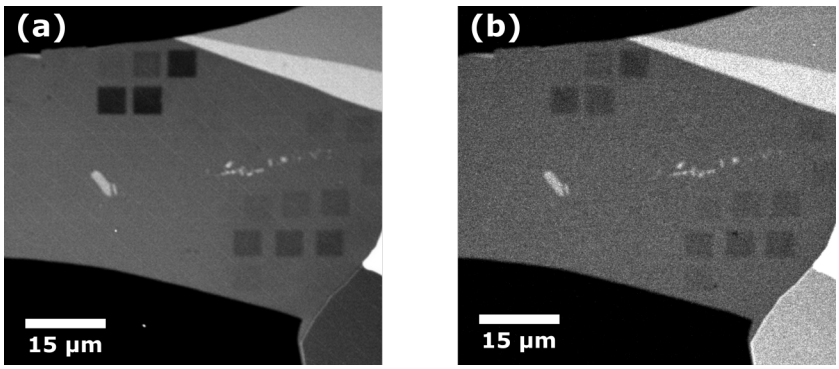

Figure 3.17: PL image of a graphene sample on a glass substrate taken immediately after photomodification **(a)** and after a period of six months **(b)**.

The photoinduced reduction of the PL intensity demonstrates a remarkable long-term stability. Figure 3.17 compares the PL image of graphene sample recorded shortly after photomodification **(a)** and after a six month period **(b)** during which the sample was kept at room temperature and in ambient atmosphere. Although the two images cannot be compared directly due to the difference in PL imaging conditions (i.e. excitation power and wavelength, optical filters, and PMT voltage), all modified regions are clearly visible in Figure 3.17 **(b)** and their relative contrast has remained unchanged.

Despite the stability in ambient conditions, modification effects can be reversed completely by immersing sample into solvent, such as methanol or isopropyl alcohol (IPA). Figure 3.18 **(a)** shows the PL image of a pristine few-layer sample on a glass substrate; the darker part in the middle corresponds to a monolayer area. Prior to immersion into a solvent, a rectangular region of the flake including areas of

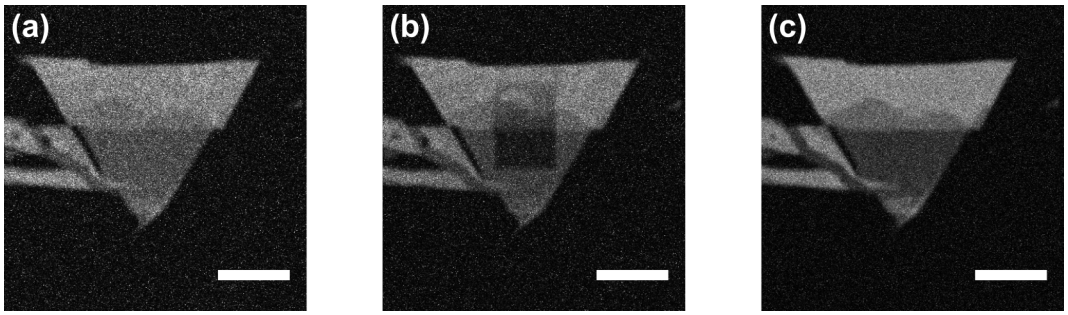

Figure 3.18: **(a)** PL image of a few layer graphene sample. The darker part in the middle corresponds to the monolayer area, while brighter regions at the top are two and three layers thick. **(b)** PL of the sample after photoexcitation with 815 nm light with fluence of 3 mJ/cm^2 for two minutes. **(c)** PL of the flake after solvent treatment showing complete recovery of the PL intensity in all regions. All scale bars, 5μm.

mono-, bi- and trilayer graphene was exposed to 3 mJ/cm^2 laser pulses centred at 815 nm for 2 minutes. The image of the sample after photomodification shows a strong reduction of the PL intensity in all the regions (Fig. 3.18 **(b)**). The sample was then immersed into methanol for one hour, washed with IPA and dried using a nitrogen flow. As it can be seen from Figure 3.18 **(c)**, this treatment resulted in the complete recovery of the PL intensity.

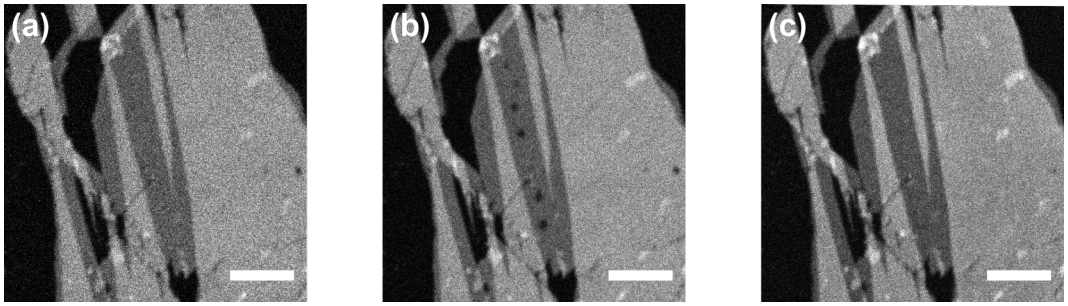

Figure 3.19: **(a)** PL image of a graphene flake before photomodification. The darker region in the middle corresponds to a monolayer area. **(b)** a PL image of the sample after photomodification showing photoinduced decrease of the PL intensity in several circular regions. **(c)** a PL image of the sample after thermal annealing in ambient atmosphere at 200° C for duration of 10 minutes. All scale bars, 5μm.

A very similar result can be achieved by annealing of the sample in an ambient atmosphere. Figure 3.19 shows PL images of a graphene sample before **(a)** and after **(b)** photomodification; the small dark circles in the PL images correspond to regions modified with various excitation powers. Following the photomodification, the sample was placed onto a hot plate and heated up to 200° C for 10 minutes. As evident from Figure 3.19 **(c)**, after annealing the PL intensity of the modified

regions has recovered to pristine values while the intensity of non-modified regions has remained unchanged.

The complete recovery of the PL intensity gives an additional proof that modification process does not involve damaging of the graphene. If photomodification originated from steady-state heating of the sample due to the interaction with laser pulses, sample annealing in ambient atmosphere would also lead to the reduction of the PL intensity. However, the thermal treatment does not affect PL intensity in pristine areas and completely reverses the I(PL) decrease in photomodified regions.

Moreover, no PL intensity recovery has been observed for low power excitation, suggesting that photoexcitation does not cause significant heating of the sample. The difference between two processes may lie in a very localised nature of heating or much higher instantaneous temperatures achieved with pulsed photoexcitation.

3.9 Summary

In summary, the modification of graphene caused by the interaction with near-infrared picosecond laser pulses was investigated using PL imaging. Though no optical damage was inflicted on graphene, the interaction with short intense pulses has led to a localised decrease of the PL intensity. The photoinduced changes show remarkable long-term stability, with very little change observed in the modified sample after 6 months.

Photoexcitation with different wavelengths leads to a very similar decrease of the PL intensity suggesting that the modification process is not a result of single- or multiphoton absorption, but arises from extremely high instantaneous temperatures reached with ultrashort pulsed excitation. The recovery of the PL intensity in the modified regions after thermal annealing indicates that photomodification is not caused by the steady-state heating of the sample, but is a result of a highly nonlinear regime achieved with ultrafast excitation. Strong environmental sensitivity implies that modification process is mediated by physisorption of atmospheric gas molecules onto the surface of graphene, most likely ambient oxygen and moisture.

The photomodification of graphene occurs for excitation fluences significantly lower than optical damage threshold and may not be immediately obvious, as the changes induced in graphene are not visible in optical microscope images and, though they cause substantial changes in the Raman spectrum, they do not lead to the activation of the D peak.

Chapter 4

Photoinduced doping and strain in exfoliated graphene

4.1 Introduction

In this chapter, changes of graphene properties induced with photomodification are studied using Raman spectroscopy. Stable photoinduced reduction of the ultrafast PL intensity shows that, even for relatively low pulse fluences, interaction with laser light can significantly alter the properties of graphene. As pulsed laser excitation is used in a wide variety of measurements, it is of a great importance to understand how sample properties are affected by photoexcitation. The changes of the sample properties during measurements may be responsible for discrepancies that are sometimes observed in the data.

Changes of the graphene properties caused by photomodification were studied using spatially-resolved Raman spectroscopy. Variation of the Raman spectra after modification show that photoexcitation has led to an increase in the doping level of graphene as well as changes in the level of mechanical strain. Atomic force microscopy studies of the samples show an increase of the surface roughness in the modified regions, suggesting that changes in the strain level are caused by slippage and buckling of graphene, the effect similar to the one observed in the anneal samples [88, 90]. The increase in the doping level is likely to be caused by the enhanced bonding of atmospheric oxygen due to the distortion of the graphene surface. Strong correlation between the PL intensity decrease and the area ratio of the Raman 2D and G peaks suggests that the former is caused by an increased inelastic scattering rate of hot charge carriers.

4.2 Raman studies of photoinduced changes in exfoliated graphene

To investigate the modification of graphene properties caused by interaction with laser pulses, square regions of monolayer flakes were exposed to different fluences of picosecond excitation for a duration of 1 minute and the changes induced in graphene were monitored using Raman spectroscopy. Single layer graphene samples were prepared by mechanical exfoliation of natural graphite and deposited on $180 - \mu m$-thick glass substrates - see Section 2.2.1 for the details. The number of layers in individual samples was estimated by optical contrast measurements [104] and confirmed using Raman spectroscopy [143]. Excitation pulses centred at 816 nm generated by Levante OPO were focused onto the sample using a 60x water immersion lens. Square regions were modified by raster-scanning the laser spot across the chosen area of the sample and the total exposure time was controlled by changing the number of raster-scans.

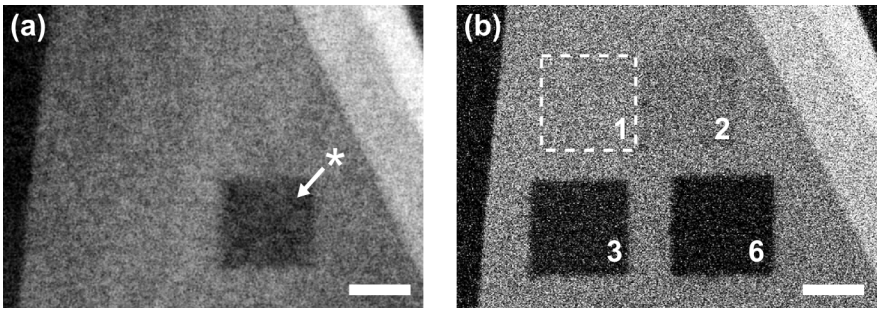

Figure 4.1: **(a)** Optical micrograph of a monolayer graphene flake after photomodification. The asterisk denotes the area where pump fluence was high enough to cause material ablation. **(b)** PL image of the sample showing a decrease of upconverted PL intensity in the modified regions. The numbers indicate excitation fluence in mJ/cm^2 that was used to modify the corresponding region. The dashed line indicates the first excited region. All scale bars, 3 μm.

Figure 4.1 **(a)** shows the optical micrograph of a single layer graphene flake after photomodification. Even though the contrast of the image has been digitally increased, there are no visible signs of modification except for the bottom right square where the excitation power was high enough to cause laser ablation. The photoexcited regions, however, are clearly visibly in the PL image (Fig. 4.1 **(b)**) due to photoinduced reduction of the PL intensity; the numbers in the image indicate the excitation fluence that was used to modify the corresponding region.

Figure 4.2 compares the Raman spectra collected in the centre of the first square region before **(dashed blue)** and after **(solid red)** excitation with 1 mJ/cm^2 laser

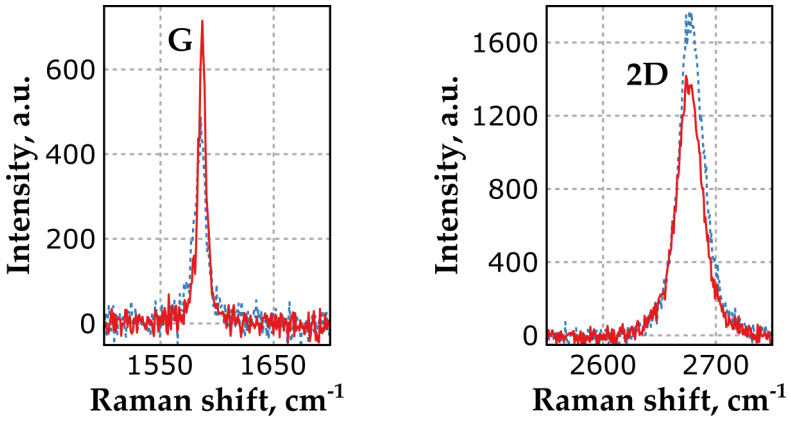

Figure 4.2: Raman spectra corresponding to the centre of the first square region before **(dashed blue)** and after **(solid red)** photoexcitation with 1 mJ/cm^2 laser pulses for 1 minute.

pulses for 1 minute. Upon photoexcitation, the G peak is up-shifted by 1.2 cm^{-1} and the 2D peak is down-shifted by 1.6 cm^{-1}, and the intensity ratio of two peaks I_{2D}/I_G is decreased. Note that no defect-induced D peak has been observed at 1350 cm^{-1} in the spectra after excitation, indicating that photomodification has not induced any structural defects in graphene.

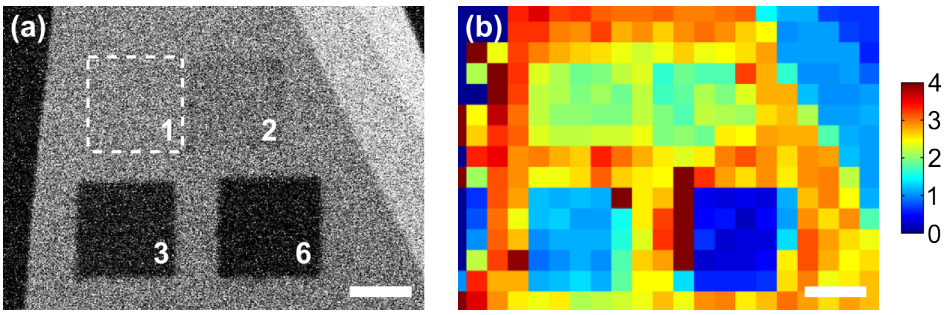

Figure 4.3: **(a)** PL image of the graphene sample after photomodification. **(b)** Raman map of the sample plotting intensity ratio of the 2D and G peaks. All scale bars, 3 μm.

The modified regions are clearly visible in the Raman map plotting intensity ratio of the Raman 2D and G peaks (Fig. 4.3 (b)) as photomodification has led to a decrease of the I_{2D}/I_G ratio. Higher excitation power gives rise to a stronger decrease of the intensity ratio. The localisation of the photoinduced changes visible in the Raman map match perfectly with the dark regions observed in the PL images, indicating that the modification is local, limited to the region of photoexcitation.

A reduced I_{2D}/I_G ratio and sharpening of the G peak in the modified regions suggests that photoexcitation has led to an increase of the doping level [119]. How-

ever, the observed peak position changes do not match the ones expected from the estimated value of the chemical potential, suggesting that there also has been a change in the level of mechanical strain.

4.3 Separation of contributions from doping and strain to the peak position change

Changes of the Raman 2D and G peak positions can be caused by the variation of both doping and strain, and this bimodal sensitivity complicates data analysis [111, 119, 149]. However, the contributions from strain and doping can be separated by considering the correlation between the frequency shift of the 2D and G peaks. This method first was introduced by J. Lee et al. [90]. It is based on the fact that the relative rate of the peak position change is very different for the cases of doping and strain.

Variation of the peak positions under applied strain is caused by the shift of the phonon frequencies due to the change of the interatomic distances. While the rate of the peak position change depends on the type and direction of strain, the 2D peak always experiences larger shift because it originated from the second-order process involving two phonons [105, 108].

Uniaxial strain lowers the crystal lattice symmetry, causing both G and 2D peak to split into two components[1] [111]. The relative rate of the peak position change under applied stress depends on the direction of strain with respect to the crystallographic axes of graphene. For the zigzag-oriented strain, $\Delta\omega_{2D}^{+}/\Delta\omega_{G}^{+} = 2.00$ and $\Delta\omega_{2D}^{-}/\Delta\omega_{G}^{-} = 2.05$ while for the strain along the arm-chair direction $\Delta\omega_{2D}^{+}/\Delta\omega_{G}^{+} = 3.00$ and $\Delta\omega_{2D}^{-}/\Delta\omega_{G}^{-} = 1.89$ [118]. When the level of strain is insufficient to resolve the two peak components, $\Delta\omega_{2D}/\Delta\omega_{G}$ can be approximated as 2.02 (2.44) for the zigzag (arm-chair) direction.

Biaxial strain preserves the lattice symmetry and does not cause peak splitting, with the experimentally measured values of $\Delta\omega_{2D}/\Delta\omega_{G}$ ranging from 2.45 to 2.80 [115–117].

Variation of the peak position with varying ϵ_F is caused by the change of the equilibrium lattice parameter [119] and the presence of Kohn anomalies in graphene [120, 150]. As the latter has negligible influence on the 2D peak, ω_{2D} shows weaker dependence on the carrier concentration. Figure 4.4 plots the correlation in peak position changes between the 2D and G peaks with varying carrier density for elec-

[1] See Section 1.3.2.4 for more details.

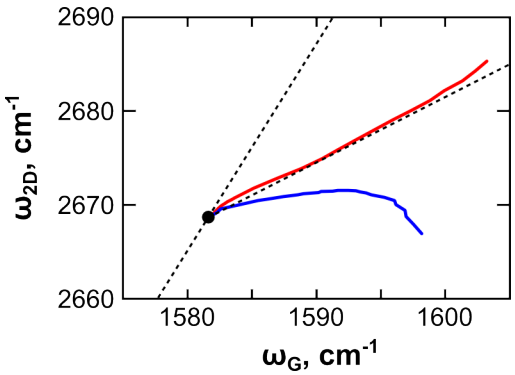

Figure 4.4: Variation of the Raman 2D and G peak positions with increasing electron **(blue)** and hole **(red)** doping. Black dot corresponds to $(\omega_G;\omega_{2D})$ position in undoped sample. Image adapted from Ref. [90].

tron **(blue)** and hole **(red)** doping. The frequency vector $(\omega_G;\omega_{2D})$ in the case of hole doping shows approximately linear dependence on the carrier concentration with the slope $\Delta\omega_{2D}/\Delta\omega_G = 0.7$ [90]. For electron doping, however, $\Delta\omega_{2D}/\Delta\omega_G$ quickly becomes nonlinear with increasing carrier concentration.

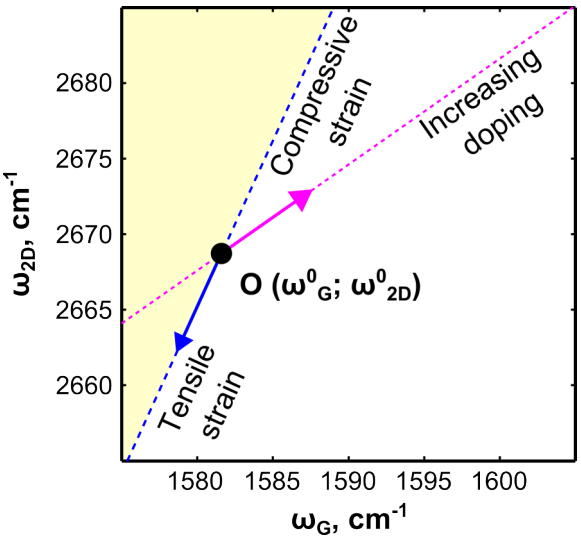

Figure 4.5: Unit vectors for strain- **(blue)** and doping-induced **(magenta)** changes of the $(\omega_G;\omega_{2D})$ position. Black dot corresponds to the $(\omega_G;\omega_{2D})$ not affected by strain or doping.

The majority of graphene sample in ambient atmosphere experience hole doping due to the interaction with oxygen and moisture in air [88, 94, 144, 151]. Assuming that native stress in the samples is dominated by uniaxial strain of a random direction, the contribution of hole doping and strain to the changes of $(\omega_G;\omega_{2D})$ can be easily separated using a vector decomposition illustrated in Figure 4.5.

The magenta and blue arrows represent the unit vectors for doping- and strain-

induced movement of $(\omega_G;\omega_{2D})$. The former has a gradient of 0.7 while the latter has a gradient of 2.2, an average of $\Delta\omega_{2D}/\Delta\omega_G$ for zigzag and armchair directions. The black dot represents the origin of the vector space, i.e. the $(\omega_G;\omega_{2D})$ position not affected by either doping or strain. Up-shift (down-shift) from the origin along strain direction corresponds to increasing compressive (tensile) strain. The yellow shaded area in the Fig. 4.5 denotes the forbidden region: since increasing doping of any kind leads to a blue-shift of the G peak, $(\omega_G;\omega_{2D})$ can enter this region only for low carrier concentration ($n < 1.4 \cdot 10^{12}$) when $\Delta\omega_{2D}/\Delta\omega_G$ becomes nonlinear [90].

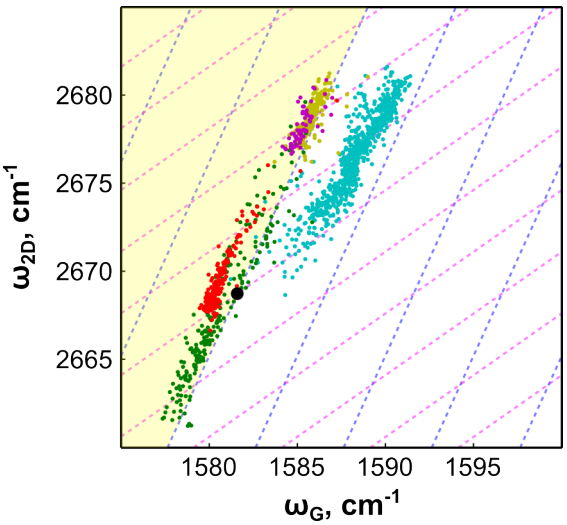

Figure 4.6: Correlation between the 2D and G peak frequencies in pristine graphene samples. The blue and magenta dashed lines indicate directions of strain- and doping-induced shifts of $(\omega_G;\omega_{2D})$. The different colors of the data markers correspond to different samples.

Figure 4.6 plots $(\omega_G;\omega_{2D})$ obtained by Raman mapping five pristine graphene samples. The intrinsic frequencies of the 2D and G modes $(\omega_G^0;\omega_{2D}^0)$ were calculated using the results from Ref. [83] and taking into account changes of the 2D peak position due to the difference in the excitation wavelength [105]. All samples show a significant variation of the peak positions across the sample. However, in all cases $(\omega_G;\omega_{2D})$ is primarily distributed along the lines with a gradient of 2.2, which is in excellent agreement with the behaviour expected for the case of randomly oriented uniaxial strain. For the majority of the samples, $(\omega_G;\omega_{2D})$ lies in the forbidden region indicating a low intrinsic level of doping.

Interestingly, most of the samples show a native compressive strain ($(\omega_G;\omega_{2D})$ is shifted upwards from the origin along the strain line) with only one sample demonstrating an intrinsic tensile strain. The compressive strain in the majority of the samples was most likely induced during fabrication as exfoliated graphene flake

were deposited onto pre-heated substrate (see Chapter 2 for details). Compression of graphene due to a mismatch in thermal expansion coefficient between graphene and the underlying substrate has been demonstrated before in samples after thermal annealing [152–154]. The only sample demonstrating native tensile strain (denoted with green circles in Figure 4.6) was deposited onto a substrate at room temperature.

4.4 Photoinduced strain and doping in exfoliated samples

The impact of sample-to-sample variation of graphene properties can be minimised by performing photomodification on different areas of the same flake. Nevertheless, it is important to take into account the $(\omega_G;\omega_{2D})$ position in different regions of the sample prior to photoexcitation. Figure 4.7 plots $(\omega_G;\omega_{2D})$ in three square regions of the sample before and after photomodification. Green circle markers denoted the $(\omega_G;\omega_{2D})$ position in the pristine sample. They form a narrow group with broadening primarily induced by variation of strain.

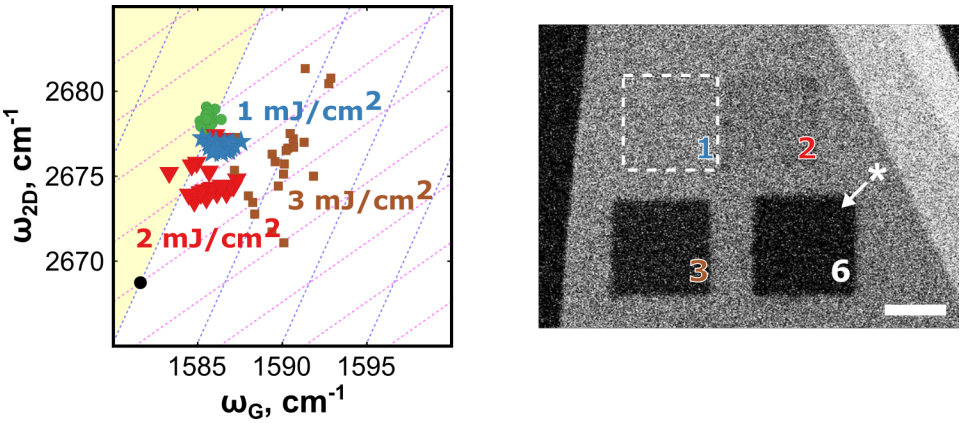

Figure 4.7: **(left)** Plot of $(\omega_G;\omega_{2D})$ after photomodification with 1 mJ/cm^2 **(blue stars)**, 2 mJ/cm^2 **(red triangles)**, and 3 mJ/cm^2 **(brown squares)** for 1 minute. The $(\omega_G;\omega_{2D})$ position in the sample before photoexcitation is shown by green circles. The dashed lines indicate directions of strain- and doping-induced movement of $(\omega_G;\omega_{2D})$. **(right)** PL image of the sample after photomodification. The numbers indicate excitation fluence in mJ/cm^2 that was used to modify the corresponding region. The asterisk denotes the laser-ablated area.

The distribution changes dramatically after photomodification. For the square region modified with 1 mJ/cm^2 laser light **(blue stars)**, the centre of distribution is shifted downward and to the right hand side. To achieve this kind of movement, $(\omega_G;\omega_{2D})$ should be up-shifted along the doping direction and down-shifted along

the strain direction. The former indicates an increase in the local doping level, while the latter demonstrates that photoexcitation has lead to a reduction of compressive strain in graphene, a remarkable effect that has not been reported before.

From Fig. 4.7 it can be seen that photoexcitation leads to significant broadening of the $(\omega_G; \omega_{2D})$ distribution, which for 1 mJ/cm^2 and 2 mJ/cm^2 excitation is mostly caused by variation of doping, and for 3 mJ/cm^2 it is predominantly strain-induced.

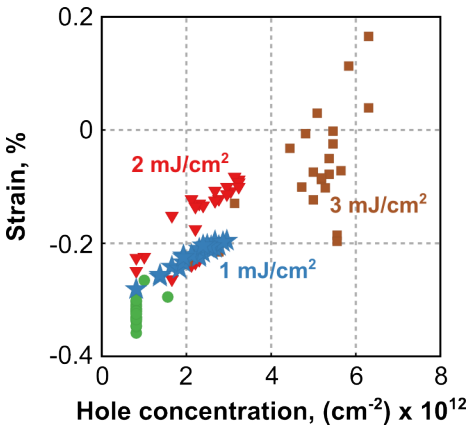

Figure 4.8: Changes of doping and strain level in the sample after photomodification estimated from the variation of the Raman peak positions.

A more quantitative description of the changes induced in the graphene sample by photomodification can be obtained by separating strain and doping contribution to the variation of the G peak position and calculating carrier concentration and strain levels corresponding to the observed G peak shifts. Figure 4.8 plots changes in the carrier density and stress levels after photoexcitation obtained using the data from Refs. [119] and [149]. Note that for the hole concentrations $n < 1.4 \cdot 10^{12}$ the linear approximation for doping-induced changes of $(\omega_G; \omega_{2D})$ is no longer valid, making vector decomposition and data fitting ambiguous. From Figure 4.8, it can be seen that photomodification leads to both an increase in the level of p-doping and a reduction of compressive strain. Higher laser fluences cause larger changes of doping and strain levels.

4.5 Atomic force microscopy studies of photomodified regions

To investigate the origin of photoinduced strain and doping, atomic force microscopy (AFM) scans of a sample after photomodification were performed. Figure 4.9 compares the PL image of a monolayer graphene sample after photomodification with the AFM scan of the sample. For this photomodification experiment, excitation fluence was kept at the same level and different degrees of modification were achieved by varying the total exposure time. Square regions were modified using 1 mJ/cm^2 pulses centred at 815 nm, with a total exposure time varying from 2 to 8 minutes.

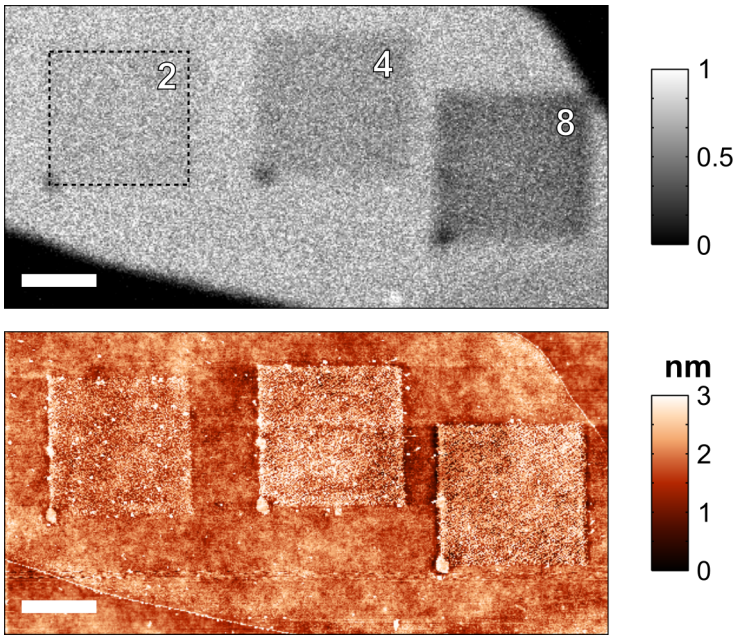

Figure 4.9: **(a)** PL image of a monolayer flake modified with 815 nm excitation with the pulse fluence of 1 mJ/cm^2. Numbers indicate total exposure time in minutes of the corresponding region. **(b)** Height map of the sample created using AFM in dynamic (tapping) mode. All scale bars, 2.5 μm.

The photomodified regions are clearly visible in the topological map of the sample (Fig. 4.9 **(b)**) as they show an increased surface roughness compared to pristine graphene. The modified areas have very sharp borders, indicating the highly localised nature of the photoinduced changes.

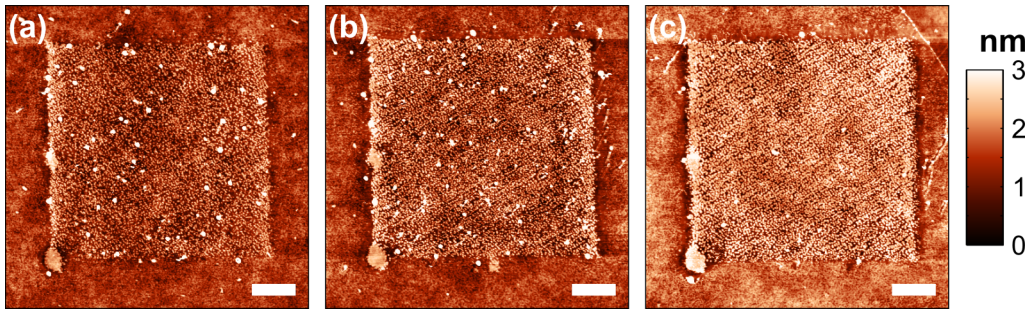

Figure 4.10: Height maps of the regions exposed to 1 mJ/cm^2 laser light centred at 815 nm for 2 **(a)**, 4 **(b)** and 8 **(c)** minutes. All scale bars, 1 μm.

Figure 4.10 compares enlarged images of the three modified regions arranged according to decreasing PL intensity. As it can be seen, the surface roughness shows a very strong correlation with the reduction of the PL intensity. Distortion of the graphene surface is likely to be caused by slippage and buckling of the flake due to the mismatch in thermal expansion coefficients between graphene and the underlying substrate. The increase in the doping level, meanwhile, can be explained by the enhanced bonding of atmospheric oxygen due to the distortion of the graphene surface [88]. These effects are similar to the compressive strain and reversible p-doping induced in graphene upon annealing [88, 90]. The different result, i.e. the reduction of compressive strain in the modified regions, may be a consequence of very local nature of heating or extremely high electron and phonon temperatures reached during pulsed laser excitation.

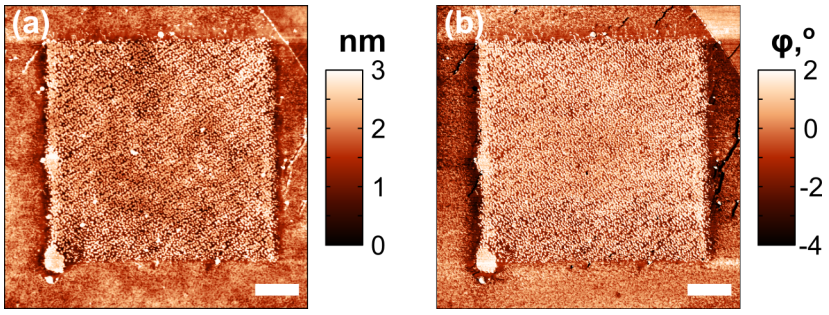

Figure 4.11: **(a)** Height map of the square region after 9 minutes exposure. **(b)** Phase map of the region. All scale bars, 1 μm.

The release of compressive strain has been observed previously in epitaxial graphene samples exposed to atomic oxygen [155]. However, in order to act as a strain-release centre, an oxygen adatom has to be chemically bonded to graphene. The absence of the defect-induced peak in the Raman spectrum indicates that no change of hybridisation occurs during photomodification.

Molecules adsorbed at the surface of graphene should be visible in the phase images constructed by recording the phase difference between the driving signal and cantilever oscillations. Phase imaging provides information about various surface properties, such as adhesion, elasticity, and friction, and it is widely used to distinguish different component of composite materials [156–159].

Figure 4.11 compares height and phase images of a region modified with the total exposure time of 8 minutes. Variation of the phase visible in the modified region may be caused by material contrast due to the molecules physisorbed onto the surface of graphene. However, phase lag can be also caused by difference in the slope of the surface: the difference in phase reflects the dissipation of energy involved in the contact between the sample and the AFM tip, which depends on the total area of contact [160]. Unambiguous determination of material composition is therefore possible only for relatively flat samples [135].

4.6 Correlation between photoinduced strain and doping and decrease of PL intensity

As both doping and strain in graphene samples are affected by photomodification, more detailed study is required to identify the process that leads to the stable decrease of the PL intensity. Figure 4.12 displays the correlation between values of strain and doping extracted from the Raman peak shifts and normalised PL intensity for five different samples after photoexcitation. Note that for some samples various degrees of modification were achieved using identical exposure time and different excitation powers, while for others excitation power was kept at the same level and different exposure times were used.

The majority of the samples demonstrate very similar behaviour, with decreasing PL intensity being correlated with increasing doping and decreasing compressive/increasing tensile strain. However, changes of the sample properties are not always monotonic, and the magnitude of the changes varies from sample to sample.

The observed discrepancies may be caused by several reasons. Firstly, significant variation of strain in pristine samples makes it difficult to compare directly the changes induced in different regions. More accurate analysis that takes into account the initial state of the sample is required, as magnitude and sign of the photoinduced changes might depend on the starting doping and strain in the sample. Secondly, the correlation analysis is limited to the case of hole doping and uniaxial strain, and the presence of electron doping or biaxial strain would make it inapplicable.

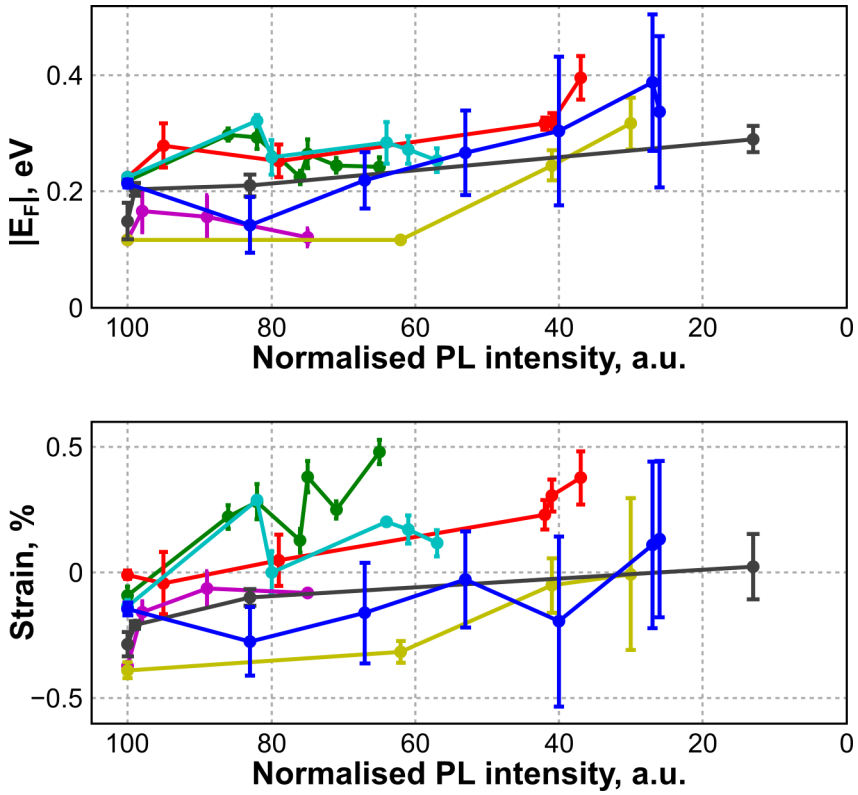

Figure 4.12: Correlation between normalised PL intensity and photoinduced doping **(top)** and strain **(bottom)** in photomodified graphene samples. The different colors of the data markers correspond to different samples.

Any additional process that affects the PL intensity, such as optical damaging of graphene, will further complicate data analysis.

Remarkably, despite the variations in extracted values of strain and doing, correlation between the normalised PL intensity and the area ratio of the Raman 2D and G peak is very similar in all five samples (Fig. 4.13). The A_{2D}/A_G ratio is commonly used to determine carrier concentration in graphene as it is very sensitive to the inelastic scattering rate of electrons [106, 108].

The integrated area of the Raman peak represents the total probability of the corresponding scattering process. As the G peak originates from the first-order scattering process determined by virtual states at the half of the laser energy E_L, it is not affected by doping for $\epsilon_F < E_L/2$. Therefore, although the intensity of the G peak increases and FWHM(G) decreases with increasing doping, the total peak area remains constant [106]. Consequently, the changes in A_{2D}/A_G reflect the variation of the 2D peak area.

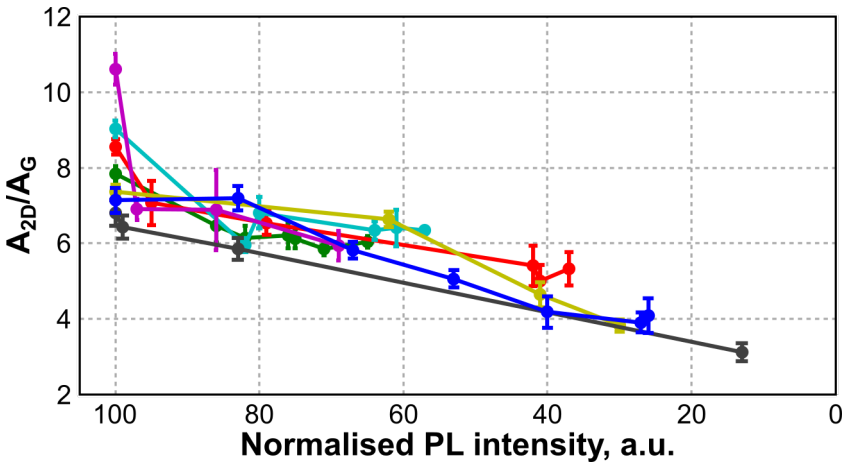

Figure 4.13: Correlation between the normalised PL intensity and the area ratio of the Raman 2D and G peaks in modified samples.

The 2D peak arises from the two-phonon scattering process in which real electronic states act as intermediate states. The 2D peak area therefore shows strong dependence on the inelastic scattering rate of electrons γ, with $A_{2D} \sim 1/\gamma^2$. The two main mechanisms of inelastic scattering in graphene are emission of optical phonons and electron-electron interaction. While the former is only weakly affected by changes in the carrier concentration, the rate of the e-e scattering increases linearly with increasing chemical potential [106, 108].

As changes of the other Raman spectrum parameters are consistent with the picture of photoinduced doping, variation of the inelastic scattering rate due to increasing carrier concentration is the most probable explanation for the observed A_{2D}/A_G dynamics. However, additional sources of inelastic scattering (impurity scattering etc.) or changes in the optical phonon generation rates would also lead to the decrease of the 2D peak area.

4.7 Summary

In summary, the modification of single layer graphene due to intense, picosecond near-infrared laser pulses was investigated using Raman spectroscopy. Ultrafast pulsed excitation leads to both a local increase of p-doping and a change in the level of mechanical strain. While the magnitudes of changes induced by photomodification vary from sample to sample, the sign of the changes is predominantly the same, resulting in an increase in hole doping and stress in the sample changing from compressive to increasing tensile strain.

The increase surface roughness observed in the modified regions suggests that the changes of strain can be caused by the slippage and buckling of graphene while an increase in the doping level can be explained by enhanced binding of atmospheric oxygen and moisture. The latter is in the perfect in agreement with environmental sensitivity of the photomodification described in the previous chapter. A strong correlation between the normalised PL intensity and the A_{2D}/A_G ratio suggests that the reduction of the PL intensity is caused by an increase of inelastic relaxation rate due to photoinduced doping.

The local nature of the photomodification effects can be utilised to create complex patterns that define device functionality, offering an advantage in spatial resolution and speed.

Chapter 5

Ultrafast photoluminescence and charge carrier concentration in graphene

5.1 Introduction

In this chapter, the dependence of up-converted PL intensity on the intrinsic charge carrier concentration in graphene is investigated for the first time. As the ultrafast PL signal arises from recombination of the nonequilibrium carrier distribution created by short pulsed excitation, it is very sensitive to electron relaxation dynamics. The presence of intrinsic charge carriers in graphene can lead to a modification of the inelastic scattering rates of the photoexcited electrons.

The studies of the photoinduced changes of the graphene properties show that the decrease of the PL intensity after photomodification is linked with both an increase in the doping level and a change in the mechanical strain level. However, with both properties changing at the same time, it is difficult to separate their contributions and identify the process that leads to the variation of luminescence intensity.

Graphene-based field-effect transistors were used to control the carrier density in the samples. The dependence of the up-converted PL intensity on the Fermi level position was investigated using a combination of optical and transport measurements. The PL intensity has the maximum value when the Fermi level is positioned at the Dirac point, and decreases with increasing carrier density. For low levels of doping, the PL intensity is only weakly dependent on the charge carrier concentration; however, the dependence becomes much stronger with increasing doping level. The obtained results are in good agreement with the predictions of the refined

two-temperature model presented at the end of the chapter.

5.2 Sample fabrication and characterisation

To investigate the dependence of the ultrafast PL signal on carrier density, a set of contacted samples on Si/SiO_2 substrates was created using electron beam lithography - see Section 2.2.5 for the details. Substrates with graphene samples were mounted into ceramic packages, and bonding pads on the substrates were connected to the contacts on the packages using ultrasonic wire bonding. The carrier concentration in the samples was controlled by applying a voltage between graphene and a highly-doped silicon gate, and the position of the Fermi level was identified using $R(V_g)$ measurements.

Sample resistance was measured in a constant-current regime. The oscillating voltage with an amplitude of 0.1 V and a frequency of 5.071 kHz was generated by a lock-in amplifier (Model 7270, Signal Recovery), and a 1 MΩ ballast resistor was connected in series to the sample to ensure a constant amplitude of the alternating current in the circuit of $I = 100$ nA. The resistance of graphene was then measured by recording the voltage drop across the sample.

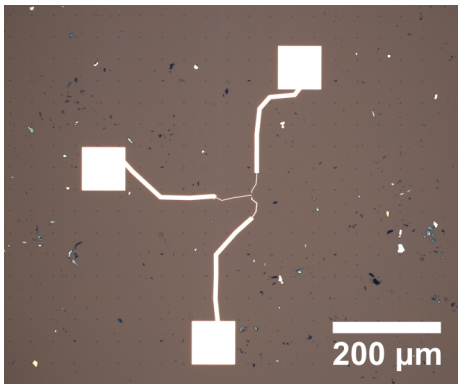

Figure 5.1: Optical micrograph of a graphene sample on a Si/SiO_2 substrate showing metallic contacts connecting the graphene flake in the middle with the large contact pads prepared for wire bonding.

The $R(V_g)$ characteristics were recorded by applying a sinusoidal voltage to the gate electrode (±10 V at 0.2 Hz). The position of the Fermi level was identified by measuring the shift of the resistance maximum.

Excitation pulses centred at 775 nm were generated by Levante OPO and focused onto the sample using a 20x lens. The intensity of the up-converted PL signal, isolated with 750 nm short-pass filters, was measured by a photomultiplier tube.

The dependence of the PL intensity on the Fermi level position was investigated by studying the correlation between the sample resistance and up-converted PL intensity for a varying gate voltage.

Figure 5.1 shows the optical microscopy image of a graphene sample on a silicon substrate with electric contacts created using electron beam lithography. The graphene flake located in the middle of the picture is connected to the 200 μm-by-200 μm bonding pads that provide an area for ultrasonic wire bonding.

Graphene field-effect transistors fabricated on Si/SiO_2 substrates can experience significant gate hysteresis, i.e. changes of the charge neutrality point position (resistance maximum) depending on the direction of the gate voltage sweep. The hysteresis is presumed to arise from the injection of charge carriers into trapping centres in the oxide layer [92, 161] or charge transfer from molecules adsorbed at the surface of graphene [91, 94]. Variation of the gate voltage corresponding to the charge neutrality point V_{CNP} depends on the rate and range of the gate voltage sweep, as well as the surrounding environment.

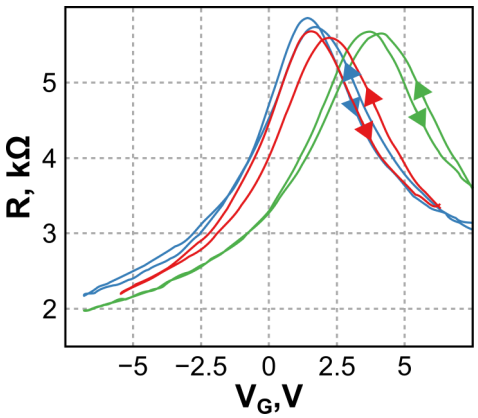

Figure 5.2: Changes in the $R(V_g)$ dependence of a graphene sample in ambient atmosphere. **(blue)** The initial $R(V_g)$ dependence of the sample. **(green)** $R(V_g)$ characteristic of the sample after 80 seconds of continuous gating. **(red)** $R(V_g)$ of the sample several minutes after the gate was grounded. The arrows indicate the direction of the gate voltage sweep.

Besides the gate hysteresis, the samples investigated in an ambient atmosphere were found to show increasing hole doping under a continuously applied gate voltage. The blue curve in Figure 5.2 represents the intrinsic $R(V_g)$ dependence of a graphene FET. The charge neutrality point (CNP) is located at 1.5 V, indicating a low level of hole doping with the chemical potential $\mu = -70$ meV. A sine wave with a frequency of 0.2 Hz and an amplitude of 10 V was then applied to the gate electrode. After 80 seconds of continuous measurements, V_{CNP} has shifted to 2.6 V, indicating the

decrease in the Fermi level position by 40 meV. This effect appears to be triggered by the gating of the sample: with no voltage applied to the gate, the sample returns to its original state after several minutes (red curve in Fig. 5.2).

The increasing doping of the samples under continuous gating may be caused by the adsorption of the atmospheric oxygen to the surface of graphene. Changes of the oxygen adsorption rate due to the variation of the Fermi level position have been reported previously for electrically gated bilayer graphene [162].

To minimise the influence of the atmosphere on graphene during electro-optical measurements, the substrates with graphene samples were coated with a thin layer of PMMA. Though PMMA is commonly used as a positive photoresist for electron beam lithography, it has very weak absorption in the visible and near-infrared wavelength ranges [163]. PMMA was spun onto the substrates at 5000 rpm and baked on a hotplate at 120 C° for 10 minutes to reduce the remaining solvent concentration. The second step of lithography was then performed on the samples to remove PMMA from the bonding pads on the substrate.

The samples with the protective polymer layer demonstrated no variation of the doping level after prolonged sweeping of the gate voltage. This indicated that the observed effect was indeed caused by the interaction with atmospheric molecules. However, these samples still experience CNP hysteresis. For the sake of clarity, the $R(V_g)$ curves are henceforth plotted only for the reverse direction of the gate voltage sweep.

Significant changes of the CNP position were observed in samples upon photoexcitation. Figure 5.3 compares the R(V_g) characteristics of a sample before, during, and after photoexcitation. Prior to excitation, the CNP of the sample is located at 4.3 V **(blue line)**, which corresponds to $\mu = -120$ meV. Upon photoexcitation, the resistance maximum is shifted to -3.6 V **(red line)**, indicating significant photoinduced doping with $\Delta\mu = 240$ meV and the change in the type of majority charge carriers from holes to electrons.

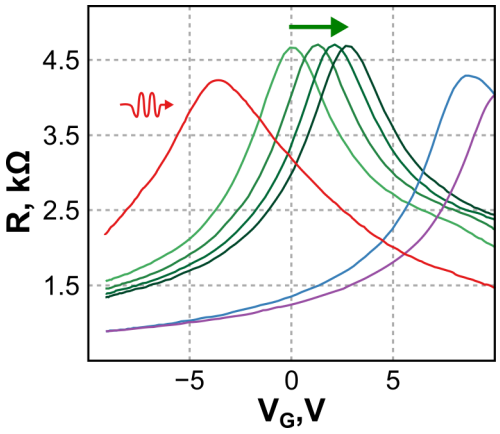

Figure 5.3: Photoinduced doping in graphene samples on Si/SiO_2 substrates **(blue)** R(V_g) dependence of pristine sample. **(red)** R(V_g) curves of the photoexcitation sample. **(green)** Changes in the CNP position shortly after photoexcitation; time delay between adjacent curves is 0.5 s. **(magenta)** R(V_g) dependence 1 minute after the end of photoexcitation.

After the end of excitation, the photoinduced doping gradually decreases over time. The green curves in Figure 5.3 shows the R(V_g) characteristics recorded with 0.5 second intervals after the excitation beam had been blocked. Magenta curve represents the R(V_g) dependence measured 1 minute after the end of photoexcitation, when changes of V_{CNP} had stabilised completely. The resistance maximum is shifted to a higher voltage compared to the pristine sample, indicating a stable increase of hole doping due to the photomodification of the sample.

Temporary photoinduced n-doping appears to be caused by charge trapping in the oxide layer [91, 161, 164–167], as a similar response was observed for excitation of the substrate in the vicinity of the graphene sample.

5.3 Dependence of photoluminescence intensity on charge carrier concentration

The modulation of the voltage applied to the gate leads to the variation of the Fermi level position around the point defined by the doping of the sample, with $E_F = 59.6\sqrt{|V_{CNP} - V_g|}$ (see Section 2.2.6 for details). As the gate voltage corresponding to the resistance maximum may change during the measurement due to photoinduced electron doping and photomodification, the value of the gate voltage alone cannot be used to calculate the Fermi level position. However, as the shape of the $R(V_g)$ dependence remains to a large extent unmodified, the resistance of the sample can be used to qualitatively describe the changes in the carrier concentration.

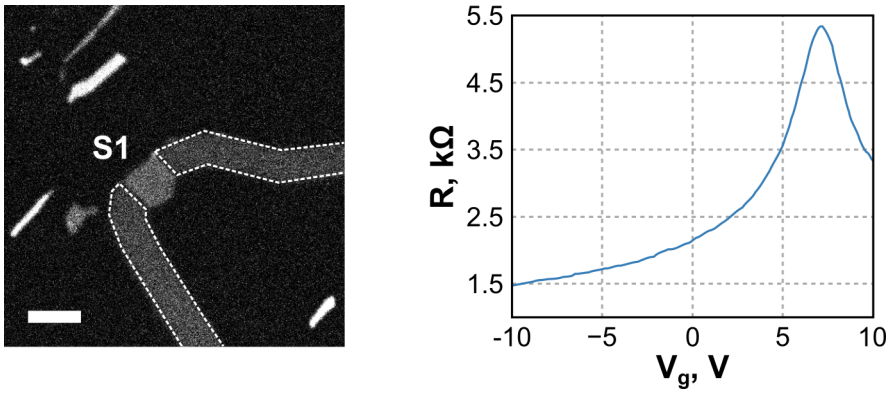

Figure 5.4: **(left)** PL image of a graphene sample on a silicon substrate with the dashed lines indicating gold contacts. Scale bar, 3 μm. **(right)** $R(V_g)$ dependence of the sample recorded before the beginning of measurements.

Figure 5.4 **(left)** shows the PL image of a contacted sample S1 on a silicon substrate. The dashed lines indicate the gold contacts that are visible in the PL image due to two-photon luminescence [168, 169]. The $R(V_g)$ dependence recorded prior to photoexcitation indicate that the sample is p-doped with the Fermi level shifted down from the Dirac point by 160 meV (Fig. 5.4 **(right)**).

The carrier density in the sample was modulated by a sinusoidal voltage with a frequency of 0.2 Hz and an amplitude of 10 V that was applied to the gate electrode. Figure 5.5 **(left)** plots temporal evolution of the up-converted PL intensity **(blue)** and the sample resistance **(green)** for excitation with 0.5 mJ/cm^2 pulses centred at 775 nm. The resistance peaks that occur when the Fermi level crosses the charge neutrality point are clearly visible. The paired, symmetric peaks in resistance correspond to the different directions of gate voltage sweep, with some difference in the peak shape and height caused by hysteresis effects. A relatively low intrinsic hole

doping and photoinduced electron doping lead to the resistance maximum being located at -4 V (-2 V) for forward (reverse) gate sweep.

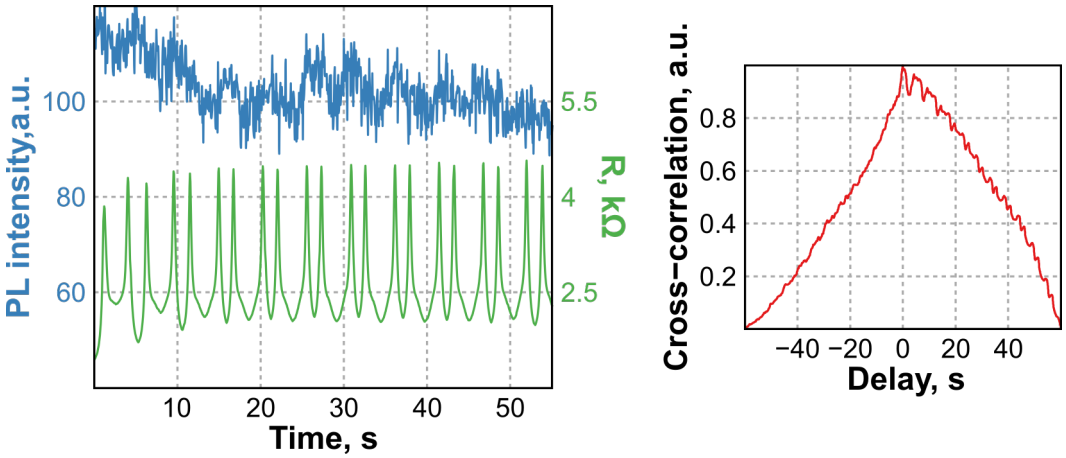

Figure 5.5: **(left)** Temporal evolution of the up-converted PL intensity **(blue)** and sample resistance **(green)** for 0.2 Hz AC voltage with the amplitude of 10 V applied to the gate electrode. Paired symmetric peaks in resistance correspond to the Fermi level crossing the Dirac point during forward and reverse gate sweeps. **(right)** Plot of the cross-correlation between the sample resistance and the PL intensity.

The cross-correlation plot (Fig. 5.5 **(right)**) represents the degree of similarity between two time series. The linear decrease of the correlation function with increasing lag is caused by finite size of the experimental data. The repeating local maximum (minimum) that occur when a peak in the sample resistance coincides with a peak (trough) in the PL intensity indicate clear correlation between two signals. These local extrema are more apparent for positive lag, suggesting that the degree of similarity between two signals decreases with increasing exposure time.

Though Figure 5.5 demonstrates a correlation between two signals, with the PL intensity showing slightly higher values when the Fermi level is positioned at the Dirac point, gate-induced modulations of the PL intensity are comparable with the overall change of the PL signal caused by the photomodification of the sample.

The range of the Fermi level positions accessible with a silicon back gate is limited by the breakdown of the oxide layer. To investigate the dependence of the PL intensity on the carrier concentration for higher doping levels, the intrinsic carrier density in a graphene sample was increased using photomodification.

Figure 5.6 **(right)** compares the $R(V_g)$ characteristic of the sample S2 before and after 20 minutes exposure to 1.5 mJ/cm^2 excitation. The resistance maximum in the sample before modification is located at 3.7 V, indicating a low level of hole doping with $\mu = -115$ meV. A higher overall resistance of the sample is caused by

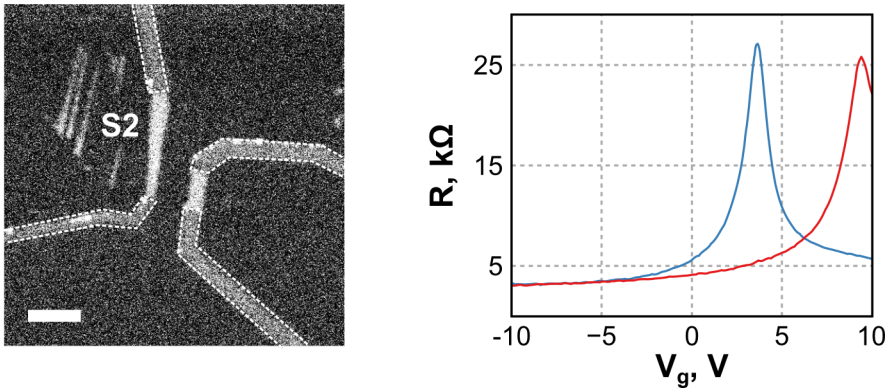

Figure 5.6: **(left)** PL image of the sample S2 after 20 minutes modification with 1.5 mJ/cm^2 pulses centred at 775 nm. Scale bar, 3 μm. **(right)** R(V_g) characteristics of the sample before (blue) and after (red) photomodification.

the elongated shape of the flake (see Fig. 5.6 **(left)**). After photomodification, the resistance peak is shifted to 9.4 V, indicating a 70 meV downshift of the Fermi level.

Remarkably, though the protective layer of PMMA reduced the rate of photomodification, it did not prevent it completely, suggesting that the molecules that take part in the modification process were trapped at the graphene/oxide or graphene/polymer interface.

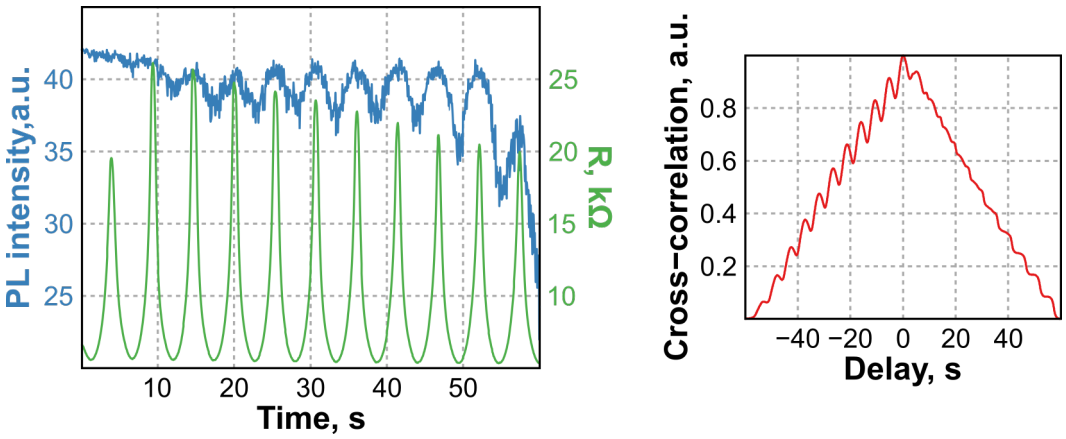

Figure 5.7: **(left)** Temporal evolution of the up-converted PL intensity **(blue)** and sample resistance **(green)** for the sample S2 after photomodification. The peak in resistance occurs when the Fermi level approaches the charge neutrality point. **(right)** Cross-correlation function of the up-converted PL intensity and the sample resistance.

In order to dynamically change the doping level during the measurement through photomodification, a higher excitation power was focused onto a single point of the sample. Figure 5.7 **(left)** plots the resistance of the sample **(green)** and the PL intensity **(blue)** as a function of time for 1.5 mJ/cm^2 excitation. Unlike the signal

in Figure 5.5, the resistance maxima do not indicate the position of the CNP: as the sample is highly doped, variation of the Fermi level position caused by gating is not sufficient to cause the change in the charge carrier type. The peaks in resistance observed in Figure 5.7 occur when the Fermi level approaches the Dirac point; however, even for the maximum value of the gate voltage it does not cross it.

As the sample is exposed to the laser light, a further increase in the doping level occurs due to the photomodification. It can be seen from Figure 5.7 that the maximum value of resistance decreases with increasing exposure time, indicating that the CNP moves to higher values of gate voltage.

At the beginning of the measurement, the PL signal produced by the sample shows only a weak modulation due to the varying gate voltage. However, the magnitude of the gate-induced changes of the PL intensity increases significantly as the sample gets more doped. The maxima of the PL intensity show an excellent correlation with the peaks in the sample resistance. Remarkably, even though the overall PL intensity decreases with exposure time, the value of the PL corresponding to the peaks in resistance, i.e. when the Fermi level approaches the Dirac point, remains to a large extent unchanged.

The identical behaviour, i.e. weak correlation between the PL intensity and the resistance in pristine samples that becomes much stronger as a result of photoinduced doping, has been observed in five different samples.

Figure 5.7 **(right)** shows the cross-correlation between the PL and resistance data. Unlike the correlation data for the sample S1 (Fig. 5.5 **(right)**), the periodic local minima and maxima are more pronounced in the negative lag region. This dissimilarity arises from the difference in the doping level. The sample S1 demonstrates a low level of n doping that gradually decreases with increasing exposure time due to the photomodification of the sample. On the other hand, the pre-modified sample S2 has intrinsically high level of hole doping that increases further during the photoexcitation. In both cases, as the Fermi level moves away from (towards) the Dirac point, the PL intensity dependence on the carrier concentration becomes stronger (weaker), increasing (decreasing) the shape similarity between the two signals.

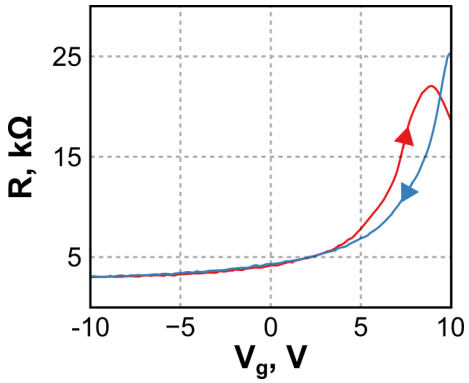

Figure 5.8: The dependence of the sample resistance on the gate voltage after the photomodification. The red and blue curves correspond to the forward and reverse gate sweeps respectively.

The $R(V_g)$ characteristic of the sample after the measurement (Fig. 5.8) shows a further increase in the doping level. Though the resistance peak was shifted only by 0.5 V, a higher increase of doping is expected in the modified region, as $R(V_g)$ reflects the average concentration of the charge carriers in the sample. The photomodified sample demonstrates a high degree of hysteresis, with $R(V_g)$ curves for forward (red) and reverse (blue) direction of the gate voltage sweep having significantly different shapes.

5.4 Coupled rate equation model

In order to get a better understanding of the PL intensity dependence on the carrier concentration in graphene, a refined two-temperature model[1] was used to calculate the dynamics of the photoexcited electron relaxation.

As the two-temperature model relies on the charge carriers being in internal equilibrium, it may not by applicable to the case of picosecond excitation, since a lower instantaneous carrier density makes the energy exchange between electrons less efficient [63, 123]. However, the photomodified areas are clearly visible in the PL images created using a 180 fs excitation, suggesting that the effects of increasing doping are similar in both cases.

The temporal dynamic of the charge carrier distribution was calculated using a set of coupled differential equation for electron temperature T_e and optical phonon occupation numbers n_{ph}:

$$\frac{dT_e}{dt} = \frac{I(t) - 2 \cdot \Gamma_{\mathrm{ph}} \hbar\omega_{\mathrm{ph}}}{C_e} \tag{5.1}$$

$$\frac{dn_{\mathrm{ph}}}{dt} = \frac{\Gamma_{\mathrm{ph}}}{M_{\mathrm{ph}}} - \frac{n_{\mathrm{ph}} - n^0_{\mathrm{ph}}}{\tau_{\mathrm{ph}}}. \tag{5.2}$$

Here, $I(t)$ is the absorbed laser irradiance, $\hbar\omega_{ph}$ is the optical phonon energy, C_e is the electronic heat capacity, M_{ph} is the number of phonon modes participating in e-ph scattering, n^0_{ph} is the phonon occupation at room temperature, and τ_{ph} is the optical phonon decay rate.

The sensitivity of the coupled rate equations to the Fermi level position arises from the electron-phonon energy exchange rate Γ_{ph} [57, 170, 171]

$$\Gamma_{ph} = \alpha \int_{-\infty}^{+\infty} dE\, \nu(E)\nu(E - \hbar\omega_{ph}) \cdot [\rho_e - \rho_a], \tag{5.3}$$

where α represents the electron-phonon coupling strength, $\nu(E)$ is the density of electronic states, and ρ_e and ρ_a are the probabilities of emitting and absorbing a phonon for a given energy of electron given by the following expressions

$$\begin{aligned} \rho_e &= f(E, T_e, \mu)\ (1 - f(E - \hbar\omega_{ph}, T_e, \mu))\ (n_{ph} + 1) \\ \rho_a &= f(E - \hbar\omega_{ph}, T_e, \mu)\ (1 - f(E, T_e, \mu))\ n_{ph}. \end{aligned} \tag{5.4}$$

The Fermi-Dirac distributions $f(E, T_e, \mu)$ in Equation 5.4 originate from Fermi's

[1] See Section 1.4.1 for the original model

golden rule and describe the requirement for the initial (final) state of the scattering process to be occupied (vacant).

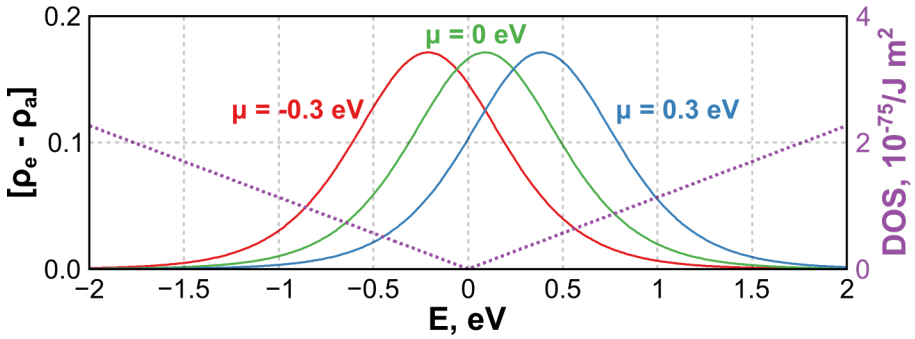

Figure 5.9: **(solid lines)** The difference between the phonon emission and absorption probabilities $[\rho_e - \rho_a]$ as a function of electron energy calculated for $T_e = 3000$ K, $T_{ph} = 300$ K and various values of chemical potential μ. **(dotted line)** The density of electronic states in graphene as a function of the charge carrier energy.

Figure 5.9 plots the difference between the phonon emission and absorption probabilities $[\rho_e - \rho_a]$ calculated for $T_e = 3000$ K, $n_{ph} = 9.5 \cdot 10^{-4}$ ($T_{ph} = 300$ K) and different values of the chemical potential μ. Though the increasing electron (hole) doping causes a shift of the probability distribution to a higher (lower) energy, the shape of the curves remains unchanged.

The e-ph energy exchange rate depends on the density of the initial and final states of the scattering process, $\nu(E)$ and $\nu(E - \hbar\omega_{ph})$. As the density of electronic states in graphene is a linear function of the charge carrier energy (dotted magenta line in Fig. 5.9), the scattering probability increases with increasing energy of electron.

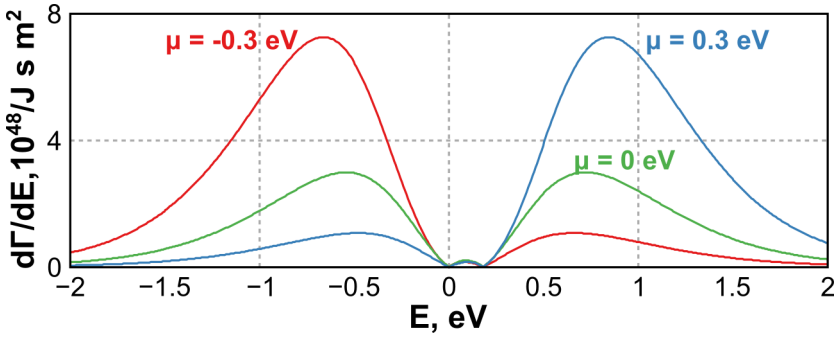

Figure 5.10: The electron-phonon energy exchange rate as a function of electron energy for $\mu = -0.3$ eV **(red)**, 0 eV **(green)** and 0.3 eV **(red)**.

Figure 5.10 shows the rate of energy exchange between electron and phonon systems as a function of the carrier energy. For undoped graphene, the distribution

has a symmetric shape, with both types of charge carriers having an equal scattering probability. However, as the Fermi level moves away from the Dirac point, the scattering probability for the majority carriers significantly increases. Therefore, the overall optical phonon generation rate, given by the integrated area under the curves, also increases with increasing carrier concentration.

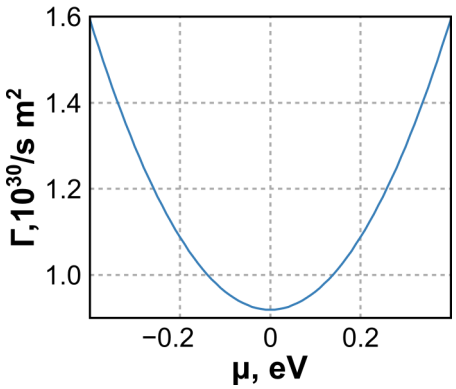

Figure 5.11: The heat transfer rate between electrons and optical phonons as a function of the chemical potential.

The electron-phonon heat transfer rate for various values of the chemical potential is plotted in Figure 5.11. It has the minimum value when $\mu = 0$ eV. As the Fermi level moves away from the Dirac point, a larger phase space becomes available for electron scattering, making e-ph heat transfer more efficient.

5.4.1 Temperature dependence of chemical potential

With the extremely high carrier temperatures achieved during photoexcitation, the temperature dependence of the chemical potential has to be taken into account when calculating the relaxation dynamic of the photoexcited charge carriers.

The chemical potential μ, also commonly called the Fermi level, is the total electrochemical potential of charge carriers in graphene. At absolute zero temperature, the chemical potential is equal to the Fermi energy ϵ_F, i.e. the energy of the top-most occupied electronic state. The variation of μ with increasing carrier temperature can be calculated by considering the conservation of the total electron density [172, 173]

$$n = \int_0^\infty d\epsilon\, \nu(\epsilon)\, (f(E, T_e, \mu) - f(E, T_e, -\mu)) = \frac{\epsilon_F^2}{\pi \hbar^2 v_F^2}, \tag{5.5}$$

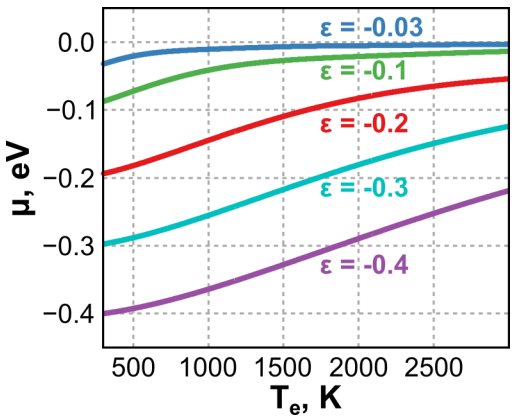

Figure 5.12: The chemical potential dependence on the charge carrier temperature for various values of the Fermi energy.

Figure 5.12 plots the chemical potential as a function of electron temperature for various values of the Fermi energy obtained by numerically inverting Eq. 5.5. At room temperature, $\mu \sim \epsilon_F$, and the absolute value of μ decreases with increasing electron temperature.

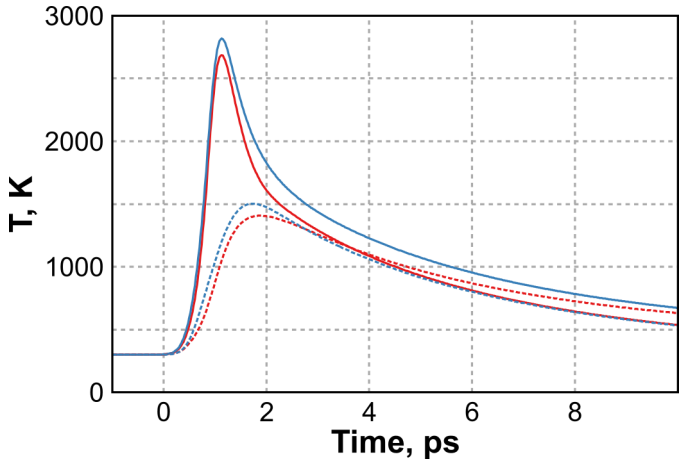

Figure 5.13: The temporal evolution of the electron **(solid lines)** and phonon **(dashed lines)** temperatures calculated for photoexcitation with a 180 fs pulse with the fluence of 0.1 mJ/cm^2. The blue and red curve correspond to the relaxation dynamics for Fermi energy of -0.1 eV and -0.4 eV respectively.

Figure 5.13 compares the temporal dynamics of the electron and phonon temperatures for excitation with a 180 fs pulse with the fluence of 0.1 mJ/cm^2 calculated for $\epsilon_F = -0.1$ eV **(blue)** and $\epsilon_F = -0.4$ eV **(red)**. The solid lines correspond to the electron temperatures while the dashed lines represent the phonon temperatures. Increasing hole doping leads to a more efficient energy exchange between electron and phonon systems, increasing the rate of the electron relaxation.

5.4.2 Effects of electron heat capacity

The heat capacity is a physical quantity defined by the ratio of the absorbed heat and the change of the system temperature $C = \partial U/\partial T$. The heat capacity of electrons is described by the following expression [174]

$$C_e = \frac{\partial U}{\partial T_e} = \int_0^\infty d\epsilon(\epsilon - \epsilon_f)\nu(\epsilon)\frac{df(E, T_e, \mu)}{dT_e}. \tag{5.6}$$

The temperature evolution in Figure 5.13 was calculated using the electron heat capacity obtained by analytically solving Eq. 5.6 in a high temperature limit ($k_B T_e \gg |\epsilon_F|$) [71, 175]:

$$C_e(T_e) = \frac{18\zeta(3)}{\pi(\hbar v_F)^2} k_B^3 T_e^2, \tag{5.7}$$

where $\zeta(3) = 1.202$ is the zeta function. Another analytical solution can be obtained for the high doping regime ($k_B T_e \ll |\epsilon_F|$) [174, 176]

$$C_e = \frac{2\pi}{3}\frac{\epsilon_F}{(\hbar v_F)^2} k_B^2 T_e. \tag{5.8}$$

However, as for a non-zero intrinsic carrier concentration the electron system can go through both regimes during photoexcitation, it is important to ensure that the correct estimate of the electron heat capacity is used.

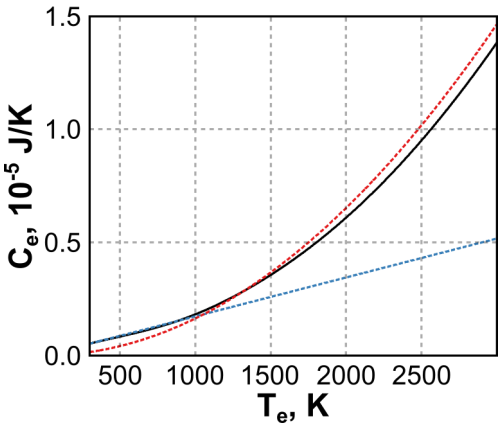

Figure 5.14: The heat capacity of electrons calculated numerically **(black)** and analytically in the high temperature **(red)** and high doping **(blue)** limits for $\epsilon_F = -0.3$ eV.

Figure 5.14 compares the electron heat capacity obtained by numerically solving Eq. 5.6 while taking into account the temperature dependence of the chemical potential **(black)** with the analytical results for the high temperature **(red)** and high

doping **(blue)** limits for $\epsilon_F = -0.3$ eV. As it can be seen, the high temperature approximation is very close to the result of numerical calculations in a wide range of carrier temperatures.

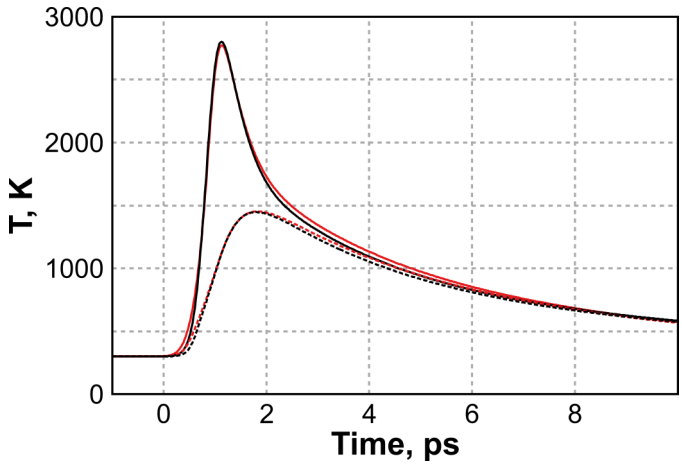

Figure 5.15: The temporal dynamics of the electron and phonon temperatures calculated in the high temperature limit **(red)** and using a numerical solution for the electron heat capacity **(black)**. The solid (dashed) lines correspond to the electron (phonon) temperature.

The use of the numerical solution for the electron heat capacity results only in small corrections to the electron relaxation dynamics that mostly affect the lower temperature part of the relaxation process (see Fig. 5.15). As the PL signal has a strongly nonlinear dependence on the charge carrier temperature [71], these changes do not have any significant effect on the resulting PL intensity.

5.4.3 Emission intensity

As the ultrafast PL signal generated using femtosecond excitation arises from recombination of a thermalised electron distribution, its emission spectrum can be described using Plank's law [71]:

$$\mathcal{F}(\hbar\omega, T_e) \propto \frac{\omega^3}{2\pi^2 c^2} \frac{1}{e^{\hbar\omega/k_B T_E} - 1} \tag{5.9}$$

The total intensity of the up-converted PL can be calculated using the temporal dynamic of T_e and integrating the emission over the detected wavelength range ($\lambda < 750$ nm).

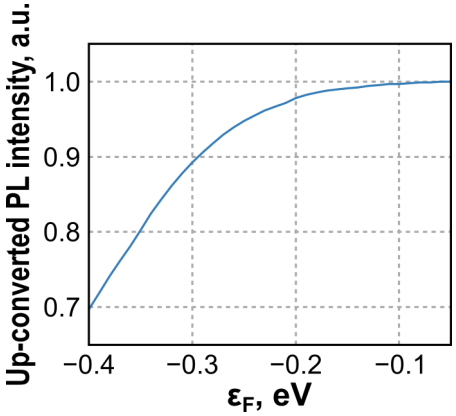

Figure 5.16: The intensity of the up-converted PL signal as a function of the Fermi energy calculated using the refined two-temperature model.

Figure 5.16 plots the variation of the PL intensity for increasing hole doping. The intensity of the up-converted PL has the maximum value for $\epsilon_F = 0$ eV and decreases as the Fermi level moves away from the Dirac point[2].

The dependence of the PL intensity on the Fermi energy calculated using the two-temperature model is in good agreement with the experimental results presented in Figures 5.5 and 5.7. Due to the intrinsically low doping of sample S1, the oscillating gate voltage leads to the variation of the Fermi energy in the -175 to 200 meV range. As the gradient of the I(PL) dependence in this region is very low, the change of the gate voltage result in only a weak modulation of the PL intensity. However, as the sample S2 had been highly doped using the photomodification, its Fermi energy was located in the region with an increasingly higher gradient ($\epsilon_F \sim -270 \div 0$ meV), resulting in a strong dependence of the PL intensity on the gate voltage.

[2]The PL intensity dependence on the carrier density for electron doping has an identical shape and is not shown here.

5.5 Summary

In summary, the dependence of the up-converted PL intensity on the intrinsic charge carrier concentration was investigated using electro-optical measurements. The carrier density in graphene field-effect transistors was modulated using gate electrode and controlled photomodification.

The up-converted PL intensity has a maximum value when the Fermi level is located at the Dirac point and decreases with increasing doping. The strength of the luminescence intensity dependence on the Fermi level position varies with intrinsic carrier population. Samples with a low intrinsic doping show only a weak modulation of the PL intensity with the varying Fermi energy. However, the signal intensity dependence on the carrier concentration becomes increasingly more distinct as sample gets more doped.

Changes of the charge neutrality point position with respect to gate voltage caused by gate hysteresis and photoinduced electron doping make it difficult to extract the exact value of the chemical potential from the transport measurements. As the shape of the $R(V_g)$ dependence changes over time due to the modification of sample mobility, further studies are required to directly link the resistance and Fermi level position.

These difficulties are associated with the Si/SiO_2 substrate and could be overcome by depositing graphene on a quartz substrate and using polymer top gate to control the carrier concentration in graphene. However, the excitation fluences required to achieve a detectable level of PL signal were found to cause melting of the polymer and consequential tearing of the graphene samples.

Nevertheless, the sensitivity of the up-converted PL signal to the carrier density makes it a promising tool for the high-resolution spatial mapping of the Fermi level position in graphene samples.

Chapter 6

Probing relaxation dynamics using two-pulse correlation measurements

6.1 Introduction

In this chapter, the preliminary results of the investigation of the photoinduced changes in the electron relaxation rates using two-pulse correlation measurements are presented. The relaxation dynamics of the photoexcited charge carriers is probed directly by measuring the intensity of the up-converted PL signal as a function of the temporal delay between two ultrashort laser pulses. The correlation signals recorded in the regions of a monolayer flake with various degrees of modification-induced reduction of the PL intensity are compared with the signal of pristine graphene. The changes in the height and width of the correlation trace suggest an increase in the relaxation rates of hot charge carriers.

6.2 Experimental setup

To investigate the photoinduced change of relaxation times of hot carriers more directly, the changes in the temporal dynamics of the PL process were probed using two-pulse correlation measurements [71]. In this technique, the intensity of the PL signal is measured as a function of the temporal separation between two ultrashort laser pulses.

The origin of the correlation signal lies in the nonlinear dependence of the PL intensity on the electron temperature T_e. The PL intensity is predominantly defined by the maximum value of T_e reached during excitation [71]. It is achieved when the two pulses have a perfect temporal overlap and decreases with increasing separation between them, reaching saturation for delays larger than the characteristic relaxation time of hot carriers in graphene [52, 54, 57, 62].

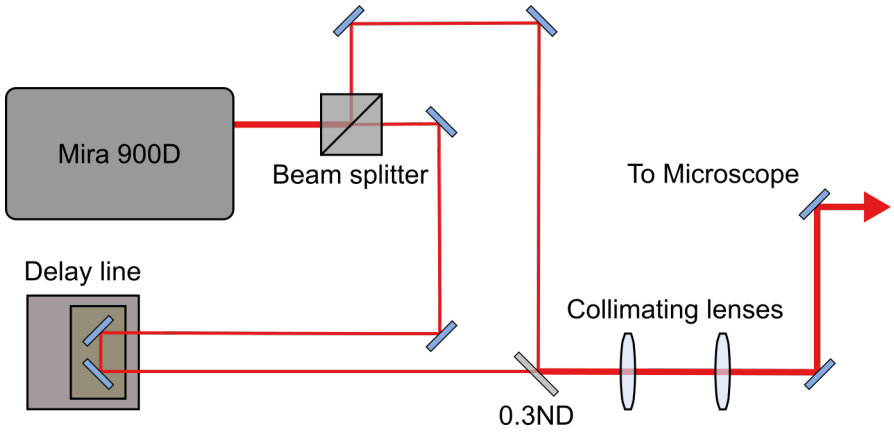

Figure 6.1: Schematic diagram of the two-pulse correlation setup

The optical setup used for the correlation measurements is illustrated in Figure 6.1. The excitation beam was split by a polarising beam splitter into two equal intensity pulses ("pump" and "probe") that were later recombined using a 0.3 OD neutral density filter. The temporal separation between the two pulses was controlled by changing the path length of the "probe" pulse using the motorised delay line. The orthogonal polarisation of the excitation pulses allowed interference effects to be minimised, but at the same time did not affect the measurement itself since the PL is not sensitive to the polarisation of the excitation pulse [71].

The excitation beams were aligned collinearly through a pair of widely spaced pinholes and an individual set of collimating lenses was used for each of the beams to optimise the overlap between the two focal volumes (not shown in Fig. 6.1). Prior to all measurements, the PL intensity generated by the "probe" pulse only was

recorded for different positions of the delay line to ensure that the beam alignment remains constant.

For the correlation measurements, the fluence of the individual pulses was set to 0.07 mJ/cm^2 to ensure that no optical damage was induced in graphene. The final correlation traces were obtained by averaging multiple signals recorded for the different directions of the delay line scans.

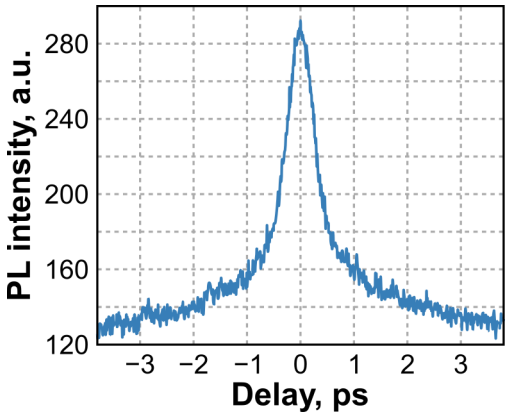

Figure 6.2: The upconverted PL intensity as a function of temporal separation between two 180 fs pulses recorded in a pristine few-layer graphene sample.

Figure 6.2 shows the correlation trace recorded in a pristine few-layer graphene sample. The change in the slope of the PL intensity decrease at $\sim$ 500 fs separation indicates the moment when the electron and optical phonon systems achieve thermal equilibrium [52, 54, 63].

6.3 Photoinduced modification of hot carrier relaxation rates

The two-pulse correlation measurements were performed on different regions of a monolayer flake modified using the picosecond excitation. Figure 6.3 **(a)** shows the PL image of the sample after photomodification. By varying the total exposure time, the PL intensity reduction of 50%, 60%, and 65% was achieved in three square areas of the flake.

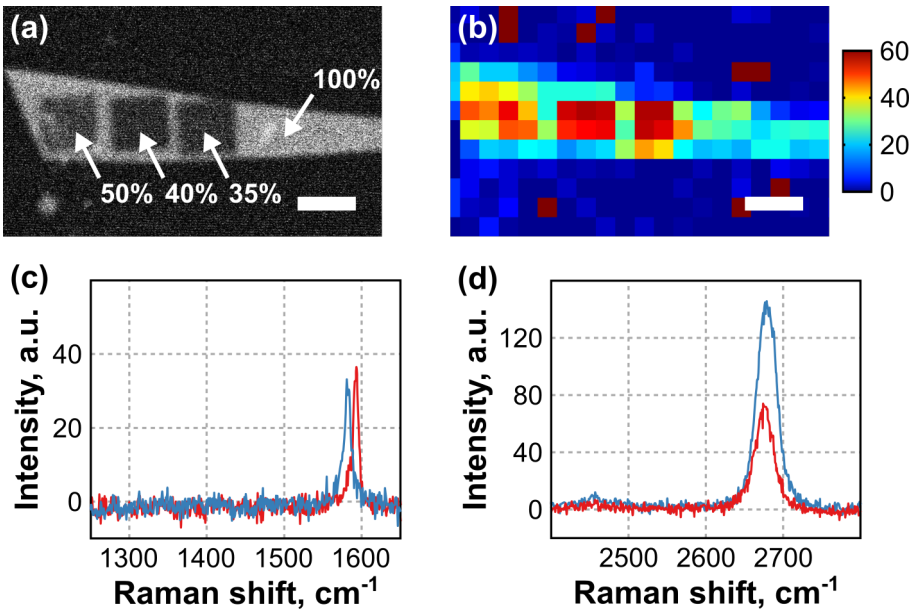

Figure 6.3: **(a)** The PL image of a monolayer graphene flake after photomodification. The numbers indicate the PL intensity in percent of the pristine value. **(b)** The Raman map of the flake plotting the intensity of the G peak. **(c)** and **(d)** The Raman spectra collected in the central square region before **(blue)** and after **(red)** photomodification. All scale bars, 3 μm.

The Raman map of the sample (Fig. 6.3 **(b)**) shows a higher intensity of the G peak in the modified regions, indicating an increased level of doping. However, the Raman spectra recorded after photomodification do not contain the defect-activated D peak, which indicates that no structural defects were created in the sample during the photomodification (Fig. 6.3 **(c)** and **(d)**).

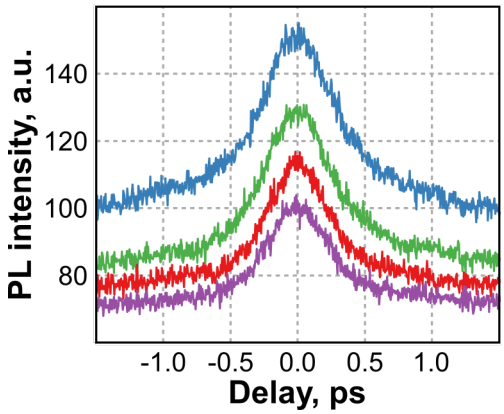

Figure 6.4: The two-pulse correlation traces recorded in a pristine sample **(blue)** and the photomodified regions with 50% **(green)**, 60% **(red)** and 65% **(magenta)** reduction of the PL intensity.

Figure 6.4 compares the TPC signal of the pristine monolayer graphene **(blue)** with the signals recorded in the photomodified areas with 50% **(green)**, 60% **(red)**, and 65% **(magenta)** decrease of the PL intensity. The photomodification leads to an overall reduction of the PL intensity i.e. the background level of the correlation signal, as well as a change in the shape of the correlation peak.

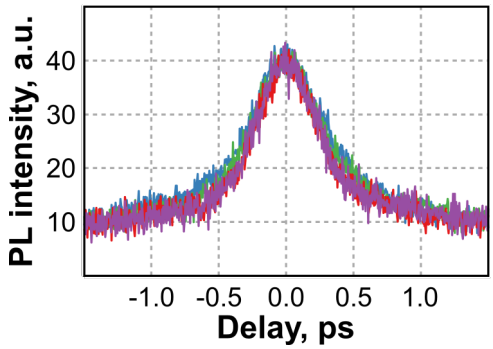

Figure 6.5: The correlation traces recorded in the different regions of the sample and normalised to the same height to allow direct comparison.

The variation of the peak intensity makes it difficult to compare the TPC signals recorded in the different regions of the modified flake. Figure 6.5 plots the correlation traces normalised to the same height to allow direct comparison. As it can be seen, the photomodification leads to sharpening of the TPC signal, with the width of the peak showing a direct correlation with the decrease of the PL intensity.

The width of the correlation trace for pristine graphene is determined both by the laser pulse width and the relaxation kinetics of hot carriers. The observed changes in the TPC peak width can be explained by an increase in relaxation rates of hot carriers. For the same temporal separation, electrons in the modified areas excited

by the first pulse can cool down to lower temperatures before the arrival of the second pulse, resulting in a lower overall PL intensity.

6.4 Summary

In summary, the changes in the relaxation dynamics of hot photoexcited carriers caused by the photomodification of graphene were probed directly using two-pulse correlation measurements. The preliminary results show a reduction of the height and sharpening of the correlation peak in the modified regions. The variation of the two-pulse correlation signal may indicate an increase in the carrier relaxation rate. However, further experimental and theoretical investigations are required to identify methods of extracting quantitative information from the correlation signal.

The two-pulse correlation measurements can be combined with ultrafast PL imaging, making it a promising technique for obtaining spatially-resolved information about the charge carrier relaxation dynamics in graphene.

Chapter 7

Conclusions and Future Work

In this project, the sensitivity of the ultrafast PL to the properties of graphene was investigated by studying the variation of the PL signal caused by the photomodification of the sample. It was found that the interaction with near-infrared picosecond pulses results in the stable change of the graphene properties, which manifests itself in the reduction of the PL intensity. The photoinduced changes were studied using a combination of optical, transport and scanning probe measurements.

The variations of the Raman spectra and transport characteristics of the samples show that photomodification leads to a significant increase in the level of hole doping as well as a change in the mechanical strain. Using atomic force microscopy, these changes were linked to a considerable increase in the roughness of the graphene surface. Though very similar to the slippage and buckling observed in thermally annealed graphene [88, 90], this effect is not a result of the steady-state heating, but arises from the extremely high electron and phonon temperatures achieved with ultrashort photoexcitation. The strong environmental sensitivity suggests that interaction with atmospheric oxygen and moisture plays a vital role in the photomodification process.

The reduction of the PL intensity after photomodification was associated with the photoinduced doping. The electro-optical measurement performed on graphene-based field-effect transistors have demonstrated that the PL intensity has a maximum value in undoped graphene and decreases with increasing carrier density. The changes of the PL intensity with increasing doping were attributed to an increase in the relaxation rate of the photoexcited charge carriers.

This finding was confirmed using the refined two-temperature model, with the theoretical predictions showing good agreement with the experimental results. The doping-induced increase in the electron relaxation rate was also observed directly in the two-pulse correlation measurements.

7.1 Controlling oxidation of graphene with photomodification

Due to the stability and localised nature of the photoinduced changes, the photomodification can be utilised for high-resolution patterning of graphene. For example, the photoinduced doping can be used to enhance the performance of graphene photodetectors through the formation of spatially controllable p-n junctions [167, 177]. Another promising application of photomodification is controlling the functionalisation of graphene, as molecules adsorbed at the surface, as well as an increased surface roughness, will affect its chemical reactivity.

A wide range of graphene derivatives has been created using chemical modification [178]. One of the graphene-based materials that has recently attracted the most research interest is graphene oxide [26, 179]. Commonly obtained by the oxidation of graphite, it can be reduced to almost pristine graphene, providing one of the most efficient methods of large-scale graphene synthesis. Graphene oxide has found its applications in a wide spectrum of areas, ranging from composite materials [180, 181] and energy storage [182–186] to cancer treatment [187–190].

For electronic applications, the most attractive property of graphene oxide is that, unlike graphene, it has a band gap which can be tuned by varying the degree of oxidation [191, 192]. Graphene oxide can be incorporated into existing devices by selective functionalisation of graphene with oxygen plasma treatment [193–195].

This section reports the results of the first attempt to control the oxidation of graphene using photomodification. Prior to functionalisation, several square areas of graphene were modified using picosecond excitation. Figure 7.1 **(a)** shows the PL image of the flake after photomodification, with three 3 μm x 3 μm areas having different degrees of photoinduced reduction of the PL intensity. The photomodification pattern is still clearly visible in the Raman map plotting the intensity of the D peak in the sample after plasma treatment (Fig. 7.1 **(b)**).

Figure 7.1 **(c)** compares the Raman spectra recorded in the pristine and premodified regions of the sample after the plasma treatment. The observed Raman features (an increase of the D peak intensity, and the G and D peaks merging into a

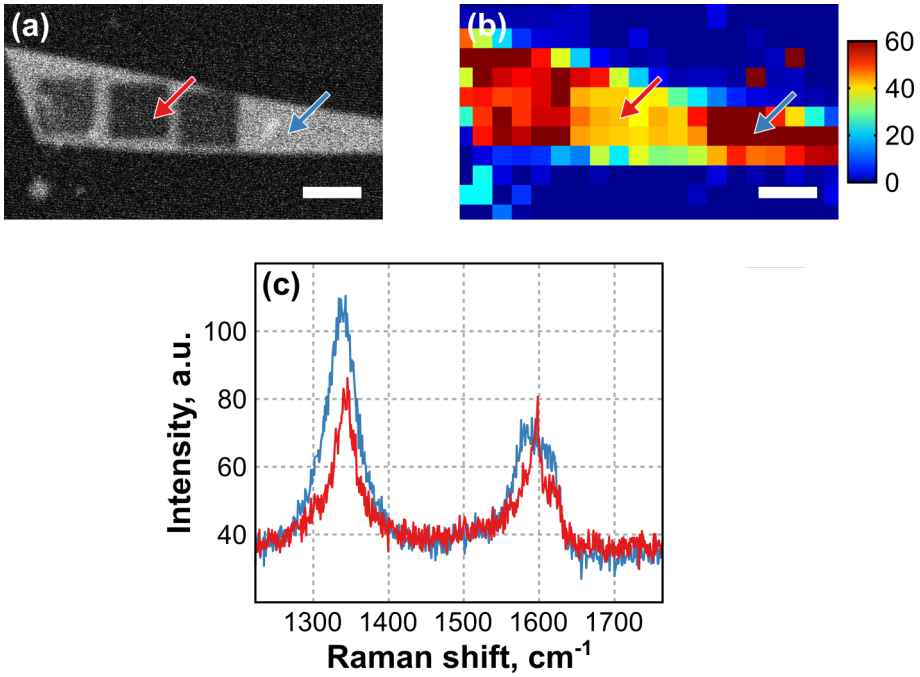

Figure 7.1: **(a)** The PL image of a monolayer graphene sample patterned using photomodification. **(b)** The map of the Raman D peak intensity in the sample after oxygen plasma treatment. **(c)** The Raman spectra collected in the pre-modified **(red)** and pristine **(blue)** areas of the sample after oxidation. The corresponding regions are marked with coloured arrows in the PL and Raman images. All scale bars, 3 μm.

one broad feature) is a typical signature of successful transformation of graphene into graphene oxide [193, 194]. However, the photomodified areas show smaller increase in the D and D' peak intensities, indicating a lower degree of oxidation.

The difference in the Raman spectra between the pristine and photomodified regions of the sample after the plasma treatment indicate that the molecules adsorbed at the graphene surface during photomodification may have acted as a protective layer, shielding graphene from oxygen plasma. These results suggest that photomodification can be used as an additional method for controlling the functionalisation of graphene, capable of creating complex patterns that define the device functionality. However, more in-depth investigations are required to uncover the precise mechanisms at work.

7.2 Optical sensing using photoluminescence imaging

The PL imaging has proven to be a very useful technique for high-resolution, background-free imaging of graphene on various substrates [64, 70]. The newly discovered sensitivity of the PL signal to the charge carrier concentration can transform it into a valuable characterisation technique, allowing the Fermi energy in the samples to be mapped with high resolution and speed. The PL imaging does not require the use of expensive confocal microscopes and can be achieved in a much simpler setup. Using readily available components, an inexpensive inverted microscope was adapted for PL imaging.

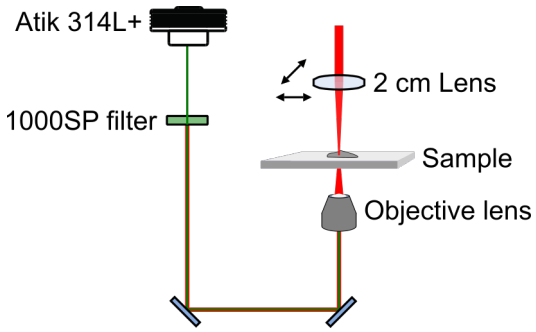

Figure 7.2: Schematic of the custom-built wide-field nonlinear microscope.

Figure 7.2 shows a schematic diagram of the custom build wide-field nonlinear microscope based on a commercial metallurgic microscope (Brunel SP95M). The excitation light is focus onto the sample using a bi-convex lens with a focal length of 2 cm, resulting in a spot size $\sim 10\mu$m. The luminescence signal, transmitted into forward direction and isolated by a 1 μm short-pass filter, is recorded using a consumer astrophotography camera (Atik 315L+). The final PL image is constructed by raster-scanning the excitation spot across the sample and digitally merging the images recorded in different regions into a single picture.

The wide-field nonlinear microscope has been successfully applied for imaging of the samples with electrolyte gate. This type of gating allows the achievement of Fermi level shifts up to 1 eV [119, 175] and is commonly used for optical measurements that require transparent dielectric substrates. However, the ultrafast laser excitation can lead to the melting of the polymer, causing significant damage to the underlying graphene film.

Figure 7.3 **(a)** and **(b)** shows the optical micrographs of graphene samples on the quartz substrates after ultrafast spectroscopic measurements. Due to the thick

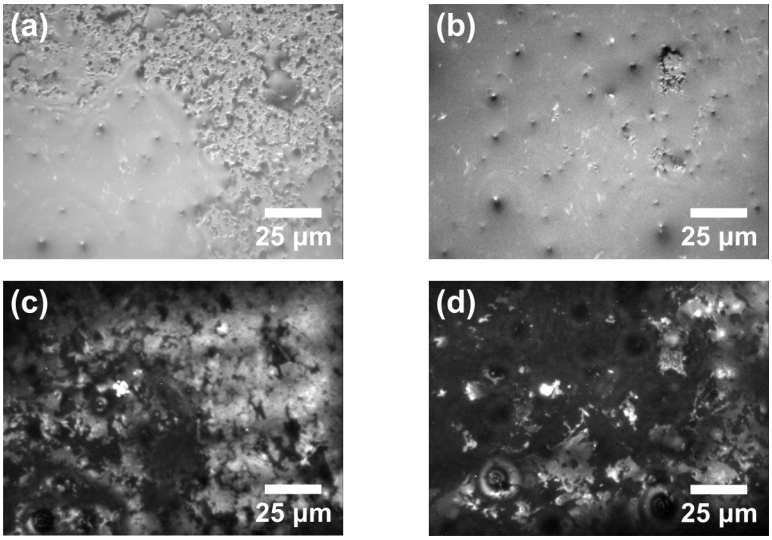

Figure 7.3: **(a)** and **(b)** The optical microscopy images of graphene samples with polymer gate. **(c)** and **(d)** The PL images of the corresponding samples.

layer of polymer covering the samples, the condition of the graphene cannot be investigated using optical microscopy. However, the discontinuities in the graphene film caused by polymer melting are clearly visible in the PL images (**(c)** and **(d)**).

Another possible application of the PL imaging is optical sensing. Due to its intrinsically high surface-to-volume ratio, graphene exhibits strong environmental sensitivity that has led to its application as an active material in a variety of different sensors [73, 76, 77, 80, 82].

This section presents the preliminary results of the PL imaging application for optical sensing of molecules interacting with the surface of graphene. The graphene sample was prepared by CVD growth on a copper foil and transferred onto a quartz substrate using the wet transfer method - see Section 2.2.2 for details. The substrate with the sample was then partly immersed into a pyrene/methanol solution.

Figure 7.4 **(a)** shows the optical microscope image recorded after sample has dried. The dashed lines in the picture indicate the border region between the areas that were immersed (left-hand side) and the pristine graphene (right-hand side). The absence of a sharp border is due to the meniscus formed by methanol. The PL signal produced by the sample shows significantly different intensity in these two regions. Figure 7.4 **(b)** plots the variation of the PL intensity recorded by scanning the excitation spot in the direction perpendicular to the region border. The gradient in the PL intensity is clearly visible, with the PL having significantly higher intensities in the pristine region.

The majority of graphene sensors developed to date rely on the change in the

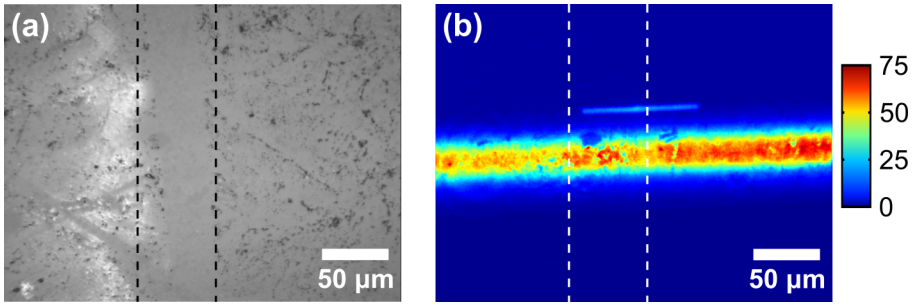

Figure 7.4: **(a)** Optical image of a graphene sample after the immersion into pyrene/methanol solution. The dashed lines mark the border region between the pristine and functionalised areas. **(b)** The PL intensity profile in the corresponding region of the sample. The narrow bright line in the centre is an imaging artefact.

transport characteristic of the sample for detection [196, 197]. The electrochemical detection requires an electric contact to be created with graphene. The use of optical detection may potentially decrease the cost of the sensor components by reducing the number of fabrication steps. This might be especially important for medical applications of graphene, since active component of medical sensors are often disposable. The high resolution of the PL imaging also allows different sensors to be incorporated into a single device by functionalising several areas of graphene with different chemicals.

Glossary

AC Alternating current.

AFM Atomic Force Microscopy.

CNP Charge Neutrality Point.

CVD Chemical Vapor Deposition.

FET Field-Effect transistor.

FWHM Full Width at Half Maximum.

IPA Isopropyl Alcohol.

PL Photoluminescence.

PMMA Polymethyl Methacrylate.

TPD Temporal Photomodification Dynamics.

References

[1] E. Alexeev, J. Moger, and E. Hendry, "Photo-induced doping and strain in exfoliated graphene," *Applied Physics Letters*, vol. 103, no. 15, p. 151907, 2013. 5

[2] K. V. Klitzing, G. Dorda, and M. Pepper, "New method for high-accuracy determination of the fine-structure constant based on quantized hall resistance," *Physical Review Letters*, vol. 45, no. 6, pp. 494–497, 1980. 6

[3] D. C. Tsui, H. L. Stormer, and A. C. Gossard, "Two-Dimensional Magnetotransport in the Extreme Quantum Limit," *Physical Review Letters*, vol. 48, pp. 1559–1562, May 1982. 6

[4] T. Ando, A. B. Fowler, and F. Stern, "Electronic properties of two-dimensional systems," *Reviews of Modern Physics*, vol. 54, p. 437, 1982. 6, 8

[5] J. Heida, B. van Wees, J. Kuipers, T. Klapwijk, and G. Borghs, "Spin-orbit interaction in a two-dimensional electron gas in a InAs/AlSb quantum well with gate-controlled electron density," 1998. 6

[6] A. Rahmani, M. A. Sadeghzadeh, and R. Khordad, "Exploration the quantum and transport lifetimes of electron gas in partially alloyed AlGaAs quantum well," *Superlattices and Microstructures*, vol. 83, pp. 271–281, July 2015. 6

[7] G. Abstreiter, H. Brugger, T. Wolf, H. Jorke, and H. Herzog, "Strain-Induced Two-Dimensional Electron Gas in Selectively Doped Si/Si_{x}Ge_{1-x} Superlattices," *Physical Review Letters*, vol. 54, no. 22, pp. 2441–2444, 1985. 6

[8] L. Landau, E. Lifshitz, and L. E. Reichl, "Statistical physics, part 1," *Physics Today*, vol. 34, no. 1, pp. 74–74, 2008. 6

[9] K. S. Novoselov, a. K. Geim, S. V. Morozov, D. Jiang, Y. Zhang, S. V. Dubonos, I. V. Grigorieva, and a. a. Firsov, "Electric field effect in atomically thin carbon films.," *Science*, vol. 306, pp. 666–9, Oct. 2004. 6, 7, 11, 30, 31

[10] P. Wallace, "The band theory of graphite," *Physical Review*, vol. 329, 1947. 6, 12

[11] a. H. Castro Neto, N. M. R. Peres, K. S. Novoselov, and A. K. Geim, "The electronic properties of graphene," *Reviews of Modern Physics*, vol. 81, pp. 109–162, Jan. 2009. 6, 7, 15

[12] N. M. R. Peres, "Colloquium: The transport properties of graphene: An introduction," *Reviews of Modern Physics*, vol. 82, pp. 2673–2700, Sept. 2010. 6, 15, 37

[13] A. S. Mayorov, R. V. Gorbachev, S. V. Morozov, L. Britnell, R. Jalil, L. A. Ponomarenko, P. Blake, K. S. Novoselov, K. Watanabe, T. Taniguchi, and A. K. Geim, "Micrometer-scale ballistic transport in encapsulated graphene at room temperature.," *Nano letters*, vol. 11, pp. 2396–9, June 2011. 7

[14] S. Morozov, K. Novoselov, M. Katsnelson, F. Schedin, D. Elias, J. Jaszczak, and A. Geim, "Giant Intrinsic Carrier Mobilities in Graphene and Its Bilayer," *Physical Review Letters*, vol. 100, p. 016602, Jan. 2008. 7

[15] K. S. Novoselov, V. I. Falko, L. Colombo, P. R. Gellert, M. G. Schwab, and K. Kim, "A roadmap for graphene," *Nature*, vol. 490, no. 7419, pp. 192–200, 2012. 7

[16] Y.-W. Son, M. L. Cohen, and S. G. Louie, "Half-metallic graphene nanoribbons.," *Nature*, vol. 444, pp. 347–9, Nov. 2006. 7

[17] Y.-W. Son, M. L. Cohen, and S. G. Louie, "Energy Gaps in Graphene Nanoribbons," *Physical Review Letters*, vol. 97, p. 216803, Nov. 2006. 7

[18] X. Li, X. Wang, L. Zhang, S. Lee, and H. Dai, "Chemically derived, ultrasmooth graphene nanoribbon semiconductors.," *Science*, vol. 319, pp. 1229–32, Feb. 2008. 7

[19] M. Han, B. Özyilmaz, Y. Zhang, and P. Kim, "Energy Band-Gap Engineering of Graphene Nanoribbons," *Physical Review Letters*, vol. 98, p. 206805, May 2007. 7

[20] X. Wang, Y. Ouyang, X. Li, H. Wang, J. Guo, and H. Dai, "Room-Temperature All-Semiconducting Sub-10-nm Graphene Nanoribbon Field-Effect Transistors," *Physical Review Letters*, vol. 100, p. 206803, May 2008. 7

[21] S. Ryu, M. Y. Han, J. Maultzsch, T. F. Heinz, P. Kim, M. L. Steigerwald, and L. E. Brus, "Reversible basal plane hydrogenation of graphene.," *Nano letters*, vol. 8, pp. 4597–602, Dec. 2008. 7

[22] D. C. Elias, R. R. Nair, T. M. G. Mohiuddin, S. V. Morozov, P. Blake, M. P. Halsall, A. C. Ferrari, D. W. Boukhvalov, M. I. Katsnelson, A. K. Geim, and K. S. Novoselov, "Control of graphene's properties by reversible hydrogenation: evidence for graphane.," *Science*, vol. 323, pp. 610–3, Jan. 2009. 7, 8

[23] T. Gokus, R. R. Nair, A. Bonetti, M. Böhmler, A. Lombardo, K. S. Novoselov, A. K. Geim, A. C. Ferrari, and A. Hartschuh, "Making graphene luminescent by oxygen plasma treatment.," *ACS nano*, vol. 3, pp. 3963–8, Dec. 2009. 7, 8

[24] Z. Luo, P. M. Vora, E. J. Mele, A. T. C. Johnson, and J. M. Kikkawa, "Photoluminescence and band gap modulation in graphene oxide," *Applied Physics Letters*, vol. 94, p. 111909, Mar. 2009. 7

[25] D. Haberer, D. V. Vyalikh, S. Taioli, B. Dora, M. Farjam, J. Fink, D. Marchenko, T. Pichler, K. Ziegler, S. Simonucci, M. S. Dresselhaus, M. Knupfer, B. Büchner, and A. Grüneis, "Tunable band gap in hydrogenated quasi-free-standing graphene.," *Nano letters*, vol. 10, pp. 3360–6, Sept. 2010. 7

[26] Y. Zhu, S. Murali, W. Cai, X. Li, J. W. Suk, J. R. Potts, and R. S. Ruoff, "Graphene and graphene oxide: synthesis, properties, and applications.," *Advanced materials (Deerfield Beach, Fla.)*, vol. 22, pp. 3906–24, Sept. 2010. 7, 102

[27] Y. Zhang, T.-T. Tang, C. Girit, Z. Hao, M. C. Martin, A. Zettl, M. F. Crommie, Y. R. Shen, and F. Wang, "Direct observation of a widely tunable bandgap in bilayer graphene.," *Nature*, vol. 459, pp. 820–3, June 2009. 7

[28] F. Xia, D. B. Farmer, Y.-M. Lin, and P. Avouris, "Graphene field-effect transistors with high on/off current ratio and large transport band gap at room temperature.," *Nano letters*, vol. 10, pp. 715–8, Feb. 2010. 7

[29] K. F. Mak, C. H. Lui, J. Shan, and T. F. Heinz, "Observation of an Electric-Field-Induced Band Gap in Bilayer Graphene by Infrared Spectroscopy," *Physical Review Letters*, vol. 102, p. 256405, June 2009. 7

[30] F. Schwierz, "Graphene transistors.," *Nature nanotechnology*, vol. 5, pp. 487–96, July 2010. 7

[31] C. Lee, X. Wei, J. W. Kysar, and J. Hone, "Measurement of the Elastic Properties and Intrinsic Strength of Monolayer Graphene," *Science*, vol. 321, no. July, pp. 385–388, 2008. 7

[32] R. R. Nair, P. Blake, a. N. Grigorenko, K. S. Novoselov, T. J. Booth, T. Stauber, N. M. R. Peres, and a. K. Geim, "Fine structure constant defines visual transparency of graphene.," *Science*, vol. 320, no. 5881, p. 1308, 2008. 7, 16, 33

[33] Z. Q. Li, E. A. Henriksen, Z. Jiang, Z. Hao, M. C. Martin, P. Kim, H. L. Stormer, and D. N. Basov, "Dirac charge dynamics in graphene by infrared spectroscopy," *Nature Physics*, vol. 4, pp. 532–535, June 2008. 7

[34] Z. Sun, T. Hasan, F. Torrisi, D. Popa, G. Privitera, F. Wang, F. Bonaccorso, D. M. Basko, and A. C. Ferrari, "Graphene mode-locked ultrafast laser.," *ACS nano*, vol. 4, pp. 803–10, Feb. 2010. 7

[35] A. Kuzmenko, E. van Heumen, F. Carbone, and D. van der Marel, "Universal Optical Conductance of Graphite," *Physical Review Letters*, vol. 100, p. 117401, Mar. 2008. 7

[36] E. Hendry, P. J. Hale, J. Moger, a. K. Savchenko, and S. a. Mikhailov, "Coherent Nonlinear Optical Response of Graphene," *Physical Review Letters*, vol. 105, p. 097401, Aug. 2010. 7, 45

[37] S. Mikhailov, "Theory of the nonlinear optical frequency mixing effect in graphene," *Physica E: Low-dimensional Systems and Nanostructures*, vol. 44, pp. 924–927, Mar. 2012. 7

[38] M. Liu, X. Yin, E. Ulin-Avila, B. Geng, T. Zentgraf, L. Ju, F. Wang, and X. Zhang, "A graphene-based broadband optical modulator.," *Nature*, vol. 474, pp. 64–67, 2011. 7

[39] E. O. Polat and C. Kocabas, "Broadband optical modulators based on graphene supercapacitors.," *Nano letters*, vol. 13, pp. 5851–7, 2013. 7

[40] W. Li, B. Chen, C. Meng, W. Fang, Y. Xiao, X. Li, Z. Hu, Y. Xu, L. Tong, H. Wang, W. Liu, J. Bao, and Y. R. Shen, "Ultrafast all-optical graphene modulator.," *Nano letters*, vol. 14, pp. 955–9, 2014. 7

[41] F. Xia, T. Mueller, Y.-M. Lin, A. Valdes-Garcia, and P. Avouris, "Ultrafast graphene photodetector.," *Nature nanotechnology*, vol. 4, pp. 839–43, Dec. 2009. 7

[42] T. Mueller, F. Xia, and P. Avouris, "Graphene photodetectors for high-speed optical communications," *Nature Photonics*, vol. 4, no. March, pp. 297–301, 2010. 7

[43] A. Urich, K. Unterrainer, and T. Mueller, "Intrinsic response time of graphene photodetectors.," *Nano letters*, vol. 11, pp. 2804–8, July 2011. 7

[44] Q. Bao, H. Zhang, Y. Wang, Z. Ni, Y. Yan, Z. X. Shen, K. P. Loh, and D. Y. Tang, "Atomic-Layer Graphene as a Saturable Absorber for Ultrafast Pulsed Lasers," *Advanced Functional Materials*, vol. 19, pp. 3077–3083, Oct. 2009. 7

[45] J.-L. Xu, X.-L. Li, Y.-Z. Wu, X.-P. Hao, J.-L. He, and K.-J. Yang, "Graphene saturable absorber mirror for ultra-fast-pulse solid-state laser.," *Optics letters*, vol. 36, pp. 1948–50, May 2011. 7

[46] J. Dean and H. van Driel, "Graphene and few-layer graphite probed by second-harmonic generation: Theory and experiment," *Physical Review B*, 2010. 7

[47] K. S. Kim, Y. Zhao, H. Jang, S. Y. Lee, J. M. Kim, K. S. Kim, J.-H. Ahn, P. Kim, J.-Y. Choi, and B. H. Hong, "Large-scale pattern growth of graphene films for stretchable transparent electrodes.," *Nature*, vol. 457, pp. 706–710, 2009. 7

[48] S. Bae, H. Kim, Y. Lee, X. Xu, J.-S. Park, Y. Zheng, J. Balakrishnan, T. Lei, H. R. Kim, Y. I. Song, Y.-J. Kim, K. S. Kim, B. Ozyilmaz, J.-H. Ahn, B. H. Hong, and S. Iijima, "Roll-to-roll production of 30-inch graphene films for transparent electrodes.," *Nature nanotechnology*, vol. 5, pp. 574–578, 2010. 7

[49] I. Khrapach, F. Withers, T. H. Bointon, D. K. Polyushkin, W. L. Barnes, S. Russo, and M. F. Craciun, "Novel highly conductive and transparent graphene-based conductors.," *Advanced materials (Deerfield Beach, Fla.)*, vol. 24, pp. 2844–9, 2012. 7, 8

[50] D. Brida, A. Tomadin, C. Manzoni, Y. J. Kim, A. Lombardo, S. Milana, R. R. Nair, K. S. Novoselov, a. C. Ferrari, G. Cerullo, and M. Polini, "Ultrafast collinear scattering and carrier multiplication in graphene.," *Nature communications*, vol. 4, p. 1987, Jan. 2013. 7, 8, 26, 58

[51] K. M. Dani, J. Lee, R. Sharma, a. D. Mohite, C. M. Galande, P. M. Ajayan, a. M. Dattelbaum, H. Htoon, a. J. Taylor, and R. P. Prasankumar, "Intraband conductivity response in graphene observed using ultrafast infrared-pump visible-probe spectroscopy," *Physical Review B*, vol. 86, p. 125403, Sept. 2012. 7

[52] J. M. Dawlaty, S. Shivaraman, M. Chandrashekhar, F. Rana, and M. G. Spencer, "Measurement of ultrafast carrier dynamics in epitaxial graphene," *Applied Physics Letters*, vol. 92, no. 4, p. 042116, 2008. 7, 8, 58, 96, 97

[53] P. George, J. Strait, and J. Dawlaty, "Ultrafast optical-pump terahertz-probe spectroscopy of the carrier relaxation and recombination dynamics in epitaxial graphene," *Nano . . .*, pp. 17–20, 2008. 7

[54] P. J. Hale, S. M. Hornett, J. Moger, D. W. Horsell, and E. Hendry, "Hot phonon decay in supported and suspended exfoliated graphene," *Physical Review B*, vol. 83, p. 121404, Mar. 2011. 7, 8, 26, 27, 28, 45, 58, 96, 97

[55] L. M. Malard, K. Fai Mak, a. H. Castro Neto, N. M. R. Peres, and T. F. Heinz, "Observation of intra- and inter-band transitions in the transient optical response of graphene," *New Journal of Physics*, vol. 15, p. 015009, Jan. 2013. 7

[56] R. W. Newson, J. Dean, B. Schmidt, and H. M. van Driel, "Ultrafast carrier kinetics in exfoliated graphene and thin graphite films.," *Optics express*, vol. 17, pp. 2326–33, Feb. 2009. 7

[57] H. Wang, J. H. Strait, P. a. George, S. Shivaraman, V. B. Shields, M. Chandrashekhar, J. Hwang, F. Rana, M. G. Spencer, C. S. Ruiz-Vargas, and J. Park, "Ultrafast relaxation dynamics of hot optical phonons in graphene," *Applied Physics Letters*, vol. 96, no. 8, p. 081917, 2010. 7, 8, 26, 27, 45, 87, 96

[58] I. Gierz, M. Mitrano, H. Bromberger, C. Cacho, R. Chapman, E. Springate, S. Link, U. Starke, B. Sachs, M. Eckstein, T. O. Wehling, M. I. Katsnelson, A. Lichtenstein, and A. Cavalleri, "Phonon-Pump Extreme-Ultraviolet-Photoemission Probe in Graphene : Anomalous Heating of Dirac Carriers by Lattice Deformation," *Physical Review Letters*, vol. 114, p. 125503, Mar. 2015. 7

[59] S. Gilbertson, G. L. Dakovski, T. Durakiewicz, J.-X. Zhu, K. M. Dani, A. D. Mohite, A. Dattelbaum, and G. Rodriguez, "Tracing Ultrafast Separation and Coalescence of Carrier Distributions in Graphene with Time-Resolved Photoemission," *The Journal of Physical Chemistry Letters*, vol. 3, pp. 64–68, Jan. 2012. 7, 45

[60] J. C. Johannsen, S. r. Ulstrup, F. Cilento, A. Crepaldi, M. Zacchigna, C. Cacho, I. C. E. Turcu, E. Springate, F. Fromm, C. Raidel, T. Seyller, F. Parmigiani, M. Grioni, and P. Hofmann, "Direct View of Hot Carrier Dynamics in Graphene," *Physical Review Letters*, vol. 111, p. 027403, July 2013. 7, 45

[61] S. r. Ulstrup, J. Christian Johannsen, A. Crepaldi, F. Cilento, M. Zacchigna, C. Cacho, R. T. Chapman, E. Springate, F. Fromm, C. Raidel, T. Seyller, F. Parmigiani, M. Grioni, and P. Hofmann, "Ultrafast electron dynamics in epitaxial graphene investigated with time- and angle-resolved photoemission spectroscopy," *Journal of Physics: Condensed Matter*, vol. 27, no. 16, p. 164206, 2015. 7

[62] J. C. Johannsen, S. r. Ulstrup, F. Cilento, A. Crepaldi, M. Zacchigna, C. Cacho, I. C. Edmond, E. Springate, F. Fromm, and C. Raidel, "Direct view on the ultrafast carrier dynamics in graphene," *Physical Review Letters*, pp. 1–15, 2013. 8, 58, 96

[63] E. Hwang, B. Y.-K. Hu, and S. Das Sarma, "Inelastic carrier lifetime in graphene," *Physical Review B*, vol. 76, p. 115434, Sept. 2007. 8, 26, 29, 58, 87, 97

[64] R. J. Stöhr, R. Kolesov, J. Pflaum, and J. Wrachtrup, "Fluorescence of laser-created electron-hole plasma in graphene," *Physical Review B*, vol. 82, p. 121408, Sept. 2010. 8, 25, 26, 27, 53, 104

[65] C.-T. Chien, S.-S. Li, W.-J. Lai, Y.-C. Yeh, H.-A. Chen, I.-S. Chen, L.-C. Chen, K.-H. Chen, T. Nemoto, S. Isoda, M. Chen, T. Fujita, G. Eda, H. Yamaguchi, M. Chhowalla, and C.-W. Chen, "Tunable photoluminescence from

graphene oxide.," *Angewandte Chemie (International ed. in English)*, vol. 51, pp. 6662–6, July 2012. 8

[66] G. Eda, Y.-Y. Lin, C. Mattevi, H. Yamaguchi, H.-A. Chen, I.-S. Chen, C.-W. Chen, and M. Chhowalla, "Blue photoluminescence from chemically derived graphene oxide.," *Advanced materials (Deerfield Beach, Fla.)*, vol. 22, pp. 505–9, Jan. 2010. 8

[67] K. P. Loh, Q. Bao, G. Eda, and M. Chhowalla, "Graphene oxide as a chemically tunable platform for optical applications.," *Nature chemistry*, vol. 2, pp. 1015–24, Dec. 2010. 8

[68] C.-F. Chen, C.-H. Park, B. W. Boudouris, J. Horng, B. Geng, C. Girit, A. Zettl, M. F. Crommie, R. a. Segalman, S. G. Louie, and F. Wang, "Controlling inelastic light scattering quantum pathways in graphene.," *Nature*, vol. 471, pp. 617–20, Mar. 2011. 8, 25

[69] T. Winzer, R. Ciesielski, M. Handloser, A. Comin, A. Hartschuh, and E. Malic, "Microscopic View on the Ultrafast Photoluminescence from Photoexcited Graphene," *Nano letters*, vol. 15, pp. 1141–5, Feb. 2015. 8

[70] W.-T. T. Liu, S. W. Wu, P. J. Schuck, M. Salmeron, Y. R. Shen, and F. Wang, "Nonlinear broadband photoluminescence of graphene induced by femtosecond laser irradiation," *Physical Review B - Condensed Matter and Materials Physics*, vol. 82, p. 081408, Aug. 2010. 8, 25, 104

[71] C. H. Lui, K. F. Mak, J. Shan, and T. F. Heinz, "Ultrafast Photoluminescence from Graphene," *Physical Review Letters*, vol. 105, p. 127404, Sept. 2010. 8, 25, 26, 27, 29, 54, 91, 92, 93, 96

[72] T. Koyama, Y. Ito, K. Yoshida, M. Tsuji, H. Ago, H. Kishida, and A. Nakamura, "Near-Infrared Photoluminescence in the Femtosecond Time Region in Monolayer Graphene on SiO2," *ACS ...*, vol. 7, no. 3, pp. 2335–2343, 2013. 8, 27

[73] M. Pumera, A. Ambrosi, A. Bonanni, E. L. K. Chng, and H. L. Poh, "Graphene for electrochemical sensing and biosensing," *TrAC Trends in Analytical Chemistry*, vol. 29, pp. 954–965, Oct. 2010. 8, 105

[74] C. Lu, H. Yang, C. Zhu, X. Chen, and G. Chen, "A Graphene Platform for Sensing Biomolecules," *Angewandte Chemie*, vol. 121, pp. 4879–4881, June 2009. 8

[75] X. Kang, J. Wang, H. Wu, J. Liu, I. A. Aksay, and Y. Lin, "A graphene-based electrochemical sensor for sensitive detection of paracetamol.," *Talanta*, vol. 81, pp. 754–9, May 2010. 8

[76] P. K. Ang, W. Chen, A. T. S. Wee, and K. P. Loh, "Solution-gated epitaxial graphene as pH sensor.," *Journal of the American Chemical Society*, vol. 130, pp. 14392–3, Nov. 2008. 8, 105

[77] C. W. Chen, S. C. Hung, M. D. Yang, C. W. Yeh, C. H. Wu, G. C. Chi, F. Ren, and S. J. Pearton, "Oxygen sensors made by monolayer graphene under room temperature," *Applied Physics Letters*, vol. 99, p. 243502, Dec. 2011. 8, 105

[78] W. Wu, Z. Liu, L. A. Jauregui, Q. Yu, R. Pillai, H. Cao, J. Bao, Y. P. Chen, and S.-S. S. Pei, "Wafer-scale synthesis of graphene by chemical vapor deposition and its application in hydrogen sensing," *Sensors and Actuators, B: Chemical*, vol. 150, pp. 296–300, Sept. 2010. 8

[79] M. G. Chung, D. H. Kim, H. M. Lee, T. Kim, J. H. Choi, D. kyun Seo, J.-B. Yoo, S.-H. Hong, T. J. Kang, and Y. H. Kim, "Highly sensitive NO2 gas sensor based on ozone treated graphene," *Sensors and Actuators B: Chemical*, vol. 166-167, pp. 172–176, May 2012. 8

[80] B. Zhang and T. Cui, "An ultrasensitive and low-cost graphene sensor based on layer-by-layer nano self-assembly," *Applied Physics Letters*, vol. 98, p. 073116, Feb. 2011. 8, 105

[81] W. Li, X. Geng, Y. Guo, J. Rong, Y. Gong, L. Wu, X. Zhang, P. Li, J. Xu, G. Cheng, M. Sun, and L. Liu, "Reduced graphene oxide electrically contacted graphene sensor for highly sensitive nitric oxide detection.," *ACS Nano*, vol. 5, pp. 6955–61, Sept. 2011. 8

[82] H. J. Yoon, D. H. Jun, J. H. Yang, Z. Zhou, S. S. Yang, and M. M.-C. C. Cheng, "Carbon dioxide gas sensor using a graphene sheet," *Sensors and Actuators, B: Chemical*, vol. 157, pp. 310–313, Sept. 2011. 8, 105

[83] W. H. Lee, J. W. Suk, H. Chou, J. Lee, Y. Hao, Y. Wu, R. Piner, D. Akinwande, K. S. Kim, and R. S. Ruoff, "Selective-area fluorination of graphene with fluoropolymer and laser irradiation," *Nano Letters*, vol. 12, no. 5, pp. 2374–2378, 2012. 8, 68

[84] F. Withers, M. Dubois, and A. K. Savchenko, "Electron properties of fluorinated single-layer graphene transistors," *Physical Review B*, vol. 82, p. 073403, Aug. 2010. 8

[85] D. Zhan, L. Sun, Z. H. Ni, L. Liu, X. F. Fan, Y. Wang, T. Yu, Y. M. Lam, W. Huang, and Z. X. Shen, "FeCl3-Based Few-Layer Graphene Intercalation Compounds: Single Linear Dispersion Electronic Band Structure and Strong Charge Transfer Doping," *Advanced Functional Materials*, vol. 20, pp. 3504–3509, Oct. 2010. 8

[86] K. P. Loh, Q. Bao, P. K. Ang, and J. Yang, "The chemistry of graphene," *Journal of Materials Chemistry*, vol. 20, p. 2277, Mar. 2010. 8

[87] M. F. Craciun, I. Khrapach, M. D. Barnes, and S. Russo, "Properties and applications of chemically functionalized graphene.," *Journal of physics. Condensed matter : an Institute of Physics journal*, vol. 25, p. 423201, Oct. 2013. 8

[88] S. Ryu, L. Liu, S. Berciaud, Y.-J. Yu, H. Liu, P. Kim, G. W. Flynn, and L. E. Brus, "Atmospheric Oxygen Binding and Hole Doping in Deformed Graphene on a SiO(2) Substrate.," *Nano letters*, pp. 4944–4951, Nov. 2010. 9, 52, 63, 67, 72, 101

[89] Q. H. Wang, K. Kalantar-Zadeh, A. Kis, J. N. Coleman, and M. S. Strano, "Electronics and optoelectronics of two-dimensional transition metal dichalcogenides.," *Nature nanotechnology*, vol. 7, no. 11, pp. 699–712, 2012. 9

[90] J. E. Lee, G. Ahn, J. Shim, Y. S. Lee, and S. Ryu, "Optical separation of mechanical strain from charge doping in graphene," *Nature Communications*, vol. 3, p. 1024, Jan. 2012. 9, 23, 63, 66, 67, 68, 72, 101

[91] H. Wang, Y. Wu, C. Cong, J. Shang, and T. Yu, "Hysteresis of electronic transport in graphene transistors," *ACS Nano*, vol. 4, no. 12, pp. 7221–7228, 2010. 9, 79, 81

[92] P. Joshi, H. E. Romero, a. T. Neal, V. K. Toutam, and S. a. Tadigadapa, "Intrinsic doping and gate hysteresis in graphene field effect devices fabricated on SiO2 substrates.," *Journal of physics. Condensed matter : an Institute of Physics journal*, vol. 22, no. 33, p. 334214, 2010. 9

[93] H. Xu, Y. Chen, J. Zhang, and H. Zhang, "Investigating the mechanism of hysteresis effect in graphene electrical field device fabricated on SiO substrates using Raman spectroscopy.," *Small (Weinheim an der Bergstrasse, Germany)*, vol. 8, pp. 2833–40, Sept. 2012. 9

[94] Y. Yang and R. Murali, "Binding mechanisms of molecular oxygen and moisture to graphene," *Applied Physics Letters*, vol. 98, no. 9, pp. 2011–2014, 2011. 9, 53, 67, 79

[95] A. Tiberj, M. Paillet, P. Landois, M. Mikolasek, S. Contreras, E. Dujardin, L. Charles, M. Rubio-Roy, J.-R. Huntzinger, J.-L. Sauvajol, and A.-a. Zahab, "Reversible optical doping of graphene.," *Scientific reports*, vol. 3, p. 2355, Jan. 2013. 9, 52

[96] X.-J. Wang, L. Zou, D. Li, Q. Zhang, F. Wang, and Z. Zhang, "Photo-Induced Doping in Graphene/Silicon Heterostructures," *The Journal of Physical Chemistry C*, vol. 119, pp. 1061–1066, Jan. 2015. 9

[97] N. Papasimakis, S. Mailis, C. C. Huang, F. Al-Saab, D. W. Hewak, Z. Luo, and Z. X. Shen, "Strain engineering in graphene by laser irradiation," *Applied Physics Letters*, vol. 106, p. 061904, Feb. 2015. 9

[98] Z. Luo, N. J. Pinto, Y. Davila, and a. T. Charlie Johnson, "Controlled doping of graphene using ultraviolet irradiation," *Applied Physics Letters*, vol. 100, no. 25, p. 253108, 2012. 9, 52

[99] A. Berholts, T. Kahro, A. Floren, H. Alles, and R. Jaaniso, "Photo-activated oxygen sensitivity of graphene at room temperature," *Applied Physics Letters*, vol. 105, no. 16, p. 163111, 2014. 9

[100] M. Lenner, A. Kaplan, C. Huchon, and R. E. Palmer, "Ultrafast laser ablation of graphite," *Physical Review B*, vol. 79, p. 184105, May 2009. 9

[101] M. Currie, J. D. Caldwell, F. J. Bezares, J. Robinson, T. Anderson, H. Chun, and M. Tadjer, "Quantifying pulsed laser induced damage to graphene," *Applied Physics Letters*, vol. 99, no. 21, p. 211909, 2011. 9, 45

[102] J.-H. Yoo, J. Bin In, J. Bok Park, H. Jeon, and C. P. Grigoropoulos, "Graphene folds by femtosecond laser ablation," *Applied Physics Letters*, vol. 100, no. 23, p. 233124, 2012. 9

[103] W. Zhang, L. Li, Z. B. Wang, a. a. Pena, D. J. Whitehead, M. L. Zhong, Z. Lin, and H. W. Zhu, "Ti:sapphire femtosecond laser direct micro-cutting and profiling of graphene," *Applied Physics A*, vol. 109, pp. 291–297, July 2012. 9

[104] P. E. Gaskell, H. S. Skulason, C. Rodenchuk, and T. Szkopek, "Counting graphene layers on glass via optical reflection microscopy," *Applied Physics Letters*, vol. 94, no. 14, p. 143101, 2009. 17, 33, 34, 46, 64

[105] L. Malard, M. Pimenta, G. Dresselhaus, and M. Dresselhaus, "Raman spectroscopy in graphene," *Physics Reports*, vol. 473, pp. 51–87, Apr. 2009. 18, 19, 20, 21, 66, 68

[106] D. M. Basko, S. Piscanec, and a. C. Ferrari, "Electron-electron interactions and doping dependence of the two-phonon Raman intensity in graphene," *Physical Review B*, vol. 80, p. 165413, Oct. 2009. 18, 25, 74, 75

[107] M. Matthews, M. Pimenta, G. Dresselhaus, M. Dresselhaus, and M. Endo, "Origin of dispersive effects of the Raman D band in carbon materials," *Physical Review B*, vol. 59, no. 10, pp. R6585–R6588, 1999. 20

[108] A. C. Ferrari and D. M. Basko, "Raman spectroscopy as a versatile tool for studying the properties of graphene.," *Nature nanotechnology*, vol. 8, pp. 235–46, Apr. 2013. 21, 22, 25, 66, 74, 75

[109] B. Krauss, T. Lohmann, D.-H. Chae, M. Haluska, K. von Klitzing, and J. Smet, "Laser-induced disassembly of a graphene single crystal into a nanocrystalline network," *Physical Review B*, vol. 79, p. 165428, Apr. 2009. 21, 22, 58

[110] L. G. Cançado, A. Jorio, E. H. M. Ferreira, F. Stavale, C. a. Achete, R. B. Capaz, M. V. O. Moutinho, A. Lombardo, T. S. Kulmala, and a. C. Ferrari, "Quantifying defects in graphene via Raman spectroscopy at different excitation energies.," *Nano letters*, vol. 11, pp. 3190–6, Aug. 2011. 22, 49

[111] M. Huang, H. Yan, C. Chen, D. Song, T. F. Heinz, and J. Hone, "Phonon softening and crystallographic orientation of strained graphene studied by Raman spectroscopy.," *Proceedings of the National Academy of Sciences of the United States of America*, vol. 106, pp. 7304–8, May 2009. 22, 23, 66

[112] O. Frank, G. Tsoukleri, J. Parthenios, K. Papagelis, I. Riaz, R. Jalil, K. S. Novoselov, and C. Galiotis, "Compression behavior of single-layer graphenes.," *ACS nano*, vol. 4, pp. 3131–8, June 2010. 23

[113] O. Frank, M. Mohr, J. Maultzsch, C. Thomsen, I. Riaz, R. Jalil, K. S. Novoselov, G. Tsoukleri, J. Parthenios, K. Papagelis, L. Kavan, and C. Galiotis, "Raman 2D-band splitting in graphene: theory and experiment.," *ACS nano*, vol. 5, pp. 2231–9, Mar. 2011. 23

[114] M. Huang, H. Yan, T. F. Heinz, and J. Hone, "Probing strain-induced electronic structure change in graphene by Raman spectroscopy," *Nano Letters*, vol. 10, no. 10, pp. 4074–4079, 2010. 23

[115] F. Ding, H. Ji, Y. Chen, A. Herklotz, K. Dörr, Y. Mei, A. Rastelli, and O. G. Schmidt, "Stretchable graphene: A close look at fundamental parameters through biaxial straining," *Nano Letters*, vol. 10, pp. 3453–3458, 2010. 23, 66

[116] C. Metzger, S. Rémi, M. Liu, S. V. Kusminskiy, A. H. Castro Neto, A. K. Swan, and B. B. Goldberg, "Biaxial strain in graphene adhered to shallow depressions," *Nano Letters*, vol. 10, pp. 6–10, 2010. 23, 66

[117] J. Zabel, R. R. Nair, A. Ott, T. Georgiou, A. K. Geim, K. S. Novoselov, and C. Casiraghi, "Raman spectroscopy of graphene and bilayer under biaxial strain: bubbles and balloons.," *Nano letters*, vol. 12, pp. 617–21, Feb. 2012. 23, 66

[118] D. Yoon, Y. W. Son, and H. Cheong, "Strain-dependent splitting of the double-resonance raman scattering band in graphene," *Physical Review Letters*, vol. 106, no. 15, pp. 1–4, 2011. 23, 66

[119] A. Das, S. Pisana, B. Chakraborty, S. Piscanec, S. K. Saha, U. V. Waghmare, K. S. Novoselov, H. R. Krishnamurthy, a. K. Geim, a. C. Ferrari, and a. K. Sood, "Monitoring dopants by Raman scattering in an electrochemically top-gated graphene transistor.," *Nature nanotechnology*, vol. 3, pp. 210–5, Apr. 2008. 24, 65, 66, 70, 104

[120] S. Pisana, M. Lazzeri, C. Casiraghi, K. S. Novoselov, a. K. Geim, A. C. Ferrari, and F. Mauri, "Breakdown of the adiabatic Born-Oppenheimer approximation in graphene.," *Nature materials*, vol. 6, pp. 198–201, Mar. 2007. 24, 66

[121] Q. Chen, C. Zhang, F. Xue, Y. Zhou, W. Li, Y. Wang, W. Tu, Z. Zou, X. Wang, and M. Xiao, "Enhanced hot-carrier luminescence in multilayer reduced graphene oxide nanospheres.," *Scientific reports*, vol. 3, p. 2315, Jan. 2013. 25

[122] M. Handlosera, G. Pireddaa, A. Lombardob, A. C. Ferrarih, A. Hartschuha, M. Handloser, G. Piredda, M. Handlosera, G. Pireddaa, A. Lombardob, A. C. Ferrarih, A. Hartschuha, M. Handloser, and G. Piredda, "Non-linear photoluminescence from graphene," *... on Lasers and ...*, vol. 127404, no. 2010, p. 127404, 2011. 25

[123] W.-K. Tse, E. H. Hwang, and S. Das Sarma, "Ballistic hot electron transport in graphene," *Applied Physics Letters*, vol. 93, no. 2, p. 023128, 2008. 26, 29, 87

[124] S. Stankovich, D. A. Dikin, R. D. Piner, K. A. Kohlhaas, A. Kleinhammes, Y. Jia, Y. Wu, S. T. Nguyen, and R. S. Ruoff, "Synthesis of graphene-based nanosheets via chemical reduction of exfoliated graphite oxide," *Carbon*, vol. 45, pp. 1558–1565, June 2007. 30

[125] Y. Hernandez, V. Nicolosi, M. Lotya, F. M. Blighe, Z. Sun, S. De, I. T. McGovern, B. Holland, M. Byrne, Y. K. Gun'Ko, J. J. Boland, P. Niraj, G. Duesberg, S. Krishnamurthy, R. Goodhue, J. Hutchison, V. Scardaci, A. C. Ferrari, and J. N. Coleman, "High-yield production of graphene by liquid-phase exfoliation of graphite.," *Nature nanotechnology*, vol. 3, pp. 563–8, Sept. 2008. 30

[126] K. R. Paton, E. Varrla, C. Backes, R. J. Smith, U. Khan, A. O'Neill, C. Boland, M. Lotya, O. M. Istrate, P. King, T. Higgins, S. Barwich, P. May, P. Puczkarski, I. Ahmed, M. Moebius, H. Pettersson, E. Long, J. a. Coelho, S. E. O'Brien, E. K. McGuire, B. M. Sanchez, G. S. Duesberg, N. McEvoy, T. J. Pennycook, C. Downing, A. Crossley, V. Nicolosi, and J. N. Coleman, "Scalable production of large quantities of defect-free few-layer graphene by shear exfoliation in liquids.," *Nature materials*, vol. 13, pp. 624–30, June 2014. 30

[127] K. V. Emtsev, A. Bostwick, K. Horn, J. Jobst, G. L. Kellogg, L. Ley, J. L. McChesney, T. Ohta, S. A. Reshanov, J. Röhrl, E. Rotenberg, A. K. Schmid, D. Waldmann, H. B. Weber, and T. Seyller, "Towards wafer-size graphene

layers by atmospheric pressure graphitization of silicon carbide.," *Nature materials*, vol. 8, pp. 203–7, Mar. 2009. 30

[128] K. S. Kim, Y. Zhao, H. Jang, S. Y. Lee, J. M. Kim, K. S. Kim, J.-H. Ahn, P. Kim, J.-Y. Choi, and B. H. Hong, "Large-scale pattern growth of graphene films for stretchable transparent electrodes.," *Nature*, vol. 457, pp. 706–10, Feb. 2009. 30

[129] P. Sutter, "Epitaxial graphene: How silicon leaves the scene.," *Nature materials*, vol. 8, pp. 171–2, Mar. 2009. 30

[130] a. K. Geim and K. S. Novoselov, "The rise of graphene.," *Nature materials*, vol. 6, pp. 183–91, Mar. 2007. 30

[131] K. S. Novoselov, "Nobel Lecture: Graphene: Materials in the Flatland," *Reviews of Modern Physics*, vol. 83, pp. 837–849, Aug. 2011. 30

[132] X. Li, W. Cai, J. An, S. Kim, J. Nah, D. Yang, R. Piner, A. Velamakanni, I. Jung, E. Tutuc, S. K. Banerjee, L. Colombo, and R. S. Ruoff, "Large-area synthesis of high-quality and uniform graphene films on copper foils.," *Science*, vol. 324, pp. 1312–1314, 2009. 30, 32

[133] A. Reina, X. Jia, J. Ho, D. Nezich, H. Son, V. Bulovic, M. S. Dresselhaus, and J. Kong, "Large area, few-layer graphene films on arbitrary substrates by chemical vapor deposition.," *Nano letters*, vol. 9, pp. 30–5, Jan. 2009. 30

[134] X. Li, C. W. Magnuson, A. Venugopal, R. M. Tromp, J. B. Hannon, E. M. Vogel, L. Colombo, and R. S. Ruoff, "Large-area graphene single crystals grown by low-pressure chemical vapor deposition of methane on copper.," *Journal of the American Chemical Society*, vol. 133, pp. 2816–9, Mar. 2011. 30

[135] P. Eaton and P. West, *Atomic force microscopy*. Oxford University Press, 2010. 38, 73

[136] R. G. W. Norrish and G. Porter, "Chemical reactions produced by very high light intensities.," 1949. 39

[137] H. W. Mocker and R. J. Collins, "Mode competition and self-locking effects in a q-switched ruby laser," *Applied Physics Letters*, vol. 7, no. 10, 1965. 39

[138] A. J. DeMaria, D. A. Stetser, and H. Heynau, "Self mode-locking of lasers with saturable absorbers," *Applied Physics Letters*, vol. 8, p. 174, Nov. 1966. 39

[139] J. Coates, "Encyclopedia of Analytical Chemistry," *Encyclopedia of analytical chemistry*, pp. 10815–10837, 2006. 39

[140] R. L. Fork, B. I. Greene, and C. V. Shank, "Generation of optical pulses shorter than 0.1 psec by colliding pulse mode locking," *Applied Physics Letters*, vol. 38, no. 1981, pp. 671–672, 1981. 39

[141] K. Zhao, Q. Zhang, M. Chini, Y. Wu, X. Wang, and Z. Chang, "Tailoring a 67 attosecond pulse through advantageous," *Optics Letters*, vol. 37, no. 18, pp. 3891–3893, 2012. 39

[142] C. J. Docherty, C.-T. Lin, H. J. Joyce, R. J. Nicholas, L. M. Herz, L.-J. Li, and M. B. Johnston, "Extreme sensitivity of graphene photoconductivity to environmental gases.," *Nature communications*, vol. 3, p. 1228, 2012. 45, 52

[143] A. C. Ferrari, J. C. Meyer, V. Scardaci, C. Casiraghi, M. Lazzeri, F. Mauri, S. Piscanec, D. Jiang, K. S. Novoselov, S. Roth, and a. K. Geim, "Raman Spectrum of Graphene and Graphene Layers," *Physical Review Letters*, vol. 97, p. 187401, Oct. 2006. 46, 64

[144] L. Kong, A. Enders, T. S. Rahman, and P. a. Dowben, "Molecular adsorption on graphene.," *Journal of physics. Condensed matter : an Institute of Physics journal*, vol. 443001, 2014. 52, 67

[145] R. Stohr, R. Kolesov, K. Xia, and J. Wrachtrup, "All-Optical High-Resolution Nanopatterning and 3D Suspending of Graphene," *ACS nano*, no. 6, pp. 5141–5150, 2011. 58

[146] F. Hao, D. Fang, and Z. Xu, "Mechanical and thermal transport properties of graphene with defects," *Applied Physics Letters*, vol. 99, no. 4, p. 041901, 2011. 58

[147] A. A. Balandin, S. Ghosh, W. Bao, I. Calizo, D. Teweldebrhan, F. Miao, and C. N. Lau, "Superior thermal conductivity of single-layer graphene.," *Nano letters*, vol. 8, pp. 902–7, Mar. 2008. 58

[148] Z. G. Fthenakis, Z. Zhu, and D. Tománek, "Effect of structural defects on the thermal conductivity of graphene: From point to line defects to haeckelites," *Physical Review B*, vol. 89, p. 125421, Mar. 2014. 58

[149] Z. H. Ni, T. Yu, Y. H. Lu, Y. Y. Wang, Y. P. Feng, and Z. X. Shen, "Uniaxial Strain on Graphene: Raman Spectroscopy Study and Band-Gap Opening," *ACS nano*, vol. 2, no. 11, pp. 2301–2305, 2008. 66, 70

[150] M. Lazzeri and F. Mauri, "Nonadiabatic Kohn Anomaly in a Doped Graphene Monolayer," *Physical Review Letters*, vol. 97, p. 266407, Dec. 2006. 66

[151] L. Wang, Z. Chen, C. R. Dean, T. Taniguchi, K. Watanabe, L. E. Brus, and J. Hone, "Negligible environmental sensitivity of graphene in a hexagonal boron nitride/graphene/h-BN sandwich structure," *ACS Nano*, vol. 6, no. 10, pp. 9314–9319, 2012. 67

[152] C.-C. Chen, W. Bao, J. Theiss, C. Dames, C. N. Lau, and S. B. Cronin, "Raman spectroscopy of ripple formation in suspended graphene.," *Nano letters*, vol. 9, pp. 4172–6, Dec. 2009. 69

[153] D. Yoon, Y.-W. Son, and H. Cheong, "Negative thermal expansion coefficient of graphene measured by Raman spectroscopy.," *Nano letters*, vol. 11, pp. 3227–31, Aug. 2011. 69

[154] K. Jia, Y. Su, Y. Chen, J. Luo, J. Yang, P. Lv, and Z. Zhang, "Effects of defects and thermal treatment on the properties of graphene," *Vaccum*, vol. 116, pp. 90–95, 2015. 69

[155] M. Z. Hossain, J. E. Johns, K. H. Bevan, H. J. Karmel, Y. T. Liang, S. Yoshimoto, K. Mukai, T. Koitaya, J. Yoshinobu, M. Kawai, A. M. Lear, L. L. Kesmodel, S. L. Tait, and M. C. Hersam, "Chemically homogeneous and thermally reversible oxidation of epitaxial graphene," 2012. 72

[156] G. K. H. Pang, K. Z. Baba-Kishi, and a. Patel, "Topographic and phase-contrast imaging in atomic force microscopy," *Ultramicroscopy*, vol. 81, no. 2, pp. 35–40, 2000. 73

[157] I. Schmitz, M. Schreiner, G. Friedbacher, and M. Grasserbauer, "Phase imaging as an extension to tapping mode AFM for the identification of material properties on humidity-sensitive surfaces," *Applied surface science*, vol. 115, no. 2, pp. 190–198, 1997. 73

[158] E. Nagao and J. A. Dvorak, "Phase imaging by atomic force microscopy: analysis of living homoiothermic vertebrate cells.," *Biophysical journal*, vol. 76, no. 6, pp. 3289–3297, 1999. 73

[159] J. Tamayo and R. García, "Deformation, Contact Time, and Phase Contrast in Tapping Mode Scanning Force Microscopy," *Langmuir*, vol. 12, no. 18, pp. 4430–4435, 1996. 73

[160] R. Garcia, C. J. Gómez, N. F. Martinez, S. Patil, C. Dietz, and R. Magerle, "Identification of nanoscale dissipation processes by dynamic atomic force microscopy," *Physical Review Letters*, vol. 97, no. 1, 2006. 73

[161] Z. Liu, A. a. Bol, and W. Haensch, "Large-scale graphene transistors with enhanced performance and reliability based on interface engineering by phenylsilane self-assembled monolayers," *Nano Letters*, vol. 11, no. 2, pp. 523–528, 2011. 79, 81

[162] Y. Sato, K. Takai, and T. Enoki, "Electrically controlled adsorption of oxygen in bilayer graphene devices.," *Nano letters*, vol. 11, pp. 3468–75, Aug. 2011. 80

[163] R. M. Ahmed, "Optical study on poly(methyl methacrylate)/poly(vinyl acetate) blends," *International Journal of Photoenergy*, vol. 2009, 2009. 80

[164] Y. G. Lee, C. G. Kang, U. J. Jung, J. J. Kim, H. J. Hwang, H. J. Chung, S. Seo, R. Choi, and B. H. Lee, "Fast transient charging at the graphene/ SiO2 interface causing hysteretic device characteristics," *Applied Physics Letters*, vol. 98, no. 18, pp. 2011–2014, 2011. 81

[165] B.-H. Lee, Y.-G. Lee, U.-J. Jung, Y.-H. Kim, H.-J. Hwang, J.-J. Kim, and C.-G. Kang, "Issues with the electrical characterization of graphene devices," *Carbon letters*, vol. 13, no. 1, pp. 23–28, 2012. 81

[166] K. M. Burson, W. G. Cullen, S. Adam, C. R. Dean, K. Watanabe, T. Taniguchi, P. Kim, and M. S. Fuhrer, "Direct imaging of charged impurity density in common graphene substrates," *Nano Letters*, vol. 13, no. 8, pp. 3576–3580, 2013. 81

[167] Y. D. Kim, M.-H. Bae, J.-T. Seo, Y. S. Kim, H. Kim, J. H. Lee, J. R. Ahn, S. W. Lee, S.-H. Chun, and Y. D. Park, "Focused-laser-enabled p-n junctions in graphene field-effect transistors.," *ACS nano*, vol. 7, pp. 5850–7, July 2013. 81, 102

[168] G. T. Boyd, Z. H. Yu, and Y. R. Shen, "Photoinduced luminescence from the noble metals and its enhancement on roughened surfaces," *Physical Review B*, vol. 33, no. 12, pp. 7923–7936, 1986. 82

[169] H. Kim, D. K. Taggart, C. Xiang, R. M. Penner, and E. O. Potma, "Spatial control of coherent anti-stokes emission with height-modulated gold zig-zag nanowires," *Nano Letters*, vol. 8, no. 8, pp. 2373–2377, 2008. 82

[170] F. Rana, P. a. George, J. H. Strait, J. Dawlaty, S. Shivaraman, M. Chandrashekhar, and M. G. Spencer, "Carrier recombination and generation rates for intravalley and intervalley phonon scattering in graphene," *Physical Review B - Condensed Matter and Materials Physics*, vol. 79, pp. 1–5, Mar. 2009. 87

[171] J. K. Viljas and T. T. Heikkilä, "Electron-phonon heat transfer in monolayer and bilayer graphene," *Physical Review B - Condensed Matter and Materials Physics*, vol. 81, no. 24, pp. 1–9, 2010. 87

[172] T. Ando, "Screening effect and impurity scattering in monolayer graphene," *Journal of the Physical Society of Japan*, vol. 75, no. 7, pp. 1–7, 2006. 89

[173] A. J. Frenzel, C. H. Lui, Y. C. Shin, J. Kong, and N. Gedik, "Semiconducting-to-metallic photoconductivity crossover and temperature-dependent drude weight in graphene," *Physical Review Letters*, vol. 113, no. 5, pp. 1–6, 2014. 89

[174] C. Kittel, *Introduction to solid state physics*. John Wiley & Sons, 2004. 91

[175] S. F. Shi, T. T. Tang, B. Zeng, L. Ju, Q. Zhou, A. Zettl, and F. Wang, "Controlling graphene ultrafast hot carrier response from metal-like to semiconductor-like by electrostatic gating," *Nano Letters*, 2014. 91, 104

[176] J. C. W. Song, M. Y. Reizer, and L. S. Levitov, "Disorder-Assisted Electron-Phonon Scattering and Cooling Pathways in Graphene," *Physical Review Letters*, vol. 109, p. 106602, Sept. 2012. 91

[177] E. C. Peters, E. J. H. Lee, M. Burghard, and K. Kern, "Gate dependent photocurrents at a graphene p-n junction," *Applied Physics Letters*, vol. 97, p. 193102, Nov. 2010. 102

[178] M. Inagaki and F. Kang, "Graphene derivatives: graphane, fluorographene, graphene oxide, graphyne and graphdiyne," *Journal of Materials Chemistry A*, vol. 2, p. 13193, June 2014. 102

[179] K. Andre Mkhoyan, A. W. Contryman, J. Silcox, D. A. Stewart, G. Eda, C. Mattevi, S. Miller, and M. Chhowalla, "Atomic and electronic structure of graphene-oxide.," *Nano letters*, vol. 9, pp. 1058–63, Mar. 2009. 102

[180] S. Stankovich, D. A. Dikin, G. H. B. Dommett, K. M. Kohlhaas, E. J. Zimney, E. A. Stach, R. D. Piner, S. T. Nguyen, and R. S. Ruoff, "Graphene-based composite materials.," *Nature*, vol. 442, pp. 282–6, July 2006. 102

[181] X. Huang, X. Qi, F. Boey, and H. Zhang, "Graphene-based composites.," *Chemical Society reviews*, vol. 41, pp. 666–86, Jan. 2012. 102

[182] J. Xu, K. Wang, S.-Z. Zu, B.-H. Han, and Z. Wei, "Hierarchical nanocomposites of polyaniline nanowire arrays on graphene oxide sheets with synergistic effect for energy storage.," *ACS nano*, vol. 4, pp. 5019–26, Sept. 2010. 102

[183] D. Wang, R. Kou, D. Choi, Z. Yang, Z. Nie, J. Li, L. V. Saraf, D. Hu, J. Zhang, G. L. Graff, J. Liu, M. A. Pope, and I. A. Aksay, "Ternary self-assembly of ordered metal oxide-graphene nanocomposites for electrochemical energy storage.," *ACS nano*, vol. 4, pp. 1587–95, Mar. 2010. 102

[184] L. Sun, L. Wang, C. Tian, T. Tan, Y. Xie, K. Shi, M. Li, and H. Fu, "Nitrogen-doped graphene with high nitrogen level via a one-step hydrothermal reaction of graphene oxide with urea for superior capacitive energy storage," *RSC Advances*, vol. 2, p. 4498, May 2012. 102

[185] M. Pumera, "Graphene-based nanomaterials for energy storage," *Energy Environ. Sci.*, vol. 4, pp. 668–674, Mar. 2011. 102

[186] H.-W. Wang, Z.-A. Hu, Y.-Q. Chang, Y.-L. Chen, H.-Y. Wu, Z.-Y. Zhang, and Y.-Y. Yang, "Design and synthesis of NiCo2O4reduced graphene oxide composites for high performance supercapacitors," *Journal of Materials Chemistry*, vol. 21, p. 10504, July 2011. 102

[187] M. Vila, M. C. Matesanz, G. Gonçalves, M. J. Feito, J. Linares, P. a. a. P. Marques, M. T. Portolés, and M. Vallet-Regi, "Triggering cell death by nanographene oxide mediated hyperthermia.," *Nanotechnology*, vol. 25, p. 035101, 2014. 102

[188] J. T. Robinson, S. M. Tabakman, Y. Liang, H. Wang, H. Sanchez Casalongue, D. Vinh, and H. Dai, "Ultrasmall reduced graphene oxide with high near-infrared absorbance for photothermal therapy," *Journal of the American Chemical Society*, vol. 133, pp. 6825–6831, 2011. 102

[189] K. Yang, S. Zhang, G. Zhang, X. Sun, S. T. Lee, and Z. Liu, "Graphene in mice: Ultrahigh in vivo tumor uptake and efficient photothermal therapy," *Nano Letters*, vol. 10, pp. 3318–3323, 2010. 102

[190] K. Yang, J. Wan, S. Zhang, B. Tian, Y. Zhang, and Z. Liu, "The influence of surface chemistry and size of nanoscale graphene oxide on photothermal therapy of cancer using ultra-low laser power," *Biomaterials*, vol. 33, no. 7, pp. 2206–2214, 2012. 102

[191] Y. Shen, S. Yang, P. Zhou, Q. Sun, P. Wang, L. Wan, J. Li, L. Chen, X. Wang, S. Ding, and D. W. Zhang, "Evolution of the band-gap and optical properties of graphene oxide with controllable reduction level," *Carbon*, vol. 62, pp. 157–164, Oct. 2013. 102

[192] A. Hunt, E. Kurmaev, and A. Moewes, "Band gap engineering of graphene oxide by chemical modification," *Carbon*, vol. 75, pp. 366–371, Aug. 2014. 102

[193] A. Nourbakhsh, M. Cantoro, T. Vosch, G. Pourtois, F. Clemente, M. H. van der Veen, J. Hofkens, M. M. Heyns, S. De Gendt, and B. F. Sels, "Bandgap opening in oxygen plasma-treated graphene.," *Nanotechnology*, vol. 21, p. 435203, Oct. 2010. 102, 103

[194] N. McEvoy, H. Nolan, N. Ashok Kumar, T. Hallam, and G. S. Duesberg, "Functionalisation of graphene surfaces with downstream plasma treatments," *Carbon*, vol. 54, pp. 283–290, Apr. 2013. 102, 103

[195] C.-H. Huang, C.-Y. Su, C.-S. Lai, Y.-C. Li, and S. Samukawa, "Ultra-low-damage radical treatment for the highly controllable oxidation of large-scale graphene sheets," *Carbon*, vol. 73, pp. 244–251, July 2014. 102

[196] Y. Shao, J. Wang, H. Wu, J. Liu, I. a. Aksay, and Y. Lin, "Graphene based electrochemical sensors and biosensors: A review," *Electroanalysis*, vol. 22, no. 10, pp. 1027–1036, 2010. 106

[197] S. Basu and P. Bhattacharyya, "Recent developments on graphene and graphene oxide based solid state gas sensors," *Sensors and Actuators, B: Chemical*, vol. 173, pp. 1–21, 2012. 106